Automatic Mesh Adaptivity for Hybrid Monte Carlo/Deterministic Neutronics Modeling of Difficult Shielding Problems

by

Ahmad Ibrahim

A dissertation submitted in partial fulfillment of

the requirement for the degree of

Doctor of Philosophy

(Nuclear Engineering and Engineering Physics)

at the

University of Wisconsin-Madison

2012

Date of final oral examination: 06/15/2012

The dissertation is approved by the following members of the Final Oral Committee:

Paul P.H. Wilson, Professor, Nuclear Engineering and Engineering Physics

Douglass L. Henderson, Professor, Nuclear Engineering and Engineering Physics

Gregory A. Moses, Professor, Nuclear Engineering and Engineering Physics

Thomas R. Mackie, Professor, Medical Physics

Mohamed E. Sawan, Distinguished Research Professor, Nuclear Engineering and Engineering Physics

Scott W. Mosher, R&D Staff Member, Oak Ridge National Laboratory

Abstract

Over the last decade, the role of neutronics modeling has been shifting from analysis of each component separately to high fidelity, full-scale analysis of the nuclear systems entire domains. The high accuracy, associated with minimizing modeling approximations and including more physical and geometric details, is now feasible because of advancements in computing hardware and development of efficient modeling methods. The hybrid Monte Carlo/deterministic techniques, CADIS and FW-CADIS dramatically increase the efficiency of neutronics modeling, but their use in the design of large and geometrically complex nuclear systems is restricted by the availability of computing resources for their preliminarily deterministic calculations and the large computer memory requirements of their final Monte Carlo calculations.

To reduce the computational time and memory requirements of the hybrid Monte Carlo/deterministic techniques while maintaining their efficiency improvements, three automatic mesh adaptivity algorithms were developed and added to the Oak Ridge National Laboratory AutomateD VAriaNce reducTion Generator (ADVANTG) code. First, a mixed-material approach, which we refer to as the macromaterial approach, enhances the fidelity of the deterministic models without having to refine the mesh of the deterministic calculations. Second, a deterministic mesh refinement algorithm improves the accuracy of structured mesh deterministic calculations by capturing as much geometric detail as possible without exceeding the total number of mesh elements that is usually determined by the availability of computing resources. Finally, a weight window coarsening algorithm decouples the weight window mesh from the mesh of the deterministic calculations to remove the memory constraint of the weight window map from the deterministic mesh resolution.

To analyze the combined effect of the three algorithms developed in this thesis, they were used to calculate the prompt dose rate throughout the entire ITER experimental facility. This calculation represents a very challenging shielding problem because of the immense size and complexity of the ITER structure and the presence of a two meter thick biological shield. Compared to a FW-CADIS calculation with the same storage size of the variance reduction parameters, the use of the three algorithms resulted in a 23.3% increase in the regions where the dose rate results are achieved in a 10 day Monte Carlo calculation and increased the efficiency of the Monte Carlo simulation by a factor of 3.4. Because of this significant increase in the Monte Carlo efficiency which was not accompanied by an increase in the memory requirements, the use of the three algorithms in FW-CADIS simulations enabled the simulation of this difficult shielding problem on a regular computer cluster using parallel processing of Monte Carlo calculations. The results of the parallel Monte Carlo calculation agreed at four points with a very fine mesh deterministic calculation that was performed on the super-computer, Jaguar.

Acknowledgments

Completing a PhD has always been my most incredible dream. Now that I feel I am getting very close, it is necessary to mention the people who made this possible. It is with immense gratitude that I acknowledge my Professor Paul Wilson, whose encouragement, guidance, and support have had the foremost influence on my career. I also need to thank him for his humility, calmness, and patience with me over the last six years. Other than being my teacher and role model, I am also very proud to consider him my friend. I cannot find the words to express my gratitude to Professor Mohamed Sawan for his invaluable advice and guidance on this work. I will always be indebted to Professor Sawan for his care and support that started before my admission to the University of Wisconsin-Madison. I share the credit for my work with many scientists in the Reactor and Nuclear Systems Division at Oak Ridge National Laboratory, particularly Dr. Douglas Peplow, Dr. Scott Mosher, Dr. John Wagner, and Dr. Thomas Evans. I owe my deepest gratitude to Dr. Peplow, not only for his extremely valuable technical help, but also for teaching me his exceptional work ethic, which I will always try to imitate. I want to extend my gratitude to many faculty members, research scientists, and current and former students in the Engineering Physics Department and the Fusion Technology Institute of the University of Wisconsin-Madison, in particular, Professor Laila El-Guebally, Professor Douglass Henderson, Dr. Ross Radel, and Dr. Brian Kiedrowski. Finally, I would like to express my deepest thanks to my family, especially my mother, Nadia, my father, Kamal, and my sisters, Nevin and Riham for their encouragement and support throughout my career. Without Nadia's endless love, I would have never reached my goal.

Contents

List of figures

List of tables

Nomenclature

3-D	Three dimensional
A^3MCNP	Automated Adjoint Accelerated MCNP
ADVANTG	AutomateD VAriaNce reducTion Generator
Bioshield	Biological shield
CAD	Computer aided design
CADIS	Consistent Adjoint Driven Importance Sampling
CC	Cell center
CDF	Cumulative distribution function
CLT	Central limit theorem
DAGMCNP	Direct Accelerated Geometry MCNP
DAWWG	Deterministic Adjoint Weight Window Generator
D-T	Deuterium-tritium
FENDL	Fusion evaluated nuclear data library
FOM	Figure of merit
FOR	Figure of reliability
FW-CADIS	Forward Weighted CADIS
HEU	High enriched uranium
HPC	High performance computing
IB	Inboard
KIT	Karlsruhe Institute of Technology
LANL	Los Alamos National Laboratory
LIFT	Local Importance Function Transform
M&S	Modeling and Simulation
MAVRIC	Monaco with Automated Variance Reduction using Importance Calculations
MC	Monte Carlo
MM	Macromaterials
ORNL	Oak Ridge National Laboratory
PDF	Probability density function
R	Relative uncertainties
RSICC	Radiation Safety Information Computational Center
SCALE	Standard Computer Analysis for Licensing Evaluation
S_N	Discrete ordinates
TFC	Toroidal field coil
UW	University of Wisconsin-Madison
VOV	Variance of the variance
VR	Variance reduction
VV	Vacuum vessel
WW	Weight-window
WWG	Weight-window generator

Chapter 1: Introduction

The term neutronics is used to describe the mathematical treatment of neutral particles (neutrons and photons) transport through materials. When neutronics calculations are used to determine the adequate amounts of shielding materials required to meet the radiation limits with minimal costs, they are called neutronics shielding calculations. The term shielding is often used to distinguish this type of neutronics calculations from criticality calculations which deal with calculating the multiplication factor in nuclear reactors.

Accurate, predictive neutronics modeling and simulation (M&S) is a critical, cross-cutting capability necessary for safe, reliable and cost-effective design analysis of nuclear facilities such as fission and fusion reactors. A current focus of the neutronics M&S research is to enable high-fidelity, full-scale reactor analyses for more accurate prediction capabilities. The high accuracy is associated with minimizing the modeling approximations, traditionally necessary for neutronics M&S, and allowing the addition of more physical and geometric detail to the neutronics models. The immense sizes and complicated structures of fusion energy systems strain the predictive capabilities of the current neutronics M&S techniques and limit their use in the design process of fusion reactors. In this thesis several algorithms are developed to increase the reliability and enhance the performance of the existing cutting-edge M&S methods to allow the accurate modeling of very challenging shielding problems.

Traditionally, two distinctive approaches have been developed and used for neutronics M&S: stochastic Monte Carlo (MC) and deterministic methods. Since the MC methods are generally considered more accurate, they have been more widely used in many applications. The

better accuracy of the MC methods is attributed to their ability to model the exact geometrical and physical details of real-life systems without the need for discretization approximations. The drawback of the MC methods is the prohibitive computational time requirements of some problems such as deep-penetration shielding problems. For example in a source-detector penetration problem with 10 orders of magnitude attenuation between the source and the detector, if each history requires one milli-second to simulate, it will require more than 1000 days for 10 particles reach the detector. The accuracy of the deterministic calculations depends on the resolution of the phase-space discretization but enhancing the resolution increases the number of unknowns and consequently increases the computational requirements. Accurate full-scale deterministic modeling of nuclear reactors requires huge amount of computational resources since the number of unknowns required to resolve the geometrical and physical domain of these systems is in the order of 10^{15} [1].

Due to the complementarity of both the deterministic and the MC approaches, each is advantageous to certain types of problems. The coupling between both the deterministic and MC methods has been known as the hybrid MC/deterministic methods. These hybrid techniques increase the overall efficiency of the neutronics M&S and enable the modeling of problems that are too difficult to be handled with either of the two approaches individually. This thesis is concerned with the two hybrid methods: Consistent Adjoint Driven Importance Sampling (CADIS) [2] and Forward Weighted CADIS (FW-CADIS) [3]. Both of these methods calculate the MC variance reduction (VR) parameters, used to accelerate the MC calculations, based on deterministically calculated fluxes. One or two relatively fast (low resolution) deterministic calculations are performed to accelerate the final MC simulation. The CADIS method is used to

increase the efficiency of the MC calculations of localized quantities while the FW-CADIS method is used for optimizing multiple tallies or tallies distributions.

Two issues related to obtaining the deterministic solutions, which are used to accelerate the MC calculations, need to be emphasized for CADIS and FW-CADIS. First, the total number of mesh cells used in the deterministic calculations of CADIS and FW-CADIS simulations of large and complicated problems can be $O(10^{2-3})$ less than the total number of mesh cells required to model the problem deterministically because the only goal of the deterministic calculations is to improve the efficiency of the MC simulation [4]. In addition to slowing down the deterministic calculations and increasing their memory requirement, fine meshes also increase the memory requirements of MC calculation by increasing the storage space of the VR parameters. Second, the automation of the creation of the deterministic input file is necessary for any successful implementation of CADIS and FW-CADIS because the manual development of such input files is extremely difficult for large and complicated problems. Automatic algorithms that manage the materials definitions of the deterministic models are already implemented in several codes that apply the CADIS and FW-CADIS methods.

As for all non-analog MC simulations, the efficiency of the MC calculation depends on the accuracy of the VR parameters, which are deterministically calculated in CADIS and FW-CADIS. For large and complicated problems, capturing all the physical and geometrical details in the CADIS and FW-CADIS deterministic calculations is not certain because the automatically developed deterministic input files use coarse meshes. The conceivable inconsistencies between the deterministic and the MC models can decrease the efficiency and the reliability of the CADIS and FW-CADIS simulations. ***The goal of this thesis is to enhance the efficiency and reliability of CADIS and FW-CADIS simulations of difficult shielding problems***

by developing automatic mesh adaptivity algorithms to improve the accuracy of the deterministic calculations without a large impact on the overall modeling efficiency. It is necessary to mention that the reliability of the CADIS and FW-CADIS simulations will not be directly measured to demonstrate the improvements of the algorithms developed in this thesis because of the difficulty of assessing the reliability of the MC simulations of large and complicated shielding problems. Instead, some causes of MC unreliability will be identified. By reducing the likelihood of these causes in CADIS and FW-CADIS simulations, the algorithms provided in this thesis are expected to enhance the simulations reliability. The three algorithms developed in this thesis are:

1. A mixed-material approach, which we refer to as the macromaterial (MM) approach, enhances the fidelity of the deterministic models without having to refine the mesh of the deterministic calculations.
2. A deterministic mesh refinement algorithm improves the accuracy of structured mesh deterministic calculations by capturing as much geometric detail as possible without exceeding the total number of mesh elements that is usually determined by the availability of computing resources.
3. A weight-window (WW) coarsening algorithm reduces the size of the VR parameters set with minimal or no decrease in the efficiency of the MC simulations.

The global prompt dose rate calculation throughout the entire ITER experimental facility, which is described in Ref. [4], was used to analyze the combined effect of the three algorithms developed in this thesis. This calculation represents a very challenging shielding problem because of the immense size and complexity of the ITER structure and the presence of a 2 m thick biological shield.

The remainder of this thesis is structured as follows. Chapter 2 reviews the neutral particles transport equation, the adjoint transport theory, the physical interpretation of the adjoint flux, and the generalized contributon transport theory. Brief descriptions of both deterministic and MC radiation transport methods are also presented. The deterministic discussion focuses on the solution accuracy of the discrete ordinates (S_N) methods and the MC discussion concentrates on the different methods of VR, the accuracy and precision of MC calculations, the reliability indicators of MC simulations, and the MC calculation efficiency. Several efficiency metrics for global MC simulations are also discussed. Finally, Chapter 2 summarizes the history of the hybrid MC/deterministic neutronics shielding methods and the theoretical background of the importance sampling technique.

Chapter 3 explains the CADIS and FW-CADIS methods in terms of theory, implementations, and applications. A special section is dedicated to demonstrate the efficiency and reliability issues of CADIS and FW-CADIS simulations. This section introduces the needs for the three algorithms devised in this thesis.

Chapter 4 describes the implementation of the MM approach for both materials definition and adjoint source description in CADIS and FW-CADIS simulations. The advantages of using the MM approach on both the deterministic calculations and the CADIS and FW-CADIS MC simulations are illustrated by examples.

Chapter 5 illustrates the deterministic mesh refinement algorithm. The enhancement in the accuracy of the deterministic calculations and the efficiency of CADIS and FW-CADIS MC simulations are exemplified for the deterministic mesh refinement algorithm.

Chapter 6 explains the WW coarsening algorithm and the adjoint flux collapsing formula. The advantages of using the adjoint flux collapsing formula and the WW coarsening algorithm are illustrated by examples.

Chapter 7 discusses the use of the MM approach, the deterministic mesh refinement algorithm, and the WW coarsening algorithm in calculating the prompt dose rate throughout the entire ITER reactor. The advantages of using each of the three algorithms on the efficiency of this FW-CADIS simulation are demonstrated.

Chapter 8 summarizes the conclusions of this thesis and suggests some topics for future research.

Chapter 2: Background and theory

2.1 Radiation transport theory

The equation describing the steady state neutral particles transport through materials can be expressed in the integro-differential form,

$$\hat{\Omega} \cdot \nabla\psi(\bar{r}, \hat{\Omega}, E) + \sigma_t(\bar{r}, E)\psi(\bar{r}, \hat{\Omega}, E) = \int_{4\pi} d\hat{\Omega}' \int_0^\infty dE' \sigma_s(\bar{r}, \hat{\Omega}' \to \hat{\Omega}, E' \to E)\psi(\bar{r}, \hat{\Omega}', E') + q(\bar{r}, \hat{\Omega}, E). \quad (2.1)$$

Equation (2.1) is called the linear Boltzmann transport equation or simply the transport equation. The six independent variables, which will be denoted in the rest of this report as the phase-space variables, are divided into three for the position, $\bar{r}$, two for the direction, $\hat{\Omega}$, and one for the energy, E. The angular flux $\psi(\bar{r}, \hat{\Omega}, E)$ represents the neutral particles flux at phase-space $(\bar{r}, \hat{\Omega}, E)$ per unit solid angle per unit energy. The source term, $q(\bar{r}, \hat{\Omega}, E)$ represents the rate per unit volume at which particles are produced at phase-space $(\bar{r}, \hat{\Omega}, E)$ per unit solid angle per unit energy. In fixed source shielding problems $q(\bar{r}, \hat{\Omega}, E)$ is the external source term while for problems with multiplying media, $q(\bar{r}, \hat{\Omega}, E)$ can be divided to two terms including a fission term and an external source term. The first term of the left hand side of Eq. (2.1) represents the loss of particles from the phase-space increment $d\bar{r}d\hat{\Omega}dE$ by streaming. The second term represents the loss of particles from the same increment by collisions where $\sigma_t(\bar{r}, E)$ is the total macroscopic cross section. The differential scattering cross section $\sigma_s(\bar{r}, \hat{\Omega}' \to \hat{\Omega}, E' \to E)$ can be divided into two terms as shown in Eq. (2.2),

$$\sigma_s\left(\bar{r}, \widehat{\Omega'} \to \hat{\Omega}, E' \to E\right) = \sigma_s(\bar{r}, E') f\left(\widehat{\Omega'} \to \hat{\Omega}, E' \to E\right). \quad (2.2)$$

In Eq. (2.2), $\sigma_s(\bar{r}, E')$ is the macroscopic scattering cross section at the energy E' and $f\left(\widehat{\Omega'} \to \hat{\Omega}, E' \to E\right)$ is the probability per unit solid angle per unit energy that a particle which had a collision at energy E' while moving in the direction $\widehat{\Omega'}$ will emerge within energy dE around E and a direction $d\widehat{\Omega}$ around $\widehat{\Omega}$. The $\widehat{\Omega'} \to \hat{\Omega}$ notation is often substituted with $\widehat{\Omega'} \cdot \hat{\Omega}$ because the angular variation of the differential scattering cross section is only a function of $\widehat{\Omega'} \cdot \hat{\Omega}$ except for special cases, such as when the medium is moving or consists of a single crystal [5].

Equation (2.1) can be written in operator form,

$$H\psi = q, \quad (2.3)$$

where H is the linear integro-differential operator ,

$$H = \widehat{\Omega} \cdot \nabla + \sigma_t(\bar{r}, E) - \int_{4\pi} d\widehat{\Omega'} \int_0^\infty dE' \sigma_s\left(\bar{r}, \widehat{\Omega'} \to \widehat{\Omega}, E' \to E\right).$$

2.1.1 Adjoint transport theory

To be distinguished from the adjoint transport equation and the adjoint fluxes, Eqs. (2.1) and (2.3) are often called the “forward” transport equation and their fluxes are called forward fluxes.

Since the transport equation is a linear integro-differential equation, a related adjoint equation can be formulated using the identity,

$$\langle \psi^+, H\psi \rangle = \langle \psi, H^+\psi^+ \rangle, \tag{2.4}$$

where H^+ is the adjoint operator and ψ^+ is the phase-space dependent angular adjoint flux corresponding to the angular adjoint flux ψ. The angle brackets < > signifies integration over all phase-space independent variables. The spatial domain of the problem is bounded by a surface Γ across which we will assume that no particles enter (i.e, vacuum boundary conditions). Hence the function upon which H operates is constrained to satisfy,

$$\psi\left(\bar{r}, \hat{\Omega}, E\right) = 0, \qquad \bar{r} \in \Gamma, \hat{n} \cdot \hat{\Omega} < 0,$$

where $\hat{n}$ is the outward normal. Using the operator form, the adjoint transport equation can be expressed by,

$$H^+\psi^+ = q^+, \tag{2.5}$$

where q^+ is the adjoint source density function. The adjoint operator, defined as,

$$H^+ = -\hat{\Omega} \cdot \nabla + \sigma_t(\bar{r}, E) - \int_{4\pi} d\hat{\Omega}' \int_0^\infty dE' \sigma_s\left(\bar{r}, \hat{\Omega} \to \hat{\Omega}', E \to E'\right), \tag{2.6}$$

can be deduced if we require that

$$\psi^+\left(\bar{r}, \hat{\Omega}, E\right) = 0, \qquad \bar{r} \in \Gamma, \hat{n} \cdot \hat{\Omega} \geq 0.$$

Mathematically there are no restrictions on the choice of the adjoint source function; however, with a certain choice of the adjoint source function, the adjoint flux can have a very

interesting physical significance. To explain this physical significance, the response, which the transport equation is calculating, will be represented by,

$$TR = \langle \psi, \sigma_d \rangle, \tag{2.7}$$

where σ_d is the response function (e.g. a detector cross-section) and TR is the calculated response.

The adjoint identity (Eq. (2.4)) can be expressed as,

$$\langle \psi, q^+ \rangle = \langle \psi^+, q \rangle. \tag{2.8}$$

According to Eq. (2.7) and Eq. (2.8), if the adjoint source was chosen to represent the response function ($q^+ = \sigma_d$), the response can be expressed as the integral of the adjoint weighted source distribution,

$$TR = \langle \psi^+, q \rangle = \int \psi^+(p) q(p) dp. \tag{2.9}$$

In particular, if the particles are emitted at $\bar{r}_0$, in direction $\hat{\Omega}_0$, at energy E_0at a rate of one particle per second,

$$q = \delta(\bar{r} - \bar{r}_0)\delta\left(\hat{\Omega} - \hat{\Omega}_0\right)\delta(E - E_0),$$

the response will be the adjoint flux at the same phase-space position.

$$TR = \psi^+\left(\bar{r}_0, \hat{\Omega}_0, E_0\right) \tag{2.10}$$

It is this fact that provides the physical significance of the adjoint flux as the importance of particles produced at $\bar{r}_0$, $\hat{\Omega}_0$, and E_0 to the objective response [5]. This will be discussed later in relation to the hybrid MC/deterministic techniques.

2.1.2 Contributon response theory

The generalized contributon transport equation can be obtained by multiplying Eq. (2.1) by ψ^+ and Eq. (2.5) by ψ and subtracting,

$$\hat{\Omega}\cdot\nabla c(\bar{r},E,\hat{\Omega})+\theta_s(\bar{r},E,\hat{\Omega})c(\bar{r},E,\hat{\Omega})= \int_{E'}\int_{\widehat{\Omega'}}\theta(\bar{r},E'\to E,\widehat{\Omega'}\cdot\hat{\Omega})c(\bar{r},E',\widehat{\Omega'})d\widehat{\Omega'}dE'+ q(\bar{r},E,\hat{\Omega})\psi^+(\bar{r},E,\hat{\Omega})-q^+(\bar{r},E,\hat{\Omega})\psi(\bar{r},E,\hat{\Omega}), \tag{2.11}$$

where,

$$c(\bar{r},E,\hat{\Omega})=\psi(\bar{r}_0,\hat{\Omega}_0,E_0)\psi^+(\bar{r}_0,\hat{\Omega}_0,E_0)$$

is a new variable that is denoted in the literature as the contributon flux [6],

$$\theta(\bar{r},E\to E',\widehat{\Omega'}\cdot\hat{\Omega})=\sigma_s(E\to E',\widehat{\Omega'}\cdot\hat{\Omega})\frac{\psi^+(\bar{r},E',\widehat{\Omega'})}{\psi^+(\bar{r},E,\hat{\Omega})}$$

is the double-differential scatter cross section for contributons, and

$$\theta_s(\bar{r},E,\hat{\Omega})=\int_{E'}\int_{\widehat{\Omega'}}\theta(\bar{r},E\to E',\widehat{\Omega'}\cdot\hat{\Omega})C(\bar{r},E',\widehat{\Omega'})d\widehat{\Omega'}dE'$$

is the total scatter cross section for contributons. Equation (2.11) is similar to the transport equation (Eq. (2.1)) but with some distinguishing features. First, only scattering reactions appear in the equation. This shows that contributons cannot get absorbed. Second, $c(\bar{r},E,\hat{\Omega})$ must vanish at vacuum boundaries because if the boundary conditions of both the

forward and the adjoint fluxes are combined, the boundary conditions for the contributons will be

$$c(\bar{r}, \hat{\Omega}, E) = 0, \qquad \bar{r} \in \Gamma.$$

Therefore contributons can never escape from the system by crossing an external boundary.

Since contributons are not absorbed and cannot leak out of the system, they must contribute to the detected response. The contributons are all introduced into the system by the source $q\psi^+$. They transport the response through the system until they flow out at the response sink $q^+\psi$. The rate the contributons drain from the system through the sink exactly equals the rate they flow into the system at the source.

The contributon concept is well-understood to convey theoretical information about the most likely paths that Monte Carlo particles travel from the source to contribute to a detector response. It should be noted that the contributon flux identifies regions in phase-space that are important to the solution of a source-response system while the adjoint flux identifies regions that are important only to the response.

2.2 Deterministic transport methods

Several mathematical methods have been used to solve the radiation transport equation deterministically. The two main categories of the deterministic methods are based on the integral and integro-differential forms of the transport equation [5]. The techniques based on the integral

form of the transport equation will not be discussed in this thesis. There are two widely used deterministic transport techniques based on solving the integro-differential methods: the S_N methods and the truncated spherical harmonics expansion method.

2.2.1 The truncated spherical harmonics expansion method

This class of methods is based on the expansion of the angular distribution of the particle flux in a complete set of orthogonal functions, namely the spherical harmonics. The expansions are truncated after some terms in order to develop practical methods for solving the resulting form of the transport equation. The spatial dependence of the angular flux is obtained by imposing a discrete mesh and evaluating the flux via the finite-difference or the finite-element methods. The energy variable is divided into a finite number of discrete energy groups.

A reasonably accurate solution might be obtained with only a few equations if the systems under consideration were large and the particles absorption is small. A truncated form (P_1) that assumes isotropic fluxes and isotropic scattering yields the diffusion approximation which played a crucial role in the history of neutron transport even though it is only valid under a number of unrealistic assumptions [7]. This class of methods will not be considered in this thesis.

2.2.2 The discrete ordinates (S_N) method

The S_N method has increasingly become the dominant technique for obtaining numerical solutions to the integro-differential form of the transport equation. It consists simply of evaluating the transport equation in discrete angular directions and is characterized by the simplicity of derivation. The algorithms used with S_N methods are marked by their notable computational efficiency compared to other deterministic methods. The S_N method will be the only deterministic methods considered in this thesis.

This class of solution methodologies is denoted as the S_N methods because the angular domain is discretized into a set of discrete directions known as S_N [5]. The spatial domain is discretized into a spatial mesh. Structured and unstructured mesh grids are used by the production-level codes for solving the transport equation. The energies are discretized into multiple groups with specific boundaries. The resulting linear system can then be solved using finite difference or finite elements method. Some of the popular S_N production-level codes are: PARTISN [8], TORT [9], ATTILA [10], and Denovo [11].

2.2.2.1 Solution accuracy of the S_N method

Truncation errors

The S_N solutions suffer from discretization errors due to the approximate nature of the discretization procedure. The solution accuracy of an S_N calculation may be suspected if the phase-space domain is not properly resolved. Unfortunately, the number of unknowns in a

deterministic calculation increases with enhancement of the phase-space resolution. The total number of unknowns, N_t, in an S_N calculation can be determined from the formula,

$$N_t = N_g \times N_c \times N_u \times N_a \times N_m, \tag{2.12}$$

where N_g is the total number of energy groups, N_c is the number of elements in the spatial mesh, N_u is the number of unknowns per cell that depends on the differencing scheme, N_a is the total number of scattering moments[1], N_m is the number of angles of the S_N discretization [1].

Generally, the computer time and memory[2] required by the S_N calculation scale linearly with N_t [12; 11]. The number of energy groups determined by the multi-group library. The number of angles must be large enough to avoid some well-known nonphysical anomalies [13; 14] that are beyond the scope of this thesis. The number of elements in the spatial mesh, N_c, scales inversely with the size of the elements. For acceptable accuracy, the conventional S_N schemes require the spatial mesh elements to have dimensions in the order of one mean free path at the lowest energy except for materials with high scattering ratios [15]. Since the diffusion length represents the relaxation factor of the thermal neutron flux, it is typically used for determining the mesh dimensions in materials with high scattering ratios. With these mesh sizes, the total number of spatial mesh elements needed to fully resolve the space domain of large systems such as fusion reactors will be in the order of 10^9 and the total number of unknowns for resolving the entire phase-space domain will be in the order of 10^{15} [1]. Only very few research

[1] Standard S_N methods expand the differential scattering cross-section, defined in Eq. (2.2), in Legendre polynomials (P_N). The total number of scattering moments is $(N+1)^2$ where N is the P_N order.
[2] In production-level S_N codes, not all the angular fluxes get stored in the memory during the calculation. The angular fluxes have only to be stored on the 2-D plane of the current sweep and they get updated as the sweep progresses. The number of angles is generally neglected when estimating the memory requirements of S_N calculations.

institutions have access to the computing resources needed for performing accurate 3-D S_N analysis for these kinds of problems because it requires massive parallelization on tens of thousands of processors [4].

Geometry discretization errors of structured meshes

Since realistic geometries do not usually conform to curvilinear coordinates, structured meshes can be very inefficient for modeling complex 3-D geometries. Structured meshes cannot accurately represent realistic models because geometry discretization errors preclude the conservation of relevant physical quantities such as materials masses. Using fine mesh resolutions can reduce but not eliminate the geometry discretization errors of structured meshes. Additionally, the S_N mesh refinement is limited by the computational resources because the number of unkowns scales linearly the total number of mesh elements according to Eq. (2.12).

Unlike structured meshes, unstructured meshes can accurately describe complex geometries [16]. Algorithms for solving the transport equations on unstructured tetrahedral spatial meshes have been developed and implemented [17]. Unstructured meshes will not be discussed because they were not used in this thesis.

2.3 Monte Carlo transport methods

During the Manhattan project the term Monte Carlo (MC) was first used to express a statistical approach that was used for neutronics modeling. The MC methods do not solve the transport equation explicitly. Instead the answers are obtained by averaging the scores of numerous particles histories simulated by random sampling. The two main processes involved in

the MC methods are the sampling and the tallying. The MC methods duplicate the individual probabilistic events occurring throughout the particles histories from the moment of their birth at the source to their death by absorption or leakage from the system. The sampling process uses random numbers to duplicate the physical processes according to the distribution functions governing these processes. During the simulation of the particles histories, a history will "score" if it contributes to the response of interest. This response of interest can be the interaction rate or the particle flux at a certain phase-space region [18]. A tally accumulates a set of scores for the response of interest. According to the Strong Law of Large Numbers [19], if the number of samples is large, the expected mean value of the underlying probability density function (PDF) can represent the tally result. Estimates of the statistical precisions of the results are usually tallied alongside with the mean value.

Because the MC method does not involve phase-space discretization, it is well suited to solving complicated 3-D problems. The exact geometries are used during the MC simulations and particles trajectories can be sampled from continuous rather than discrete function. Interpolation of the available point-wise data as a function of energy is used for providing continuous data for some MC codes [20].

The main drawback of the MC methods is the time and computer resources requirement. To achieve results with acceptably low statistical uncertainty, it is often necessary to simulate billions of particles histories consuming many hours or days of computer time. The issue is more serious for problems at which only small fraction of particles contribute to the tally of interest. Deep penetration shielding problems are the most popular example of these kinds of problems. For example in a simple source-detector penetration problem with 10 orders of magnitude attenuation between the source and the detector, if one history requires one milli-second to

simulate, it will require more than 1000 days for 10 particles to score at the detector. Another drawback of the MC methods is their non-global nature. An extra tally is required for calculating every additional response.

Most of the MC simulations used in this thesis uses the general-purpose MC code MCNP5[3] developed in Los Alamos National Laboratory (LANL) and distributed through the Radiation Safety Information Computational Center (RSICC). MCNP is a direct descendent of the work of the Manhattan project scientists on the MC methods at LANL [21].

2.3.1 Non-analog Monte Carlo methods

The simplest form of MC calculations is analog MC. In analog MC, particles are followed from birth to death according to natural probabilities. It is called analog MC because it is analogous to the natural transport of particles through materials. As noted earlier, the natural simulation of particles require huge computing resources especially for deep penetration shielding problems. In non-analog MC the physical laws of radiation transport are modified to transport particles toward the region of interest as efficiently as possible. In other words there is a preferential following of interesting particles more than uninteresting ones. The techniques formulated for this non-analog simulation are known as variance reduction (VR) techniques.

There are four classes of VR techniques:

1. **Truncation Methods**

These are the simplest of VR methods. They speed up calculations by truncating parts of

[3] MCNP is a trademark of the Los Alamos National Laboratory operated by the Los Alamos National Security, LLC for the National Nuclear Security Administration of the U.S. Department of Energy.

phase space that do not contribute significantly to the solution. The simplest example is geometry truncation in which unimportant parts of the geometry are simply not modeled.

2. Modified Sampling Methods:

Modified sampling methods alter the statistical sampling of a problem to increase the number of tallies per particle. For any MC event it is possible to sample from any arbitrary distribution rather than the physical probability as long as the particle weights are then adjusted according to the equation,

$$w_{biased}(\bar{r},\hat{\Omega},E)p_{biased}(\bar{r},\hat{\Omega},E) = w_{unbiased}(\bar{r},\hat{\Omega},E)p_{unbiased}(\bar{r},\hat{\Omega},E). \quad (2.13)$$

$p_{unbiased}$ is the PDF of the physical process before the modified sampling and p_{biased} is the new PDF after the modified sampling. Similarly $w_{unbiased}$ and w_{biased} are the particles' weights before and after the modified sampling respectively. Both the particles' weights and the PDFs are functions of all phase-space variables for generality but similar equations can be developed if any of these variables is not considered. Thus, with modified sampling methods, sampling is done from distributions that send particles in desired directions or into other desired regions of phase-space such as time or energy, or change the location or type of collisions.

3. Population Control Methods

Population control methods use particle splitting and Russian roulette to control the number of samples taken in various regions of phase space. Particles transported to regions of lower importance play Russian roulette. In the Russian roulette game, the particles are killed with a given probability but with the complementary probability they survive. This way, unimportant particles are followed less often. On the other hand, if particles are transported to

regions of higher importance, they split. Each of the split particles are simulated independently. To ensure that the problem solution remains unbiased, Eq. (2.13) has to be used for adjusting the particles weights.

4. Partially-Deterministic Methods

Partially-Deterministic Methods circumvent the normal random walk process by using deterministic-like techniques, such as next event estimators, or by controlling the random number sequence.

The following summarizes some VR techniques that are relevant to this thesis. A more complete discussion can be found in Ref. [22; 23]

Geometry, time, and energy splitting/roulette

Splitting and Russian roulette can be implemented in space, time, and energy. To be distinguished from the WW technique, the geometry, time, and energy splitting/roulette will be denoted as the simple phase-space splitting/roulette in the rest of this report. In the simple phase-space splitting/roulette, the particles split and roulette upon entering various phase-space regions according to the importance ratio of the regions the particles entered and the regions from which they came.

Weight-window technique/weight-window Generator

Although simple phase-space splitting/Russian roulette is very effective at producing more statistical samples in regions of interest, it can also cause fluctuation in the scoring values leading to statistical instabilities which can delay the MC convergence. The WW method was developed, not only to increase the sampling in important phase-space regions, but also to control particles' weights. Upper and lower bounds are assigned to each region of phase-space. If

a particle's weight is below the lower weight bound, Russian roulette is performed, and the particle's weight is either increased to be within the WW or the particle is terminated. On the other hand, if the particle's weight is above the upper weight bound, the particle is split such that the split particles all have weights within the WW. If the particle's weight falls within the WW, no adjustment is performed. Contrary to the importances, weight bounds decrease in the direction of the important regions and increase away from them.

The WW is usually better than the simple splitting/rouletting technique because the WW controls the weight fluctuations by forcing the particles having the similar positions and energy to have the same weights.

Setting the WW bounds is difficult and non-intuitive. Booth and Hendricks developed a technique called the forward-adjoint generator, which has since become known as the WW generator (WWG) [24]. The WWG statistically estimates the importance of each phase-space region as the expected score generated by a unit weight particle after entering a certain phase-space region. The importance of the phase-space interval, p can be estimated as,

$$Importance(p) = \frac{total\ scores\ due\ to\ particles\ entering\ p}{total\ weight\ entering\ p}. \tag{2.14}$$

The WWG has been implemented in MCNP in two flavors. The original WWG is a cell based WWG which is restricted to the geometrical components (cells) of the MCNP geometry. The second flavor is a geometry independent mesh-based WWG for which weights can be generated on a mesh that is not a part of the physical geometry but rather is superimposed over it [25].

The WWG is a quite simple statistical estimation of the importance function of a given phase-space region. The main difficulty of the WWG arises from the poor estimates of the importance function caused by the statistical nature of the generator. If a phase-space region is not properly sampled during WW generation, either unreliable importance estimate or no importance estimate will result. The failure of the MCNP WWG to calculate an importance (or weight) for a certain phase-space region appears as "zero" in the WWG output. This occurs if none of the particles enter the region or if the particles entering the region do not score. The problem of having too many zeros in the MCNP WWG output is very well-known in deep penetration shielding problems. There are many ways to enhance the WWG performance; some of them are discussed in Ref. [26]. These ways have proved beneficial in many types of problems but if used like a black box they can delay the MC convergence and/or bias the answers. None of these ways is suitable for enhancing the performance of the WWG for global MC problems [26].

Source biasing

Source biasing allows the simulation of a larger number of source particles in the more important phase-space regions. This technique consists of sampling the source from a biased PDF. The weights of the source particles have to be adjusted according to Eq. (2.13) [23].

2.3.2 Accuracy and precision of Monte Carlo calculations

Distinguishing between the accuracy and the precision of the MC calculation is important to this thesis. The MC uncertainty estimates refer only to the precision of the results and not to the accuracy. The latter is related to systematic errors resulting from multiple factors such as:

nuclear data uncertainties, coding errors, and inappropriate modeling. Figure 2.1 shows the difference between the statistical uncertainties determining the precision of the MC calculation and the systematic error determining its accuracy. The uncertainties in the expected values ($E(x)$) results from the fluctuations of the scoring values of each of the sampled histories while the systematic errors determine how far this expected value from the true value [27].

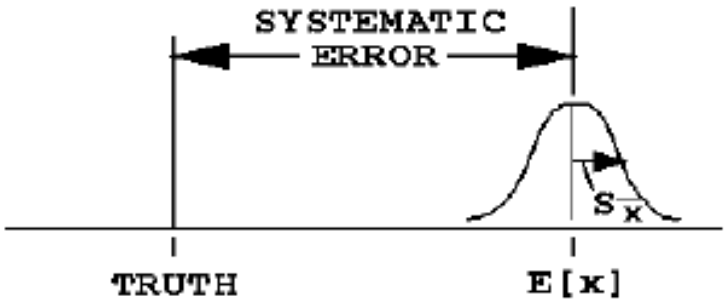

Figure 2.1: Systematic (accuracy) versus uncertainty (precision) errors [27]

It is quite possible to calculate a highly precise result that is far from the physical truth (not accurate) because nature has not been modeled faithfully [27].

Monte Carlo accuracy

The accuracy of the MC results is affected by many factors that can be grouped into three main categories: the code, the problem-modeling, and the user. The code factors encompass: the physical and mathematical models used, uncertainties in the data, and coding errors (bugs). The problem-modeling factors include the geometrical approximations and the energy and angular representation. The user's input errors can affect the problem accuracy. The user can also abuse the VR techniques that some portions of phase-space are not allowed to contribute to the result. This last factor is the primary research focus in this thesis [27].

Monte Carlo precision

1. **Monte Carlo mean, variance, and standard deviation**

MC results (tallies) are obtained by simulating particle histories and assigning a score x_i for each history. The particles histories produce a range of scores depending on the selected tally and VR. If $f(x)$ is the history score probability density function for selecting a particle history that scores x to the tally being estimated, the true mean will be the expected value $E(x)$,

$$E(x) = \int x f(x) dx. \tag{2.15}$$

In MC simulations, the function $f(x)$ is never known explicitly. Instead $f(x)$ is implicitly sampled by the MC sampling process. The true mean is approximated with the sample mean $\bar{x}$,

$$\bar{x} = \frac{1}{N}\sum_{i=1}^{N} x_i. \tag{2.16}$$

According to the Strong Law of Large Numbers [19], $\bar{x}$ tends to the limit $E(x)$ as N approaches infinity. The variance of x is a measure of the spread of x_i,

$$\sigma^2 = \int \big(x - E(x)\big)^2 f(x) dx = E(x^2) - \big(E(x)\big)^2. \tag{2.17}$$

Estimate of the variance associated with the spread of the distribution of x_i can be approximated from the sampling process,

$$S^2 = \frac{1}{N-1}\sum_{i=1}^{N}(x_i - \bar{x})^2 \approx \overline{x^2} - \bar{x}^2. \tag{2.18}$$

The estimated variance in the mean $\bar{x}$ can be calculated as,

$$S_{\bar{x}}{}^2 = \frac{S^2}{N}, \tag{2.19}$$

and hence the standard deviation in $\bar{x}$ is the square root of this variance. The standard deviation in $\bar{x}$ is what is usually denoted as the MC tally uncertainty not the spread of the scoring distribution. It is instructive to note that standard deviation in $\bar{x}$ is proportional to $1/\sqrt{N}$.

To define confidence intervals for the precision of a MC result, the Central Limit Theorem (CLT) [28] is used,

$$\lim_{N\to\infty} Pr\left(E(x) + \alpha\frac{\sigma}{\sqrt{N}} < \bar{x} < E(x) + \beta\frac{\sigma}{\sqrt{N}}\right) = \frac{1}{\sqrt{2\pi}}\int_{\alpha}^{\beta} e^{-t^2/2}dt, \tag{2.20}$$

where α and β can be any arbitrary values that can be positive or negative. $Pr(z)$ means probability of z.

For large number of samples ($N \to \infty$), $S_{\bar{x}}$ is approximately equal to σ. After replacing the true variance with the sample variance and plugging numbers for α and β.

$$\bar{x} - S_{\bar{x}} < E(x) < \bar{x} + S_{\bar{x}} \quad \sim 68\%\ of\ the\ time$$

$$\bar{x} - 2S_{\bar{x}} < E(x) < \bar{x} + 2S_{\bar{x}} \quad \sim 95\%\ of\ the\ time$$

The CLT states that the estimated mean will appear to be sampled from a normal distribution with a known standard deviation (σ) when N approaches infinity. In practice, σ is not known and must be approximated by the estimated standard deviation $S_{\bar{x}}$. The major difficulty in applying the CLT correctly to a MC result to form a confidence interval is knowing when N has approached infinity. Another key point about the validity of the confidence intervals

is that the physical phase-space must be adequately sampled by the MC process. For example, if an important path in the geometry is not well sampled both $\bar{x}$ and $S_{\bar{x}}$ will be unknowingly incorrect and the results will be wrong, usually tending to be too small [27]. The reliability of the MC results and the validity of the confidence intervals created by the calculated MC uncertainties will be discussed in details in Sec. 2.4.

2. Factors affecting Monte Carlo precision

There are multiple factors that affect the MC precision such as: the tally type, VR techniques, and numbers of histories. In this thesis, we will only concentrate on the number of histories and the VR techniques.

The MC precision is proportional to $1/\sqrt{N}$. Running more histories should increase the MC precision but running more histories increases the computer time and therefore should be viewed as the last resort for difficult shielding problems.

Not all the histories score in the tally. For difficult shielding problems the fraction of histories with nonzero scores (scoring efficiency) is always very small. The MC precision is affected by the scoring efficiency and by the distribution of the scoring values of the histories. These scoring values (scores) are affected by the use of VR techniques due to the weights adjustments according to the conservation relation (Eq. (2.13)). The hypothetical scoring distribution function $f(x)$ shown in Fig. 2.2 illustrates how the distribution of the scores around the mean $E(x)$ can be affected by both the scoring efficiency of the histories and the fluctuations of the scoring values around the mean.

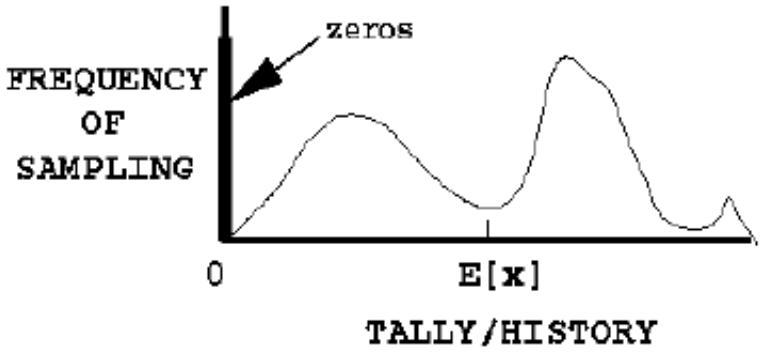

Figure 2.2: Hypothetical scoring distribution function [27]

A calculation is more precise when the scoring efficiency is high and the fluctuations of the nonzero scores are low. Most of the VR techniques tend to increase the MC precision by increasing the number of nonzero scoring histories. Although the use of VR techniques can causes scores fluctuations, some VR techniques such as the WW can also increase the MC efficiency by decreasing the scores fluctuations [27].

2.3.3 Efficiency and reliability of Monte Carlo calculations

As noted earlier, multiple factors can cause the MC results to be incorrect or imprecise. In this thesis, we will only concentrate on the inappropriate use of VR techniques. If the VR parameters are a good match to the sources of variance, the MC calculation usually produces no surprises [29]. On the other hand VR techniques can be abused so that some portions of phase-space are so heavily sampled in excess to their importance to the tally and other portions are not well sampled. In these cases, VR can have undesirable effects on both the accuracy and the precision of the MC calculation. While oversampling unimportant phase-space regions

decreases the MC efficiency, insufficient sampling of important phase-space regions can prevent the MC convergence and/or lead to wrong answers.

In the next subsection, some indicators for the reliability of the MC calculations are explained as used in MCNP and other popular MC codes. Indicators of the unreliability of MC calculations are explained in the following subsection. Finally, the factors affecting the efficiency metric of a MC calculation of a single tally are explained in subsection 2.3.3.3.

2.3.3.1 Reliability indicators

Relative uncertainties

The estimated relative uncertainty (R) in MCNP and many other MC codes is defined as

$$R = \frac{S_{\bar{x}}}{\bar{x}}. \tag{2.21}$$

The relative error is a convenient number because it represents statistical precision as a fractional result with respect to the estimated mean. It also acts as a tally reliability indicator.

For large N, R can be written as

$$R = \left[\frac{1}{N}\left(\frac{\overline{x^2}}{\bar{x}^2} - 1\right)\right]^{1/2} = \left[\frac{\sum_{i=1}^{N} x_i^2}{\left(\sum_{i=1}^{N} x_i\right)^2} - \frac{1}{N}\right]^{1/2}. \tag{2.22}$$

This form shows that, if all the scores are nonzero and equal, R is zero. Thus reducing the spread of the scores fluctuations decreases the variance. If all the scores are zeros, R is defined to be zeros. If only one nonzero score is made, R approaches unity as N becomes large.

Table 2.1 presents the recommended interpretation of the estimated 1σ confidence interval $\bar{x}(1 \pm R)$ for various values of R associated with an MCNP tally. These guidelines were determined empirically, based on years of experience using MCNP on a wide variety of problems [27].

Table 2.1: MCNP guidelines for interpreting R [27]

Range of R	Quality of tally
50% to 100%	Garbage
20% to 50%	Factor of few
10% to 20%	Questionable
<10%	Generally reliable except for point detector
<5%	Generally reliable for point detector

There is no guarantee that the estimated R will decrease inversely proportional to the $\sqrt{N}$ as required by the CLT because of the statistical nature of the tallies. Early in the problem, R will generally have large statistical fluctuations. Later, the inadequate sampling of important phase-space regions can produce large scores causing fluctuations in $S_{\bar{x}}$ and to a lesser extent in $\bar{x}$ and therefore in R [27].

Figure of merit

For a single tally, a well-defined figure of merit (FOM) for the MC calculations has been established as,

$$FOM = \frac{1}{R^2 T}. \tag{2.23}$$

R^2 should be proportional to $1/N$ and the computer time T should be directly proportional to N. The quantity R^2T should be approximately constant for a certain MC run with certain VR parameters [27].

The MC FOM has three uses [27]:

1. A tally reliability indicator
    - For well-behaved tallies, the FOM should be constant as a function of N.
2. Optimizing MC efficiency
    - Larger FOM indicates higher MC running efficiency. By several short runs, the user can compare between different VR parameters and choose the one with the highest FOM.
3. Estimate the computer time required for reaching certain R

Empirical score PDF and Pareto slope

A history score posted to a tally can be thought of as having been sampled from an underlying and generally unknown history score PDF, $f(x)$, where the random variable x is the score from one complete particle history [30]. The quantity, $f(x)dx$ is the probability of selecting a history score between x and $x + dx$ for the tally. As a PDF, $f(x)$ is normalized ($\int f(x)dx = 1$).

For valid confidence intervals, the CLT requires the first two moments of $f(x)$ to exist. To assess whether $f(x)$ appears to have been completely sampled, the behavior of $f(x)$ for large history scores can be examined. If complete sampling has occurred, the largest values of the sampled scores should have reached the upper bound (if such a bound exists) or should decrease faster than $1/x^3$ so that $E(x^2) = \int x^2 f(x)dx$ exists. This means that σ is finite and the confidence interval is valid according to the CLT.

During the MC simulation, the slope n of the logarithm of $f(x)$ at the largest score can be estimated to determine if and when the largest history scores decrease faster than $1/x^3$. It is postulated that if such decreasing behavior in the empirical $f(x)$ is not faster than $1/x^3$, then N is not large enough to satisfy the CLT because $f(x)$ has not been completely sampled [31]. Therefore, a larger N is required before a confidence interval can be formed.

Variance of the variance

Another quantity that can help the user establish more reliable confidence intervals is the variance of the variance (VOV). The quantity is analogous to the square of R, except it is the relative uncertainty in R, itself, not the mean. It is defined as,

$$VOV = \frac{S^2(S_{\bar{x}}^2)}{S_{\bar{x}}^4}, \tag{2.24}$$

where $S_{\bar{x}}^2$ is the estimated variance of $\bar{x}$ and $S^2(S_{\bar{x}}^2)$ is the estimated variance in $S_{\bar{x}}^2$.

The VOV is a measure of the relative statistical uncertainty in the estimated R and is important because $S_{\bar{x}}$ must be a good approximation of σ to use the CLT to form confidence intervals.

The estimated VOV can be defined as,

$$VOV = \frac{\sum(x_i - \bar{x})^4}{(\sum(x_i - \bar{x})^2)^2} - \frac{1}{N}. \tag{2.25}$$

With some mathematical manipulation, it can be proven that the desired VOV behavior is to decrease inversely with N [27]. This criterion is necessary but not sufficient condition for a statistically well-behave tally. Because the VOV involves the estimated third and fourth

moments of the empirical PDF $f(x)$, it is a much more sensitive indicator to large scores fluctuations than R and the mean [27]. Some cases of "unreliability" can be detected by estimating higher statistical moments which are more sensitive to statistical anomalies than the standard deviation [32].

MCNP statistical checks

To allow users to build confidence in the results and detect statistical anomalies, MCNP prints the results of ten statistical checks of one of the tally bins [27]. The quantities involved in these checks are the estimated mean, R, VOV, FOM, and the large score behavior of $f(x)$. The MCNP statistical checks [27] are:

1. A nonmonotonic behavior in the estimated mean as a function of the number of histories (N) in the last half of the problem.
2. Magnitude of R (< 0.05 for point detector tallies and < 0.1 for all other tallies).
3. A monotonically decreasing R as a function of N.
4. A $1/\sqrt{N}$ decrease in R in the last half of the problem.
5. Magnitude of VOV (< 0.1 for all types of tallies).
6. A monotonically decreasing VOV as a function of N in the last half of the problem.
7. A $1/N$ decrease in the VOV as a function of N in the last half of the problem.
8. A statistically constant FOM as a function of N in the last half of the problem.
9. A nonmonotonic behavior in the FOM as a function of N in the last half on the problem.
10. A Pareto slope of 3 or greater.

Passing all the checks should provide additional assurance that the confidence intervals will cover the expected result the correct fraction of time. Not passing several of the checks is an

indication that the confidence interval may not be correct. A nonmonotonic trend in the mean for the last half of the problem is a strong indicator that the confidence interval is likely to produce incorrect coverage rates. The magnitudes of R and the VOV should be less than the recommended values to increase the likelihood of a valid confidence interval. Small jumps in the R, VOV, and/or the FOM as a function of N are not threatening to the quality of the result. The slope of the empirical $f(x)$ is an especially strong indicator that N has not approached infinity in the sense of the CLT [27].

2.3.3.2 Unreliability and undersampling

When running MCNP, it is recommended to check all the MCNP statistical checks. Not passing some of the checks might be an indication of inappropriate sampling [27]. Excess splitting due to single event is another unreliability indicator. The MC code Monaco [33] prints a message with position and velocity information of the event at which more than 1000 particles are created by splitting.

One of the unreliability indicators of the MC calculations is the appearance of erratic uncertainties. Erratic uncertainties appear when scores from high-weight (low-importance) particles, coming from important phase-space regions that have not been well sampled, contribute to the tally. To avoid high-weight particles in important regions, the user should ensure all phase-space regions are well sampled by many particles as well as try to control the weights' fluctuations. If, despite the user's efforts, erratic uncertainties appeared, user should print the event logs for those particles causing the erratic uncertainties. The event logs should be studied to learn what is special about these particles. When the special nature of these particles is

understood, the user can adjust the VR parameters to sample these particles more often. This will cause their weight to be smaller so that they will be less likely to cause erratic uncertainties. Ignoring these particles will cause the MC results to be inaccurate [26]. For large and complicated problems, it might be very difficult to understand the reason for the appearance of these high-weight particles especially because the event logs of these particles are usually composed of millions of lines.

It is necessary to mention that even though the reliability indicators existing in many MC codes can be very useful in detecting the "unreliability" of the MC calculations, the reliability of the MC calculations cannot be guaranteed especially for large and complicated shielding problems. In some cases, the insufficient sampling of important phase-space regions can be so severe that the final MC results are unrealistically small while their uncertainties and the other reliability checks do not indicate the seemingly acceptable results. These cases, generally known as "undersampling", can lead to results that are so far from the physical truth (not accurate) with no clues that anything is missing [34; 32]. This will be demonstrated by a realistic example in Sect. 3.3.

2.3.3.3 Efficiency of Monte Carlo methods

For a single tally, the MC efficiency is measured by the FOM defined in Eq. (2.23). In this thesis, the single tally FOM will be used as the efficiency metric for each single response in an MC calculation. The VOV, which MCNP already estimates, will be used to express the

statistical uncertainty in the FOM because it determines the statistical uncertainty in R^2. The uncertainty in the single tally FOM will be computed using the relation,

$$\frac{\sigma_{FOM}}{FOM} = \sqrt{VOV}. \tag{2.26}$$

It is important to notice that the statistical uncertainties in the FOMs described in this thesis are biased but they provide a good first estimate. The reason for biasing is that the expectation value of the reciprocal of an integral is not equal to the reciprocal of the expectation values of the integral [35]. The uncertainty in the MC calculation time is also ignored in Eq. (2.26).

The FOM should be constant for well-behaved tallies. Higher FOM indicates smaller R for the given time, R can be expressed as,

$$R = \frac{S/\sqrt{N}}{\bar{x}}. \tag{2.27}$$

For a fixed time, either decreasing S or increasing N can lead to a smaller R and a higher FOM. Unfortunately, these two goals usually conflict. Decreasing S normally requires more time per history because better information is required. Therefore, for a fixed time, increasing N normally increases S because less time is spent per history. However, using VR techniques it is possible to substantially decrease S without too much decrease in N or to substantially increase N without too much increase in S. VR techniques attempt to decrease R by either producing particles in important phase-space regions or destroying particles in unimportant phase-space regions. In general, techniques that produce histories attempt to decrease S and techniques that destroy histories attempt to increase N [27].

2.3.4 Efficiency metrics of global Monte Carlo problems

For assessing some of the improvements of the algorithms developed in this thesis, the efficiency of global MC calculations needs to be quantified. Extending the concept of the FOM of a single tally to several tallies or mesh tallies is not straightforward since R is not well-defined for a tally distribution. There are many valid possibilities for global MC FOMs, but their practicality and usefulness as efficiency metrics depend on what the user desires from a global MC calculation.

Several efficiency metrics have been suggested in the literature for global MC problems but a unified global MC FOM has not been established. Some FOM metrics for tally distributions are described in this section.

Cumulative distribution function *R*

To compare the uncertainties of a mesh tally, a histogram of the cumulative distribution function (CDF) can be used. The CDF histogram shows the fractions of mesh tally elements that have R below a given value [36]. By comparing the CDF histograms of different MC cases with fixed runtime, one can deduce which case is more efficient at certain R because a higher fraction of mesh tally cells with low R is an indicator for a better MC calculation efficiency.

Care should be taken when assessing the efficiency of different MC cases at a fixed runtime if the CDFs of the mesh tally Rs cross each other. As the runtime continues, the R at which the different CDFs cross can change and different regions of the CDFs may become more important for the efficiency assessment.

FOM based on maximum R

An FOM for several tallies or mesh tallies can be defined as

$$FOM = \frac{1}{R_{max}^2 T}, \tag{2.28}$$

where R_{max} is the maximum R in all the tallies or the mesh tally elements and T is the computation time.

Since this FOM is based on the voxel with the slowest convergence rate, it can be used for characterizing the MC simulation efficiency if the user is interested in acquiring low Rs everywhere. This is usually the case for MC calculations of few tallies at specific locations. This FOM can also be suitable for assessing the MC calculation efficiency for multi-physics analysis because uniform low Rs are often required when the MC calculations are coupled with other types of calculations such as structural analysis, thermal-hydraulics, or neutron activation.

FOM based on average variance

An FOM based on the mean of the relative variances R^2 of the mesh tally elements was suggested in Ref. [37],

$$FOM = \frac{1}{\overline{R^2} T}. \tag{2.29}$$

In Eq. (2.29), $\overline{R^2}$ is the mean of the distribution function of the relative-variances (R^2) of the mesh tally elements and T is the MC computation time.

As a consequence of the CLT, $\overline{R^2}$ scales as $1/N$, where N is the number of histories. Since T scales with N, this FOM should be asymptotically constant with time. In Ref. [37], the basic assumption for this FOM was that the user desires as many elements having all R below a

specific value for the lowest time possible. This FOM was not recommended for problems with non-scoring tallies because R is undefined for the voxels without MC scoring.

Frequently in MC calculations of large and complicated problems, the calculations need to be stopped before MC scoring occurs in all the tallies. The uncertainties in the tallies without scoring are undefined. The scoring efficiency in some tallies can also be very small that the calculated uncertainties in these tallies are unreliable. Since tallies without MC scoring are expected to have the lowest scoring efficiency, this FOM has to be combined with the fraction of non-zero scoring tallies for difficult shielding problems. A typical procedure for calculating $\overline{R^2}$ is to assign $R = 100\%$ for all the tallies without MC scoring. Since the tallies without any MC scoring are expected to have a slower convergence rate than the tallies with $R = 100\%$, the FOM is expected to be overestimated with this assumption. The magnitude of the overestimation in the calculated FOM is expected to be lower for the cases with larger fractions the non-zero scoring tallies.

If the MC scoring did not occur in all the voxels, the computational time of the different MC cases has to be set constant for reliable comparisons of the MC efficiencies because this FOM is not expected to be constant with time until R^2 of all the tallies achieved the $1/N$ behavior. For constant time comparisons using this FOM, the time in the denominator of Eq. (2.29) does not need to be included.

FOM based on maximum *R* of tallies above certain threshold

In global MC calculations, the most difficult tallies are usually the tallies with smallest values. The constant asymptotic behavior of any FOM based on the reciprocal of R^2 multiplied by the time can be significantly delayed because of the small scoring efficiency in these tallies.

Fortunately, the user might not be interested in calculating the tally response below a certain threshold. For example, it might not be necessary to calculate the dose rates in the vicinity of a nuclear facility at locations where the dose rate because of the radiation sources is below the background level. In these cases, R of the mesh tally elements can be filtered below a specific threshold and the FOM can be based on R of the smallest tally above this threshold.

2.4 Hybrid Monte Carlo/deterministic techniques

While accurate 3-D deterministic modeling requires huge computational resources the computational requirements of some analog MC problems (eg. deep penetration problems) are strictly prohibitive. Non-analog MC requires the manual development of the VR parameters- a process often viewed to be more art than science and is very difficult for large and complicated problems [38].

Techniques that couple both the MC and the deterministic methods are known as the hybrid techniques. These techniques use the information obtained from computationally inexpensive deterministic calculations to distribute the particles advantageously through the phase-space domain of the MC problem and hence increase the MC calculation efficiency [39]. The solutions of both the forward and the adjoint transport equations have been used in the hybrid techniques. A brief discussion of some efforts in coupling the deterministic and the MC methods for neutronics shielding simulations is presented in the next section.

2.4.1 Literature review

The perturbation theory, first proposed by E. P. Wigner during the Manhattan project, introduced the adjoint flux concept for studying fundamental quantities in nuclear reactors such as the reactivity worth of difference materials in the reactor core [40]. Because the adjoint flux represents the phase-space importance to a certain response, it was extensively used in non-analog MC calculations. Inspired by the work of John Von Neumann and Stanislaw Ulam and with the emphasis of reducing the amount of work needed to perform the MC simulation, Kahn described the importance sampling technique and showed the theoretical existence of the zero-variance MC simulation scheme. Kahn modified the probabilities of contribution and death using an importance function. He suggested the use of some approximate analytic, numerical, or experimental procedures to calculate the importance function. He also indicated the possibility of interchanging the roles of the "normal" (forward) and adjoint equations in the MC simulations and correcting both the importance function and the MC results (tally) through iterating between the normal and adjoint simulations [41].

Because finding the exact adjoint (importance) function is too much to expect, Goertzel and Kalos suggested "the use of good intuition in selecting a physically plausible importance function with the hopes of significant decrease in variance over a more naïve game" with the absolute ignorance of the importance function [42]. Later in 1963, Kalos demonstrated the benefits of importance sampling by using analytic approximations of the adjoint flux representing the importance function. He showed that choosing from the altered transport kernel can be "facilitated, in part, by particle splitting" and Russian roulette and successfully reproduced the MC results in a 179 mean free path 1-D MC problem [43]. In 1967, the merits of

using the adjoint flux for the importance function were demonstrated by Coveyou et al. who investigated several biasing techniques namely, source biasing, implicit capture, and density (splitting and Russian roulette at certain events) biasing for deep penetration problems. Coveyou et al. developed an inverse relation between particles weights and the importance function and used this importance function for source and density biasing [44].

The early work by Kalos and Coveyou explained the benefits of using the adjoint fluxes for importance functions of non-analog MC simulations but the demonstration was limited to simple problems due to the limited computational power. As computational power increased and production-level deterministic and MC codes became available, the use of the hybrid techniques expanded to more realistic problems. The production-level implementations of the hybrid techniques started in the Oak Ridge National Laboratory (ORNL) Standard Computer Analysis for Licensing Evaluation (SCALE) package [45]. Tang and Hoffman automated the procedure for an adjoint calculation, biasing parameters generation, and non-analog MC calculation in the SAS4 [46] module of SCALE. The multigroup MC code, MORSE-SGC/S [47] was used for the MC calculation and the one-dimensional S_N code XSDRNPM-S [48] was used for the adjoint calculation. A one-to-one correspondence was imposed between the XSDRNPM-S zones and the MORSE-SGC/S regions. They used the zone-averaged and group-dependent adjoint flux calculated by XSDRNPM-S for the importance function and explained the use of this function for source energy biasing, energy biasing at collision sites, splitting and Russian roulette, and exponential transform [49]. The commercial MC code, MCBEND uses a 3-D adjoint diffusion code to automatically generate a space- and energy- dependent importance map in an orthogonal XYZ or $R\theta Z$ mesh [50]. The principal method of VR in MCBEND is the use of splitting and Russian roulette under the control of the importance map [51]. The French Monte Carlo code,

TRIPOLI [52] uses a deterministically evaluated importance function for several biasing schemes, including source biasing, exponential transform, and biasing at collision sites. For automating the use of the analytically developed importance map in biasing, the phase-space domain of the MC model is discretized in a 3-D grid and several energy groups. Using the Dijkstra algorithm [53], the analytic importance function is computed for each cell and energy group [54].

MCNP has frequently been coupled with specifically developed deterministic solvers or production-level deterministic solvers for automating the process of variance reduction. Several attempts successfully demonstrated large boosts in the simulations efficiencies compared to analog and manual non-analog MCNP calculations [55]. One of the first attempts of coupling MCNP with a deterministic solver was demonstrated by Mickael. Mickael used a short analog simulation to obtain the effective groups parameters of the time-dependent adjoint diffusion equation. A finite differencing scheme is used to solve the set of difference equations derived from the adjoint diffusion equation on a 1-D or 3-D grid. At any point in space, time, and energy, the adjoint flux is calculated using logarithmic interpolation on the grid. The particles' weights based on this interpolated (continuous) adjoint fluxes are used during the histories simulations [56]. Gardner and Liu combined Mickael method with the MCNP geometry independent (mesh-based) WWG, originally developed by Liu and Gardner [25]. They showed that the converged FOMs, after several iterations, are consistently larger when the initial importance map is based on the diffusion deterministic calculation rather than obtained from an analog MC calculation [57]. In LANL, the AVATAR method was developed to automatically invoke THREEDANT [58] for a 3-D deterministic adjoint calculation on a mesh independent of the MC geometry, calculate WWs, and run MCNP. AVATAR inverts the scalar adjoint fluxes to

get the lower WW boundary in each mesh element and each group. The weights are then normalized so the source particles are born with weights inside the WW. Van Riper et al. stated that using the full angular adjoint information, which THREEDANT can produce, will require an inordinate amount of storage. The angular component of the adjoint flux was approximated with the assumption of a separable angular variation that is symmetric about the average adjoint current. The WWs were normalized to a particular source location and energy, and consequently the inherent coupling between source and transport biasing is not taken into account [59]. An AVATAR-related effort was applied using the 3-D unstructured-mesh S_N code, Attila. Because of the intensive calculations required by the weight-checking algorithm in unstructured grids, the fluxes were interpolated to develop structured mesh weights-windows maps [16].

In an assessment of the MCNP WW, the incompatibility between source and transport biasing has been shown to be problematic due to calculation inefficiency and false convergence [60]. Responding to this issue, the CADIS method was developed by Wagner and Haghighat. The CADIS method uses the adjoint fluxes for automatic variance reduction of MC calculations through source biasing and consistent transport biasing with the WW technique [61]. The implementations of the CADIS method included algorithms for automatic generation of deterministic adjoint functions and algorithms for generation and usage of space- and energy-dependent source biasing and WW parameters [2]. The CADIS method was implemented into the Automated Adjoint Accelerated MCNP (A^3MCNP) code [62] and the AutomateD VAriaNce reducTion Generator (ADVANTG) code [63; 64]- both based on MCNP. A^3MCNP uses the S_N code, TORT [9] and ADVANTG can be linked to either TORT or the S_N code Denovo [11] for the deterministic calculation. A^3MCNP uses a specifically developed mesh-based WW algorithm that allows discontinuous mesh while ADVANTG writes a

geometry-independent (mesh-based) WW file that is directly usable by the RSICC version of MCNP5. The CADIS method was also implemented in the Monaco with Automated Variance Reduction using Importance Calculations (MAVRIC) sequence [33; 65; 66]. MAVRIC replaced SAS4 as the primary shielding analysis sequence of SCALE6 [67]. MAVRIC uses the multigroup MC code Monaco [33] for the MC calculations and the S_N code Denovo [11] for the deterministic calculations.

In an unreleased version of MCNP, the deterministic adjoint WW generator (DAWWG) was developed. DAWWG employs the PARTISN [8] multi-group S_N code to generate mesh-based WWs. The adjoint fluxes from PARTISN are converted to WWs for MCNP by taking the inverse of the adjoint flux, normalizing the WWs to the WW in the reference mesh. The angular WW concept was taken from AVATAR. The WWs also provide source energy biasing in a way similar to the CADIS method. For sources that span multiple mesh cells, DAWWG does not provide spatial biasing to the source particles which leads to inefficiencies in the method [55].

Turner and Larsen developed the Local Importance Function Transform (LIFT) as a practical approximation to the zero-variance method for contributions [68]. In Turner and Larsen's demonstration, the adjoint calculations were performed on an orthogonal grid using the diffusion method [69]. The LIFT method approximates the adjoint solution using a piecewise-continuous function containing parameters obtained from the adjoint calculation. The transport and collision processes of the transformed MC problem bias the source distribution, the distance to collision, and the selection of post collision energy groups and directions. Similarly in the University of Michigan, Cooper and Larsen developed an automated WW method for global MC calculations. In such a hypothetical global MC calculation, the flux estimates are desired at

all points in phase-space. The method developed by Cooper and Larsen is based on the use of WW that distributes MC particles uniformly throughout the system. The WW is constructed from an approximate deterministic solution of the forward transport problem [70].

For optimizing distributions (e.g., mesh tallies over all or part of the problem space) or multiple localized detector regions, an extension of the CADIS method was developed in ORNL. The Forward Weighted CADIS (FW-CADIS) method involves determining a function that represents the importance of particles to the objective of achieving uniform MC particle density in the desired tally regions [3]. The name, Forward Weighted, stems from the fact that the method involves weighting the adjoint source strength with information from a forward solution. The FW-CADIS method, therefore, involves two deterministic calculations: one forward and one adjoint. The FW-CADIS method was implemented in both ADVANTG and MAVRIC.

Becker developed methods to control the distributions of MC particles throughout the phase-space MC domain using a user-specified particle distribution such as the contributon flux. Becker used two approaches to achieve the user-specific particle distribution. The first is a WW approach which imposes a requirement on the MC particle distribution without changing the underlying physics. The second is the transform approach which comprehensively uses many biasing techniques to modify the particle physics. Becker's two approaches still use the standard biasing techniques such as source biasing, path length (exponential) biasing, collision biasing, and WWs but the biasing techniques are not viewed as individual techniques that can produce better results; rather, they are seen as elements of comprehensive tool set to distribute MC particles in a user-specified way [71].

The rest of this thesis focuses on the two hybrid methods CADIS and FW-CADIS. These two methods use the deterministically evaluated adjoint fluxes to develop the VR parameters for the MC calculations. The next section describes the fundamental theory behind using the adjoint flux in MC VR.

2.4.2 Importance sampling

The use of the adjoint function in MC VR has had a long history that is almost as old as the MC method itself [72]. The MC calculations can be thought as methods of solving integrals using random sampling procedures. The role of the adjoint function in MC VR can be illustrated by considering the integral form of the transport equation,

$$\psi(p) = \int K(p' \to p)\psi(p')dp' + q(p). \tag{2.30}$$

The transport kernel $K(p' \to p)$ is defined such that $K(p' \to p)dp$ is the probability of a particle emerging in dp about p from an event in dp' about p'. This kernel can be thought as composed of a collision kernel $C(\overline{r'}, E' \to E, \widehat{\Omega'} \to \hat{\Omega})$ and the streaming kernel $T(\overline{r'} \to \bar{r}, E, \hat{\Omega})$. MC methods have specific sampling procedures for each of these kernels. With non-analog MC, the MC game can be altered by changing the probability densities from which each event is sampled. The modification of the transport kernel is necessary to depict this alteration since the changes from analog random sampling (for e.g splitting and rouletting) take place at certain transport events. The source emission probability can also be altered to depict any non-analog sampling in the MC simulation [43].

Equation (2.30) can be modified by multiplying with an arbitrary function $I(p)$ which is positive everywhere. If we define an altered source function,

$$\hat{q}(p) = I(p)q(p), \tag{2.31}$$

and an altered flux,

$$\hat{\psi}(p) = \psi(p)I(p). \tag{2.32}$$

Eq. (2.30) will be transformed to

$$\hat{\psi}(p) = \int \hat{K}(p' \to p)\hat{\psi}(p')dp' + \hat{q}(p). \tag{2.33}$$

The altered transport kernel will be

$$\hat{K}(p' \to p) = K(p' \to p)\frac{I(p)}{I(p')}, \tag{2.34}$$

which is proportional to the ratio of the value of the arbitrary function at the phase-space of a single event to its value at the phase-space of the last event.

Equation (2.33) is similar to the original integral transport equation (Eq. (2.30)) with three changes:

1. The source function is replaced by a modified source function.
2. The transport kernel is modified by the ratio of the arbitrary function values at the phase-space of this event and the last event.
3. The phase-space dependent flux is replaced by the product of the original flux and the arbitrary function.

This suggests a modified sampling scheme for both particles emitted from the source and particles that go through the transport events. The number of particles sampled from the source or in the transport events is proportional to the arbitrary function $I(p)$. According to Eq. (2.13), the weights of these particles have to be adjusted for the MC final answer (tally result) not to be biased.

Equation (2.9) can be thought as an integral equation describing an extremely efficient MC process that calculates a tally response TR. In this MC calculation, the source particles immediately contribute to the tally response without going into any physical events. To find an optimum choice for the function $I(p)$, Eq. (2.9) should be solved with Eq. (2.31) taking into account that the MC calculations require that the source be defined as a PDF (i.e. $\int \hat{q}(p)dp = 1$),

$$I(p) = \frac{\psi^+(p)}{TR}. \tag{2.35}$$

$I(p)$ is directly proportional to the phase-space dependent adjoint flux. Because of the physical interpretation of the adjoint flux, the altered kernel and source function have the reasonable property of distributing as many particles in phase-space as the expected contribution (importance) of each phase-space position to the detector. The modified sampling technique that uses this "importance function" is often known as "importance sampling" [42]. It is worth mentioning that this importance function is not directly related to the statistical metrics used to characterize the efficiency of the MC simulation such as the variance or the FOM [73]. Despite this fact, it is still logical to advantageously distribute the particles throughout the phase-space regions of the system.

Theoretically, if $I(p)$ is exactly known, the modified sampling process will lead to a MC result with zero-variance since all the histories will have the same score. MC codes use different

methods to count the tally scores such as track length estimators, collision estimators, and last event estimators. It has been proven that for all MC estimators, this modified sampling scheme can provide a zero-variance solution with some adjustments to the adjoint source functions [72]. In practice the solution of the adjoint equation is as difficult as the solution of the transport equation itself. If the importance function is exactly known, performing the random sampling process will not be needed because it will be easier to calculate the response using integration methods (Eq. (2.9)). However, an approximate estimate of the adjoint function can significantly decrease the MC variance if the suggested modified sampling scheme was used in the MC calculation. Many hybrid MC/deterministic techniques, including CADIS and FW-CADIS, use approximate (fast) adjoint deterministic calculations to provide the MC calculations with the phase-space dependent importance function. As a consequence of using this modified sampling technique that approximates a zero-variance solution, the efficiency of the MC calculations depends on the accuracy of the deterministically calculated fluxes in CADIS and FW-CADIS simulations.

The modified source PDF suggested by the importance sampling scheme can be deduced by solving Eq. (2.35) and (2.31),

$$\hat{q}(p) = \frac{q(p)\psi^{+}(p)}{TR}. \tag{2.36}$$

This is advantageous since the number of source particles sampled in any phase-space region is proportional to the region contribution to the detectors.

The particles flux in non-analog MC simulations ($\hat{\psi}$ in this modified sampling scheme) is often denoted as the MC particles flux ψ_{MC}. From Eq. (2.35) and Eq. (2.32), the MC particles flux simulated using the importance sampling scheme can be expressed by,

$$\psi_{MC}(p) = \frac{\psi^{+}(p)\psi(p)}{TR}. \quad (2.37)$$

Equation (2.37) shows that importance sampling tend to populate the MC particles according to the contributon flux $c(p) = \psi^{+}(p)\psi(p)$ [6]. This is advantageous because the contributon flux has higher values in phase-space regions that are more important to the solution of the problem. The LIFT method approximates an analog Monte Carlo simulation of the contributon fluxes by altering the MC transport mechanics with an approximate solution for the adjoint fluxes [68]. The methods developed by Becker and Larsen disperse the MC particles throughout phase-space according to user-specified distribution such as the contributon flux [71]. Since the CADIS and the FW-CADIS methods apply this importance sampling technique using deterministically calculated adjoint fluxes, these methods tend to populate the MC particles in phase-space regions according to the contributon flux.

The next chapter describes the efficiency and reliability of two hybrid MC/deterministic methods, CADIS and FW-CADIS which are based on the same theory described in this section.

Chapter 3: CADIS and FW-CADIS

3.1 Methods description

The CADIS method provides consistent formulations for source and transport biasing parameters and their implementation within the WW technique [2]. The biased source distribution, $\hat{q}(\bar{r}, E)$ is given by,

$$\hat{q}(\bar{r}, E) = \frac{\phi^{+}(\bar{r},E)q(\bar{r},E)}{TR}, \tag{3.1}$$

where TR is the total detector response given by Eq. (2.7) and Eq. (2.9), $q(\bar{r}, E)$ is the unbiased source distribution, and $\phi^{+}(\bar{r}, E)$ is the scalar adjoint flux. Equation (3.1) is similar in form to Eq. (2.36) if the angular variations are considered. Direction-based CADIS has been implemented and used in limited applications [74], but it will not be considered in this thesis. The reason for this similarity is that the biased source PDF of the CADIS method is derived from the same importance sampling procedure described in Sec. 2.4 [2]. By sampling from the biased source distribution, source particles are sampled in proportion to their expected contribution to the detector response.

For the transport biasing, the WW technique is employed. In MCNP, the WW input requires lower WW bounds w_l. The width of the window is controlled by the input parameter c, which is the ratio of upper and lower WW bounds ($c = {}^{w_u}/_{w_l}$). The space- and energy-dependent WW lower bounds are given by,

$$w_l(\bar{r},E) = \frac{TR}{\phi^+(\bar{r},E)\left(\frac{c+1}{2}\right)}. \quad (3.2)$$

In the CADIS method, the source and transport biasing parameters are consistent. The source particles, which are sampled from the biased source distribution of Eq. (3.1), start with statistical weights w_0,

$$w_0(\bar{r},E) = \frac{TR}{\phi^+(\bar{r},E)}.$$

These weights are within the WWs as desired. This consistency eliminates the incompatibility between the source and transport biasing that was problematic in previous approaches leading to poor efficiency and/or false convergence [60]. Furthermore, for problems in which the adjoint (importance) function varies significantly within the source phase-space region, the source biasing is very effective for improving computational efficiency [23; 2].

As noted in Sect. 2.1, the adjoint source has to be defined as the response function for the adjoint flux to represent the importance of each phase-space region to a desired response. For the CADIS method, the user specifies an adjoint source with space and energy distributions similar to the tally to be optimized.

The CADIS method is effective for optimizing classic source/detector problems for which the adjoint source has to be specified at a single location and has to have a specific response. For simultaneously optimizing distributions (mesh tallies) or multiple responses (multiple tallies) for which the responses vary significantly over the phase-space regions of the tallies, the CADIS method did not prove to be as successful. When multiple adjoint sources corresponding to multiple tallies are specified, the tally closest to the true physical source converges faster showing that the closest adjoint source is attracting more particles. Specification

of the adjoint source at the furthest region from the physical source encourages the MC particles to move further but raises concerns regarding the convergence reliability in the inner regions of the problem. The hybrid method, developed by Cooper and Larsen, which uses the inverted forward flux as an importance function in an attempt to distribute the MC particles uniformly throughout the system, demonstrated its benefit for global MC calculations [70]. Although this method encourages particles to move toward regions of lower flux and discourages particles from moving toward regions of higher flux, when applied to large realistic applications where the desired tally regions are a subset of the total problem space, the method tends to have slow convergence because of distributing the particles in undesired regions [3].

For the simultaneous optimization of several tallies or the cells of a mesh tally, the FW-CADIS was developed in ORNL. In the FW-CADIS method, the source biasing and WW parameters are calculated from the adjoint fluxes using the same procedures as for the CADIS method but the deterministic adjoint calculation is preceded by a forward deterministic calculation that estimates the space-dependent response in the required tally regions [3]. The source of the adjoint deterministic calculation is represented by the user-specified adjoint source (tally cross section) weighted by the inverse of the response estimated from the forward deterministic calculation. In other words, the adjoint source in a FW-CADIS calculation would be,

$$q^{+}(\bar{r},E)=\frac{\sigma_d(\bar{r},E)}{\int_E \phi(\bar{r},E)\sigma_d(\bar{r},E)dE}. \tag{3.3}$$

Weighting the adjoint source by the inverse of the total response estimate, the adjoint source strengths and thus the adjoint fluxes (importances) will be higher at regions further from

the physical source. This tends to distribute the MC particles uniformly throughout the tally regions [3].

The practicality and usefulness of the hybrid techniques are determined by their time savings compared to using either the deterministic or the MC methods individually. The manual creation of the input files for deterministic transport codes require substantial familiarity with deterministic methods and can be very time consuming. In both MAVRIC [33] and ADVANTG [64], the user only specifies the mesh boundaries and the adjoint source description. Based on these inputs and MC geometry, the codes automatically create the deterministic input files and run the deterministic calculations. Since only approximate deterministic solutions are needed to develop reasonable WW maps and source biasing parameters, the deterministic calculations do not need to fully resolve the phase-space domain. The deterministic mesh needs to capture significant material changes and geometrical details but does not need the fineness required of a stand-alone deterministic calculation [75].

3.2 Applications

Table 3.1 summarizes the objective and the number of deterministic calculations needed by each of the CADIS and the FW-CADIS methods.

Table 3.1: Uses of CADIS and FW-CADIS and deterministic calculations involved [75]

Method	Use	Deterministic calculations
CADIS	Optimization of localized detector (tally) regions	Adjoint
FW-CADIS	Optimization of distributions (mesh tallies) or multiple localized detector regions	Forward and adjoint

For over a decade, the CADIS method has been used in a variety of shielding applications involving neutron, gamma, and coupled neutron-gamma source-detector problems [75]. Table 3.2 shows examples of the problems the CADIS method has been applied to and the observed speed-ups.

Table 3.2: Examples of applications and associated speed-ups of CADIS [75]

Application	Observed speed-up relative to analog[4] MC
PWR cavity dosimetry	$O(10^4)$
DPA in BWR core shroud	$O(10^3)$
Neutron well-logging tool	$O(10^2)$
Gamma well-logging tool	$O(10^{3-4})$
Dose from single spent fuel storage cask	$O(10^{3-4})$
PWR ex-core thermal detector response	$O(10^4)$
Passive threat detection	$O(10^{2-4})$
Active-interrogation detection	$O(10^4)$
ITER shielding	$O(10^{2-4})$
HFIR DPA calculations	$O(10^4)$
Criticality accident alarm system analyses	$O(10^{2-3})$

[4] MC simulations that are identified as “analog” or “without variance reduction” usually still include the standard implicit capture method. For comparing the efficiency of these MC simulations with CADIS or FW-CADIS, the implicit capture was not switched off since the CADIS and the FW-CADIS calculations were also combined with the implicit capture. Implicit capture is switched on by default in MCNP and many other MC codes.

For the past few years the FW-CADIS method has been used in a variety of neutron, gamma, and coupled neutron-gamma fixed-source problems in which the results are sought throughout large portions of the problem space or at multiple detectors. Table 3.3 shows examples of problems to which the FW-CADIS was applied. The enhancement in the MC FOM is not specified since a MC FOM for global MC problems has not yet been established. In many cases it is either very difficult or impossible to obtain meaningful results with analog MC, and hence the speed-up is clearly very large but was not quantified [75].

Table 3.3: Examples of applications of FW-CADIS [75]

Application
Dose rate throughout full-scale PWR facility
Multiple detector responses in nuclear well-logging tools
Site boundary dose rate from an array of spent fuel casks
ITER shielding and material heating analysis
Dose rates throughout a critical facility
Dose rates throughout an urban model from a nuclear weapon detonation
Dose rates throughout IRIS reactor containment

The noticeable success of CADIS and FW-CADIS can be attributed to four reasons: (1) the consistency between the source and transport biasing, (2) the automation of the creation of the deterministic input file, (3) the automation of the generation of the space- and energy-dependent source biasing and WW parameters, and (4) the use of mature production-level S_N codes such as Denovo [11] and TORT [9].

3.3 Efficiency and reliability of CADIS and FW-CADIS

As mentioned in Sect. 2.4.2, the efficiency of the MC calculations depends on the accuracy of the deterministically calculated fluxes in CADIS and FW-CADIS simulations. In Sect. 2.3.3, it was noted that the VR techniques can be abused so that some phase-space regions are not well sampled and/or other regions are so heavily sampled in excess to their importance to the MC calculation. This can cause the calculation of seemingly acceptable MC results that is far from being realistic (unreliable). The deterministically calculated VR parameters of CADIS and FW-CADIS can have an overall span of tens of orders of magnitude. This increases the risk of producing inaccurate and unreliable results because of the undersampling and instability issues discussed previously. This section discusses the efficiency and reliability issues of CADIS and FW-CADIS simulations.

Before discussing the efficiency and reliability of the CADIS and FW-CADIS methods, two of their important features have to be considered. First, coarse meshes are usually used with CADIS and FW-CADIS simulations due to the limited availability of computing resources for the deterministic calculations. Another limitation for the CADIS and FW-CADIS mesh resolution is the storage size of the VR parameters. Since the WW are developed using the same mesh and energy groups' structure of the deterministic calculation, the mesh used for CADIS and FW-CADIS deterministic calculation has to be limited by the storage size of the WW file[5]. Production-level MC codes (e.g. MCNP) depend on replication of the MC data (geometry, cross-sections, VR parameters, etc.) for parallel processing rather than domain-decomposition [76].

[5] The WW file, wwinp is the file written by ADVNATG for MCNP. The same argument supported in the text can be extended to the mesh important map file for SCALE/MAVRIC.

Running parallel MC calculations is often difficult for CADIS and FW-CADIS simulations because of the large amount of computer memory that needs to be allocated for each processor. For large and complicated problems, the deterministically calculated VR parameters may require several gigabytes of memory even with $O(10^{2-3})$ fewer elements than the mesh needed to solve the problem deterministically. Second, the manual creation of the input files for deterministic transport codes requires substantial familiarity with deterministic methods and can be very time consuming. The deterministic input files have to be automatically developed for any successful implementation of CADIS and FW-CADIS. Capturing all physical and geometrical details in the CADIS and FW-CADIS deterministic calculations cannot be guaranteed with these coarse, automatically generated meshes. Inconsistencies between the deterministic and the MC models in CADIS and FW-CADIS simulations can significantly decrease the MC calculation efficiency and, if severe, they can cause inaccurate and unreliable MC results. This will be demonstrated in the next examples.

Each of the next examples focuses on a different aspect of the effects of the deterministic and the WW meshes on the efficiency and reliability of CADIS and FW-CADIS simulations.

3.3.1 ITER toroidal field coils heating

This example shows how severe inconsistencies between the deterministic and the MC models in CADIS and FW-CADIS simulations can cause the MC calculations to be inaccurate and unreliabile. The example explains some circumstances that occurred during the calculation of the nuclear heating in the inboard (IB) leg of the toroidal field coils (TFC) of ITER. The nuclear heating in the IB TFC represents one of the main drivers of the shielding design of ITER.

The details of this calculation, which are not pertinent to this thesis, can be found in Ref. [77; 78].

Problem description

Each of the IB TFC legs has a height of 8 m, a radial thickness of 70 cm, and a toroidal extent of 80 cm. The simplified computer aided design (CAD) model of Fig. 3.1 shows the IB TFC of ITER together with the shielding layers separating them from the neutron source in the deuterium tritium (D-T) plasma region. The IB leg of the ITER TFC was divided into 10 segments for assessing the nuclear heating profile.

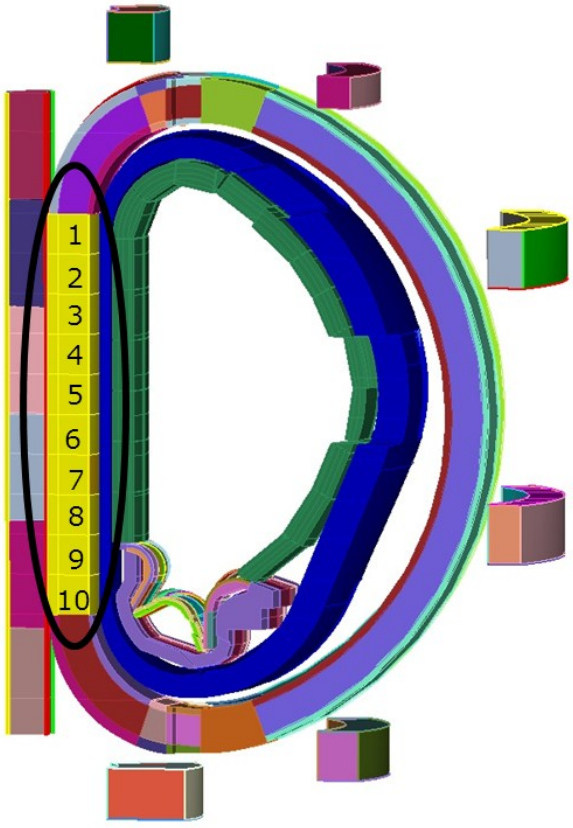

Figure 3.1: Inboard (IB) toroidal field coil (TFC)

For the analysis in this thesis, the nuclear heating was calculated at the lower IB TFC segment, denoted as segment 10 in Fig. 3.1.

Methodology

The ITER model used in this analysis represented a 40° sector of the ITER machine with reflecting boundaries. The MC calculations in this analysis used the University of Wisconsin-Madison (UW-Madison) CAD based MC code, Direct Accelerated Geometry MCNP (DAGMCNP) [79]. DAGMCNP is a MC code that replaces the ray tracing routines of MCNP with CAD routines defined in an external software library. It has been extensively used in the neutronics analysis of several fusion applications such as ITER, HAPL, and ARIES [80]. The CAD model used in the DAGMCNP analysis model had a 5 cm gap at each side of the vacuum vessel (VV) in the toroidal direction. The gap extended all the way through the IB VV.

ADVANTG was used to apply the FW-CADIS method to optimize the fluxes at all the 10 IB TFC segments. The adjoint source was specified to be the total neutron and gamma heating in a rectangular parallelepiped enclosing all the IB-TFC segments in the MC model. ADVANTG used a native MCNP input file, for generating the Denovo models of the FW-CADIS calculations. This input file, which did not have the 5 cm gap surrounding the VV, was created from the ITER CAD model by the Karlsruhe Institute of Technology (KIT) using the McCAD translator [81]. The WWs developed by ADVANTG were then used with the subsequent MC simulations that used the DAGMCNP model, which had a gap in the VV. Figure 3.2 shows a simplified version (only VV and void) of the two ITER models used for the DAGMCNP simulation and the ADVANTG WW creation.

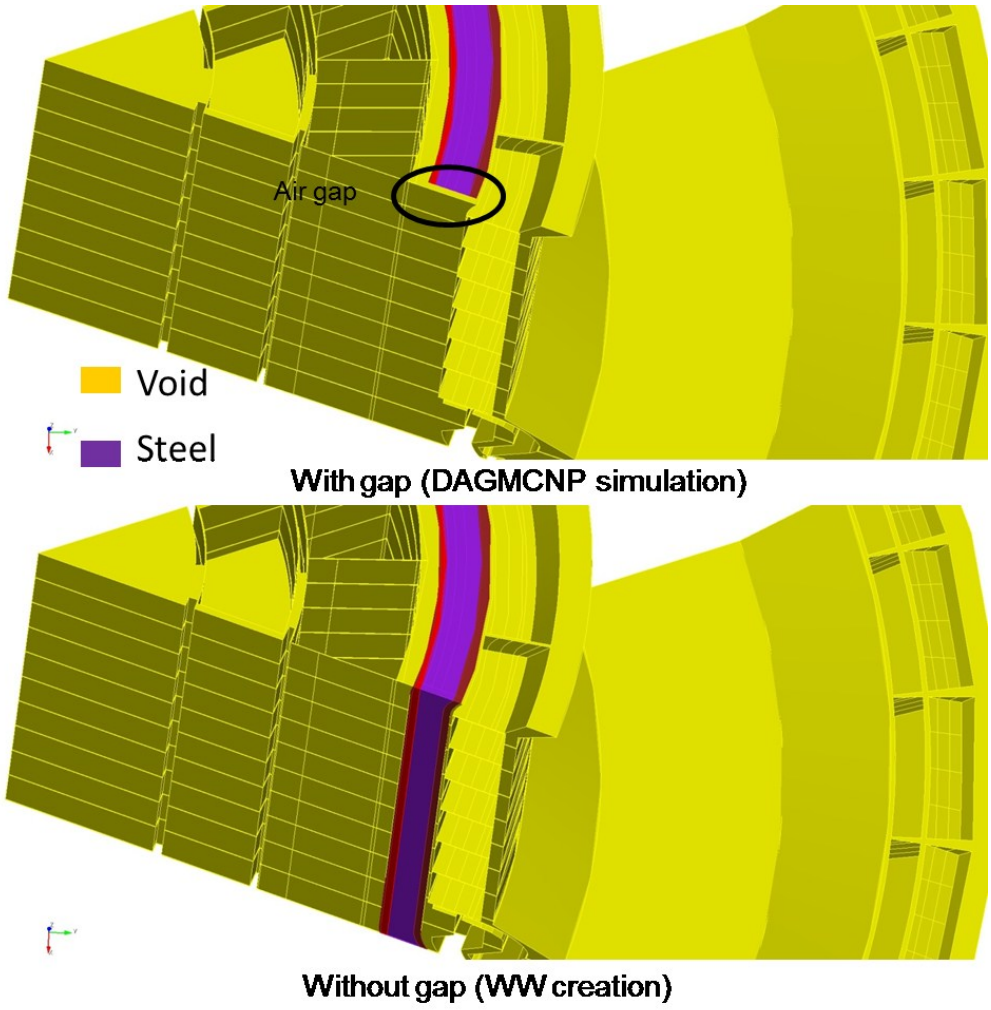

Figure 3.2: ITER model with and without the air gap in the VV

The IAEA fusion evaluated nuclear data library (FENDL-2.1) [82] was used in this analysis. A continuous energy library was used for the DAGMCNP calculations and a multi-group 46 neutron/21 gamma library for the Denovo calculation.

Results

While the inconsistency between the deterministic and the MC models impacted the accuracy of the tally mean, that has been discussed elsewhere [78] and is not the topic of this analysis. Rather, this example provides a very clear demonstration of the risk of obtaining unreliable results because of the conceivable inconsistencies between the deterministic and the MC models in CADIS and FW-CADIS simulations.

Erratic uncertainties appeared in the MC tally results of the FW-CADIS simulation. Table 3.4 shows the tally fluctuation chart of the DAGMCNP calculation of the nuclear heating in the lower IB TFC segment.

Table 3.4: DAGMCNP tally fluctuation chart for one of IB TFC segments

nps	mean	error	vov	slope	fom
128000	2.58E-02	0.1801	0.3847	2.2	3.10E-01
256000	2.81E-02	0.1147	0.144	3.2	3.50E-01
384000	2.84E-02	0.0935	0.0792	2.9	3.60E-01
512000	2.83E-02	0.0798	0.0583	2.8	3.70E-01
640000	2.62E-02	0.0706	0.0529	2.9	3.90E-01
768000	2.71E-02	0.0697	0.0528	2.7	3.30E-01
896000	2.68E-02	0.063	0.045	3	3.50E-01
1024000	2.65E-02	0.0577	0.0398	2.8	3.50E-01
1152000	2.64E-02	0.055	0.0344	2.7	3.50E-01
1280000	2.60E-02	0.0516	0.0314	2.5	3.60E-01
1286701	3.85E-02	0.3194	0.976	2.3	9.30E-03

If one stops the calculation at 896,000 histories, the tally passes the 10 MCNP statistical checks. If one stops the MC simulation at 1,286,700 histories, then the tally passes all the 10 MCNP statistical checks except for the Pareto slope which was 2.58 (i.e close to the threshold 3).

Because of history number 1,286,701 the nuclear heating tally mean increased from 0.026 watt/cm^3 to 0.039 watt/cm^3, the R increased from 5.1% to 31.9%, the VOV increased from 3% to 97.6%, and the FOM decreased from 0.36 to 0.0093. With 1,286,701 histories, the tally failed 8 MCNP statistical checks. The mean heating value using 896,000 histories is 0.0267 watt/cm^3 is 30.6% smaller than the value with 1,286,701 histories which shows that the MC simulation using 896,000 histories is undersampled and inaccurate despite passing the 10 MCNP statistical checks.

Following the event log of history number 1,286,701, it was found that this particle had 4 consecutive 5:1 splitting events at the front insulation casing of the IB TFC segment. Before the consecutive splitting events, the last collision for this history occurred in one of the divertor cassettes. If the DAGMCNP model had not had the gap, the streaming of this particle with the relatively low energy (0.2 Mev) from the divertor cassette to the IB TFC casing would have been highly unlikely because the two regions would have been shielded by the 35 cm thick IB VV. Figure 3.3 shows a schematic view describing some of the events occurring to this history.

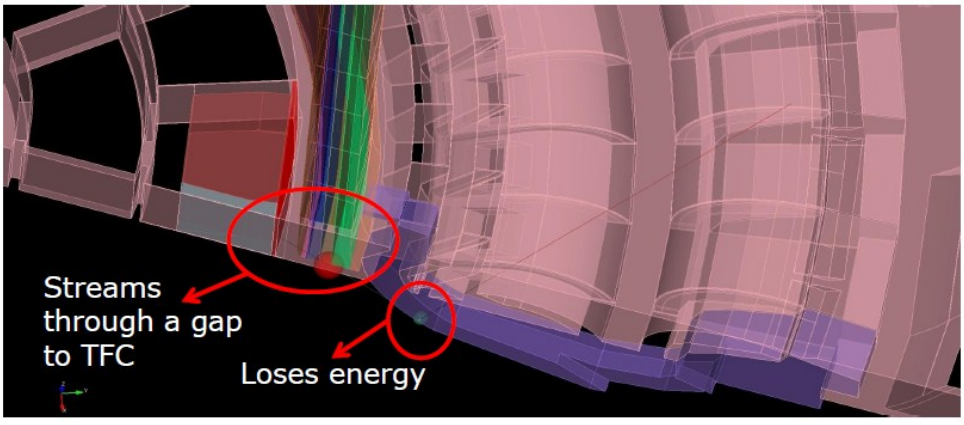

Figure 3.3: Events occurring to one history in IB TFC ITER problem

ADVANTG used the KIT native MCNP model, which did not have the VV gap, to create the WWs. The low energy neutrons in front of the VV were assigned high weights because, without the gap, they have a very low probability of reaching the IB TFC without splitting. These neutrons were harshly rouletted in front of the gap and their survival probability was very low. The high nuclear heating values because of neutrons streaming through the gap would not have been noticed if the calculation was stopped before particle 1,286,701. *This shows that unreliable MC results, including false indications of statistical quality and incorrect mean value, can be caused by severe inconsistencies between the deterministic and the MC models in CADIS and FW-CADIS simulations.*

3.3.2 Steel box with air pipes

This example shows how inconsistencies between the deterministic and the MC models in FW-CADIS simulations can decrease the efficiency of the MC calculation by slowing down its convergence.

Problem description

The simple model of Fig. 3.4 was designed to test the effect of the S_N mesh on the overall simulation efficiency of MAVRIC.

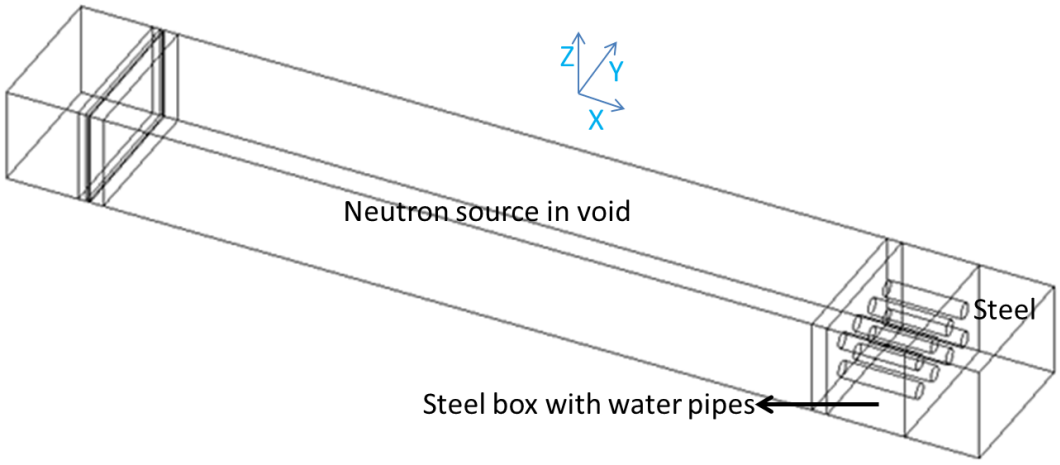

Figure 3.4: MAVRIC model for steel box with air pipes problem

The Monaco model had an isotropic neutron source uniformly distributed in a 475 cm×100 cm×60 cm rectangular parallel-pipe. The neutron source energy was uniform in the first group of the 27 neutron/19 gamma ENDF-VI library (6.38-20 Mev) [83]. The source was surrounded by steel boxes from both ends in the *X* direction. The dimensions of the box on the right were 48 cm in *X* direction, 100 cm in *Y* direction and 60 cm in *Z* direction. Eight air pipes, 10 cm in diameter, penetrated this box and went all the way through it in the *X* direction. Another steel box of similar dimensions covered this box from the other side of the source.

A uniform Cartesian mesh tally was used to tally the total neutron flux within the steel box with the air pipes. The mesh tally contained 2,880 total number of mesh cells. Each mesh cell was cubical with a side length of 5 cm.

Reflecting boundaries were mimicked by positioning the original model in the center of a lattice of nine similar models. The mesh tally was only used to tally the neutron fluxes in the center model.

Methodology

Two Cartesian mesh grids were used for the Denovo S_N calculations. The two grids were similar in every aspect except for a 5 cm shift in the *Y* and *Z* directions. Inside and around the mesh tally box, the grid had cubic elements with side length of 10 cm. Figure 3.5 shows the Denovo models for the steel box with the air pipes.

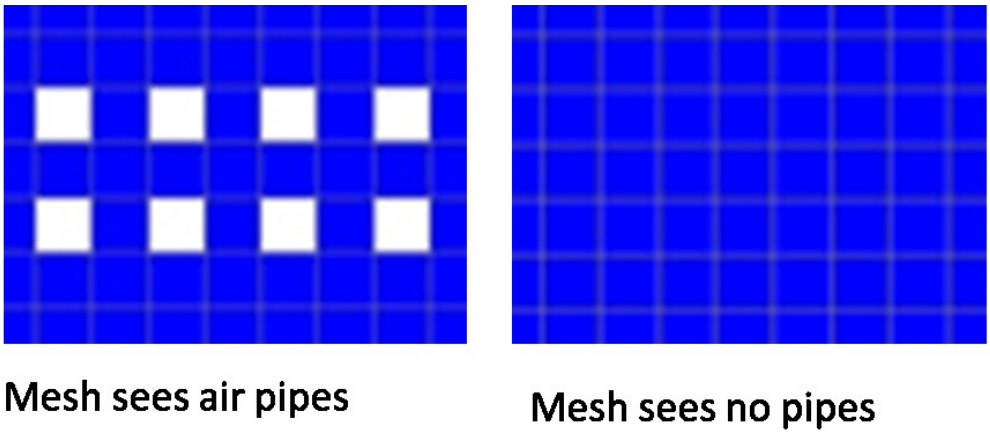

Figure 3.5: Denovo mesh for the steel box with air pipes problem

The materials definitions of the MAVRIC S_N calculations are based on the materials at the center of each mesh cell in the Monaco model. In the first grid, the circular cylindrical air pipes were transformed into rectangular parallel pipes having a square cross sectional area of side length of 10 cm and going all the way through the mesh tally box. The second grid completely missed the air pipes because none of the mesh cells' centers hit the pipes. The steel box, at which the neutron flux was tallied, did not have any penetrations in the S_N calculations of the second case. The Monaco model with the air pipes did not change for both cases.

Results

The importance map based on the first grid, with square air pipes, resulted in higher efficiency Monaco simulation. Figure 3.6 shows the CDF of the mesh tally uncertainties for 1-day Monaco runs with both of the importance maps based on the grid with the air pipes and the grid without the air pipes.

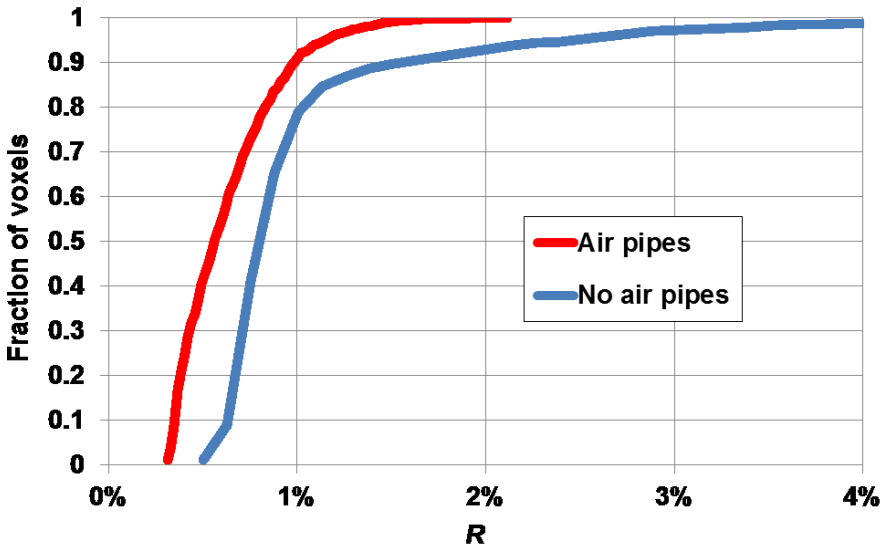

Figure 3.6: CDFs for steel box with air pipes problem

While the maximum *R* for the Monaco case that used the importance map based on the grid with the air pipes was only 2%, the maximum *R* for the other case without the air pipes was 13%. For every *R* below 13%, a larger fraction of voxels had relative uncertainties lower than this *R* with the FW-CADIS calculation for which the S_N model had the air pipes. The global MC FOM, defined by Eq. (2.29), of the first FW-CADIS case with the Denovo model that does not include the air pipes was 4.0 times lower than the FOM of the FW-CADIS case with the Denovo model that includes the air pipes. *This shows that in FW-CADIS the efficiency of the MC*

simulations are affected by the accuracy of the S_N fluxes and the ability of the S_N model to replicate the MC one.

The better efficiency of the FW-CADIS case with the air pipes was also noticed when the amount of splitting was counted for both cases. For every 2687 particles simulated with the grid without the air pipes, 1 particle was particle was split more than 1000 times in a single splitting event. For this grid, the fraction of particles which were split more than 1000 times in one splitting event was 4,320 times higher than the corresponding fraction for the S_N grid with the air pipes. The excess splitting indicates that the neutrons confront abrupt changes in the phase-space importance during the MC simulations using the importance map of the grid without the air pipes.

Figure 3.7 shows the total flux mesh tally results for both of the FW-CADIS cases on a transverse (*Y*-*Z*) plane that is separated by 40 cm from the front plane and 12 cm from the back plane of the steel box.

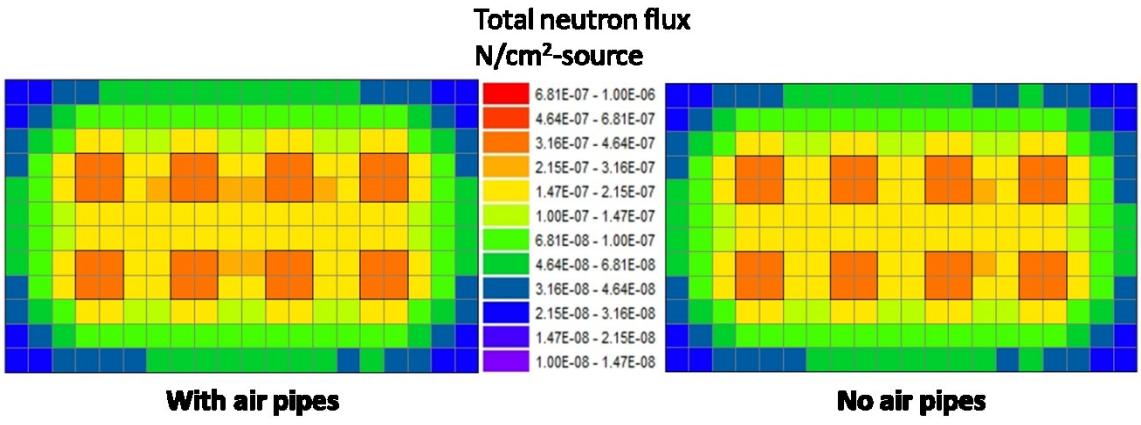

Figure 3.7: Total neutron flux mesh tally of steel box with air pipes problem

The differences between the total flux values of the two FW-CADIS cases exceeded 3σ for 15.2% of the mesh tally voxels. The maximum difference between the total flux values in terms of number of standard deviations of the FW-CADIS case with highest uncertainty was 9.1σ. Even though the reliability of MC tally results at these mesh elements with high differences cannot be guaranteed for either of the FW-CADIS cases, one would expect that the results of the FW-CADIS case with the more accurate Denovo model (with air pipes) is more reliable because of the smaller Rs.

3.3.3 High enrichment uranium active interrogation

This example shows the impact of increasing the total number of space-energy WW mesh elements on the MC FOM in CADIS and FW-CADIS simulations.

Problem description

Figure 3.8 represents a standard cargo container (2.44 m × 2.44 m × 6.10 m). The threat object is a 5 kg sphere of 95% enriched uranium (3.982 cm radius) placed at the center of the container and shielded by 2.35 m × 2.35 m × 2.35 polyethylene cube. The container is being irradiated by 14.1 MeV neutrons from a deuterium-tritium (D-T) generator.

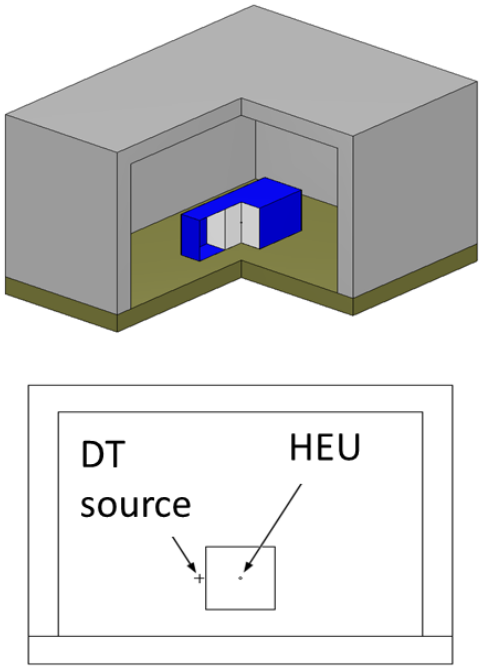

Figure 3.8: HEU active interrogation problem

Methodology

ADVANTG was used to employ the CADIS method to increase the MC efficiency in calculating the fission rate in the threat object. A 27-group neutron cross section library, derived from ENDF-VII data [84], was used for the Denovo calculation and a continuous-energy neutron data was used for the MCNP calculations. The adjoint source was defined as a sphere located at the same position and having the same diameter as the high enriched uranium (HEU) sphere. The adjoint source strength was defined as the HEU fission cross-section in the 27 group structure of the Denovo library.

A mesh with 19 planes in the *X* direction, 23 planes in the *Y* direction, and 19 planes in the *Z* direction was used for the initial deterministic calculation and the initial WW map. To analyze the effect of the total number of the WW space-energy elements on the MC FOM, the

initial deterministic mesh was refined by inserting a certain number of extra planes between each two adjacent planes in each direction. By changing the number of the inserted planes, the total number of mesh elements increased by a factor equal to the number of the inserted planes raised to the cubic power. The WW meshes of these cases, which will be known as "Full refinement" cases, used the same refined meshes of the deterministic calculations. In order to understand the impact of simply using WW maps with larger numbers of space-energy elements without changing the WW values, the WW mesh was refined separately without refining the deterministic calculation. The same weight of each cell in the initial unrefined WW map was used for all the corresponding newly inserted cells in the refined WW maps of these cases, which will be known as "WW refinement" cases.

Results

The calculated fission rate was between 3.0×10^{7} and 3.2×10^{7} fission/source-particle and all *R*s were between 1.0% and 3.2% for all the CADIS cases.

Figure 3.9 shows the variation of the MC FOM with the total number of space-energy elements for both the "Full refinement" and "WW refinement" cases.

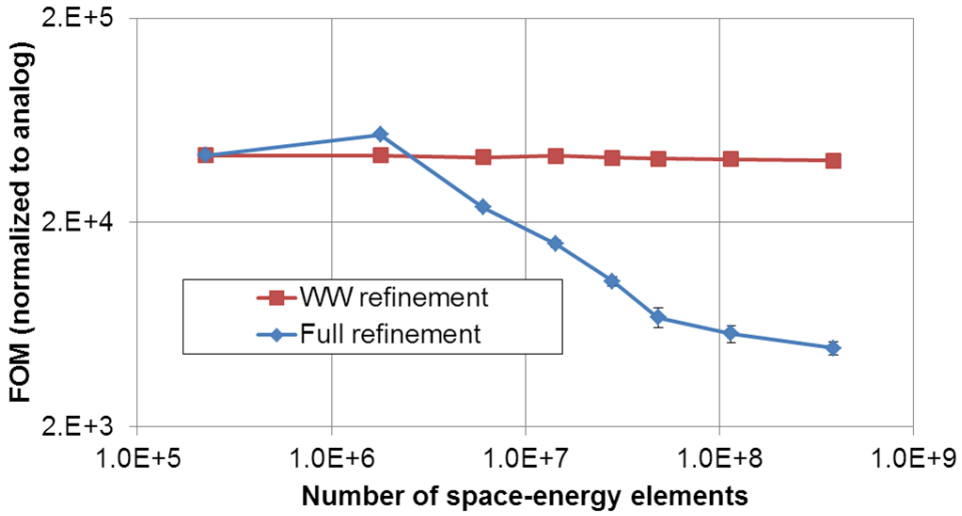

Figure 3.9: FOM variation with weight-window (WW) mesh for HEU active interrogation problem

As shown in Fig. 3.9, the decrease in the FOM due to the refinement of the WW without changing the adjoint fluxes did not exceed 5% even with a factor of 1,728 increase in the total number of cells in the WW map. This shows that, the computational costs of larger WW meshes, including the cost of the binary searches on the mesh, have small impact on the MC FOM if the WW values are not changed.

Even though finer deterministic calculations are expected to calculate more accurate fluxes, the FOM decreased by a factor of 8.76 due to refining the mesh of the deterministic calculation. As noted in Sect. 2.4.2, the importance function provided by Eq. (2.35) contains only information about the expected score of a MC particle. The decrease in the MC simulation efficiency can be attributed to the fact that the importance function does not contain any information about the variance introduced by the MC particles or the MC FOM. The effects of the WW values on the calculation cost, defined as the inverse FOM, of a MC calculation have

been recently studied by CJ Solomon [73; 85]. The work of CJ Solomon represented the first attempt at deterministic optimization of MC calculations with weight-dependent VR, but the demonstration of the applicability of such deterministic optimization has been limited to simple problems [85]. The algorithms developed in this thesis will not consider the effects of the WW values on the calculation cost of the MC calculations because of the excessive computer time and memory required to deterministically optimize the WW values of MC simulations of large and complicated problems.

3.3.4 Dose rate in proximity of high-intensity neutron generator

This example shows how the memory requirement of the MC calculation can represent the limiting factor of the deterministic mesh resolution in CADIS and FW-CADIS simulations.

Problem description

The MCNP model in Fig. 3.10 describes the control area (bunker) of a nuclear development facility that utilizes a particle accelerator to produce neutrons. The accelerator uses D-D fusion reactions producing 2.45 Mev mono-energetic neutrons. Water barrels with volumes between 0.5 and 1 m^3 are used for shielding. Estimate of the neutron dose rate outside of the bunker is necessary for determining the shielding configurations that minimizes the radiation dose for occupational safety. For simplicity, only neutrons were considered in this calculation.

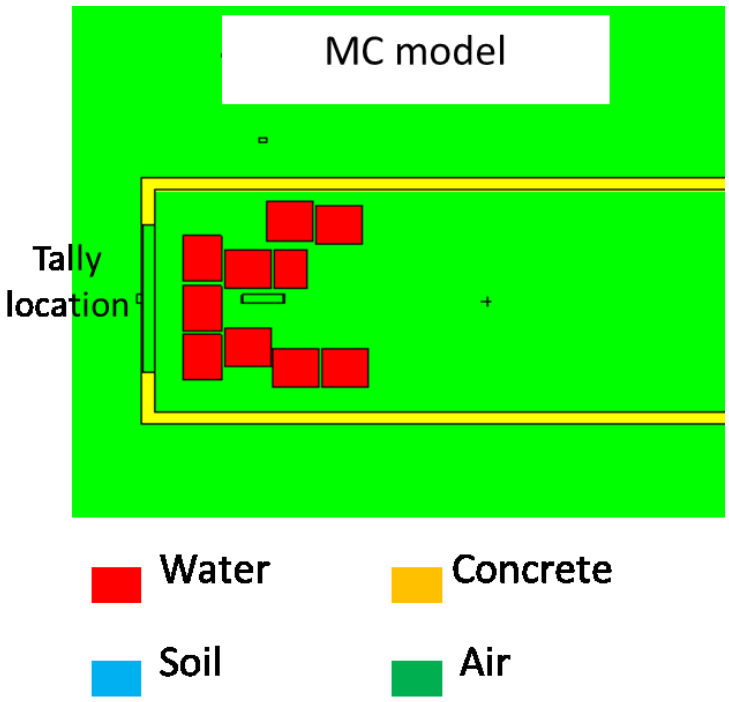

Figure 3.10: MCNP model for nuclear development facility bunker problem

Methodology

ADVANTG was used for employing the CADIS method to increase the MC efficiency in calculating the neutron dose rate outside the bunker. A 27 neutron multi-group ENDF-VII library was used for the ADVANTG/Denovo calculations. A point adjoint source was defined at the point of the dose rate calculation. The adjoint source strength was defined as the flux to dose rate conversion factors in the 27 energy group structure of the multi-group ENDF-VII calculation.

Similarly to the last example, the CADIS calculation was repeated with different deterministic and WW meshes. An initial deterministic mesh was carefully tailored to capture all the geometric detail in the model. The mesh had having 49 planes in *X* direction, 58 planes in *Y* direction, and 23 planes in *Z* direction. Analogously to the "Full refinement" cases of the last example, the deterministic mesh was refined 5 times by inserting certain number of extra planes

between each two adjacent planes in each of the *X*, *Y*, and *Z* directions. For each of these 5 different deterministic calculations, the WW mesh used the same mesh as the deterministic calculation. For the "WW refinement" cases, the WW mesh was separately refined 8 times using the same planes insertion procedure. The "WW refinement" cases used the fluxes of the same initial deterministic calculation and the WW values of all the new refined cells were similar to the corresponding coarse cells in the initial coarse mesh WW map.

Results

For a neutron source with total strength of 10^{10} neutron/sec, the neutron dose rate was between 238 and 241 microSv/hr and *R* was between 0.9% to 1.1% for all the CADIS cases. The neutron dose rate was 272±20.7 microSv/hr for the analog MC case.

When the WW mesh was refined by inserting 8 planes in each direction, the MCNP calculation stopped because of not being able to allocate enough memory for the WWs on a computing node that had 4 GB of RAM. The storage size of the WW file, in its ASCII format was 11.9 GB for this case which included 903.69 million space-energy cells. The amount of computer memory (RAM) required by such a WW file is half the storage space of the ASCII WW file. The restrictions on the WW map size will be stricter with parallel processing because of increasing the message passing and/or increasing the total amount of memory required to perform the MC calculation in parallel.

Figure 3.11 shows the FOM versus the total number of energy-space mesh elements in the WW file of the MC calculation with changing and without changing the CADIS adjoint deterministic calculation.

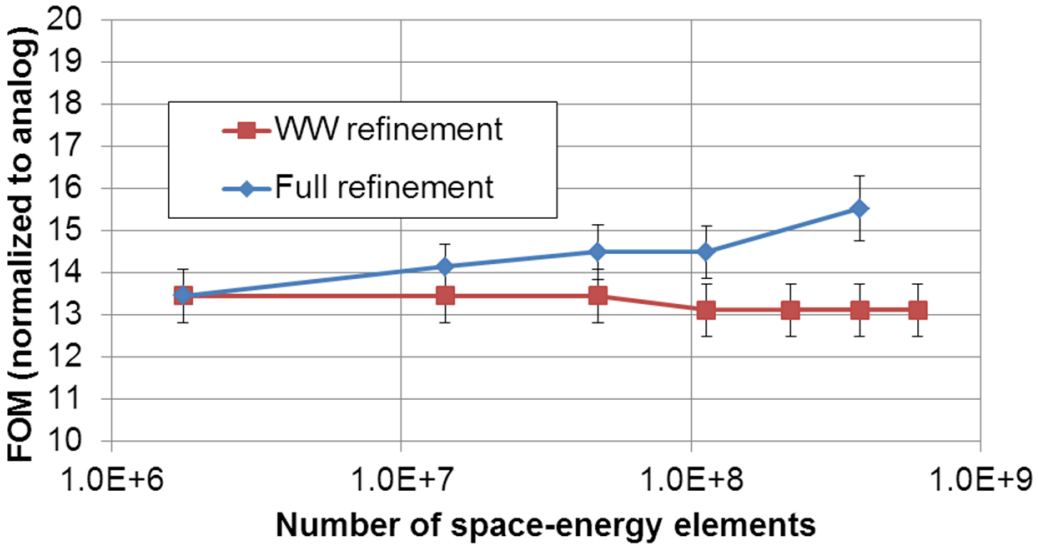

Figure 3.11: FOM variation with WW mesh for nuclear development facility bunker problem

The FOMs of the "Full refinement" cases increased by 15.7% because of refining the deterministic and the WW meshes. This contradicts with the high decrease in the FOM for the "Full refinement" cases in the last example and shows that the variation in the FOM with the WW values is problem dependent. As noted in the last example, the effects of the WW values on the MC FOM can be attributed to the fact that the importance function does not contain any information about the variance introduced by the MC particles.

For the "WW refinement cases", the FOM changed by only 2.6% which is less than half of the 1σ estimated for the uncertainties of each one of the FOMs. This again shows that the computational cost of increasing the number of space-energy elements in the WW mesh without changing the WW values is too small to have an impact on the MC FOM.

3.4 Conclusion

In CADIS and FW-CADIS simulations, the efficiency of the MC calculations depends on the accuracy of the S_N fluxes. In addition to the truncation errors, the coarse meshes used in CADIS and FW-CADIS deterministic calculations also cause geometry discretization errors, which can cause inconsistencies between the deterministic and the MC models. Inaccuracy of the deterministic calculations can seriously decrease the efficiency of the MC calculations. Even worse, severe inconsistencies between the deterministic and the MC models can also cause the MC calculations of CADIS and FW-CADIS simulations to be inaccurate and unreliable.

Refining the mesh always decreases both the truncation and the geometry discretization errors, but the deterministic mesh resolution is limited by the availability of the computing resources. Additionally, the storage size of the VR parameters has to be smaller than the computer memory allocated for the MC calculation. Large WW maps can also obstruct the parallel processing of the MC calculations because of increasing the message passing and/or the total memory requirement. This provides a more restrictive limitation to the fineness of the deterministic mesh because the WWs created by CADIS and FW-CADIS simulations typically use the same mesh and energy group structure of the deterministic calculations.

The effect of the WW mesh resolution on the MC FOM was studied in two different problems. The MC calculation cost of CADIS and FW-CADIS simulations depends on factors other than the accuracy of the VR parameters because the importance function contains only information about the expected score of the Monte Carlo particles and does not contain information about the variance introduced by these particles [73]. Without changing the WW

values, the additional calculation cost of increasing the size of the WW maps is relatively small and does not affect the MC FOM.

The goal of this thesis is to enhance the reliability and the overall efficiency of the CADIS and FW-CADIS simulations by developing automatic algorithms to facilitate capturing more geometrical and physical details in the deterministic calculations without large penalties in the overall efficiency of these hybrid techniques. These algorithms will be discussed in the next three chapters.

Chapter 4: Macromaterial approach

4.1 Motivation

In Sect. 3.3 it was noted that for CADIS and FW-CADIS simulations of geometrically complex problems, the mesh is generally coarser than the mesh needed to solve the problem deterministically and the automation of the deterministic input file creation is necessary. The traditional process of defining the materials for CADIS and FW-CADIS deterministic calculations used the cell center (CC) approach. The CC approach assigns a material for each mesh cell in the deterministic model based on the material existing at the center point of this cell in the MC model. Despite its simplicity, it is difficult to capture the important geometric detail and avoid the inconsistencies between the MC and deterministic models using the CC approach.

The MM approach was developed to enhance the geometry representation without increasing the resolution of CADIS and FW-CADIS deterministic meshes. It automatically creates a mixture for each mesh cell in the deterministic model by homogenizing the materials that coincide with the cell in the MC model [86].

For CADIS and FW-CADIS, the user has to define the adjoint source representing the tally response function (e.g. cross-sections). If the tally response function is space-dependent, describing it manually can be very difficult. Since the MM approach provides access to the materials fractions of each mesh cell in the deterministic model, it was also used in defining the adjoint sources for space-dependent response functions in CADIS and FW-CADIS simulations [87].

4.2 Algorithm

The steps of the MM approach can be summarized as follows:

1. Construct a sub-grid over each of the user-supplied mesh cells. The number of subdivisions, p, in each dimension is supplied by the user and hence the total number of sub-voxels is p^3.
2. Determine the material associated with each sub-voxel using the CC approach.
3. Calculate approximate volume fractions associated with each material to calculate a homogenized material mixture for each mesh cell.
4. Loop through the newly created materials and set materials with similar compositions, within a preset threshold, to be equivalent.

Since the materials are queried p^3 times in each mesh cell, the error in approximating the volume fraction of materials, and thus the mass discrepancy, decreases as $O((1/p)^3)$. The drawback of the MM approach is the potential creation of a large number of material mixtures. The reduction of the number of materials in step 4 can be used to decrease the memory requirements for storing the macroscopic cross-sections of the deterministic calculations; otherwise, the number of materials scales with the number of mesh elements in the original grid.

The MM approach was also used to automatically define the adjoint sources for space-dependent responses in CADIS and FW-CADIS simulations. In both MAVRIC and ADVANTG, the user defines the adjoint sources as regions in space (points or bounding boxes) and energy spectra. For CADIS simulations, the user-defined regions are mapped on the S_N grid and the adjoint sources are uniformly distributed on the mesh elements coinciding with these

regions. In FW-CADIS simulations, the energy- and space-dependent adjoint sources, which are set to represent the response functions ($q^+(\bar{r},E) = \sigma_d(\bar{r},E)$) can be expressed as,

$$q^+(\bar{r},E) = \sigma_d(E)g(\bar{r}), \tag{4.1}$$

where $g(\bar{r})$ is either 0 or 1 for each S_N mesh cell (uniformly distributed). Unfortunately this description is not suitable for adjoint sources representing cross-sections of some nuclear reactions such as atomic displacement, nuclear heating, or helium production. For example, if one wants to calculate the atomic displacements in steel and the S_N mesh cells of the adjoint source have different fractions of steel mixed with other materials, $g(\bar{r})$ should have multiple values between 0 and 1 depending on the fraction of steel in each mesh cell. For additive responses such as nuclear heating, the energy-dependent macroscopic cross-section will vary with the materials composition in each mesh cell. In these cases, the space and energy dependency of the adjoint sources are not separable ($q^+(\bar{r},E) = \sigma_d(\bar{r},E) \neq \sigma_d(E)g(\bar{r})$) because the energy distribution of the response will vary from one cell to another.

For defining the energy-dependent adjoint source strength in each mesh cell of CADIS or FW-CADIS deterministic grids, the response function of each material is weighted by its MM fraction before summing the response functions to represent the adjoint source of the cell. In a discretized form, the space- and energy- dependent adjoint source, $q^+_{ijk,g}$ can be expressed by,

$$q^+_{ijk,g} = \sum_{m=1}^{m=M} f^m_{ijk}\sigma^m_g, \tag{4.2}$$

where M is the total number of materials in the MC model, f^m_{ijk} is the MM fraction of the m^{th} material in the mesh cell defined by the three indices i, j, and k, σ^m_g is the value of the group-wise response function (e.g tally-cross section) for group g and material m. In FW-CADIS

calculations, the adjoint source strength of cell ijk gets weighted by the inverse of the total response calculated from a forward deterministic calculation according to Eq. (3.3). If the response is only required for a certain material, weighting the adjoint source strength balances the strength of the adjoint source in each cell according to the MM fraction of this material in the cell. Weighting the adjoint source strength by the MM fraction of each material in each cell before summing these strengths for each energy group provides the desired energy- and space- dependent (inseparable) response for additive responses.

4.3 Implementations

The MM approach was implemented for the materials definition and the adjoint source description of the SCALE [45] shielding analysis sequence, MAVRIC [33] and was released with SCALE6.1 [88]. It was also implemented for the materials definition in ADVANTG [64]. In the MMGridGen tool [89] of the University of Wisconsin-Madison (UW-Madison) Direct Accelerated Geometry Monte Carlo (DAGMCNP) package [79], the MM approach was implemented in two flavors. The first flavor, denoted as point-sampling in Ref. 89, is similar to the SCALE and ADVANTG implementation. The second flavor, ray-tracing uses the MC ray-tracing capabilites for calculating the materials volume fractions [89].

4.4 Demonstration

4.4.1 Deterministic accuracy

Problem description

To demonstrate the effects of the MM approach on the accuracy of the S_N calculations, a spent fuel shipping cask was modeled in Denovo [11]. The cask had a cylindrical shape with a total diameter of 3.4 m and total height of 5.72 m. It is composed of three materials: homogenized fuel elements materials, concrete, and steel. Figure 4.1 represents the SCALE General Geometry Package (SGGP) model of the shipping cask.

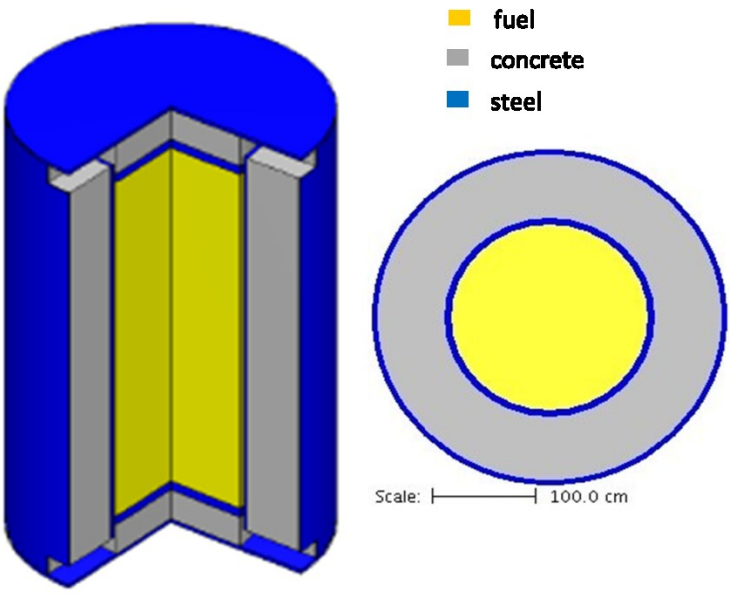

Figure 4.1: Spent fuel shipping cask

Methodology

The Denovo input file was created by MAVRIC. Denovo was used to calculate the neutron dose rate 1 m away from the shipping cask at its mid plane. A uniform homogenous source neutron source with a spent fuel energy spectrum was modeled in the fuel region. A 27 neutron/19 gamma multi-group ENDF-VII library was used in this analysis.

Two mesh grids were used for the Denovo calculations. The coarse grid contained 70,000 cells with variable cells dimensions. The fine grid, containing 560,000 mesh cells, was created by inserting extra planes at the midpoints of each two adjacent *X*, *Y*, and *Z* planes in the coarse grid. The MM approach was only used with the coarse grid. Figure 4.2 shows the Denovo models that used the coarse grid with and without the MM approach and the fine grid.

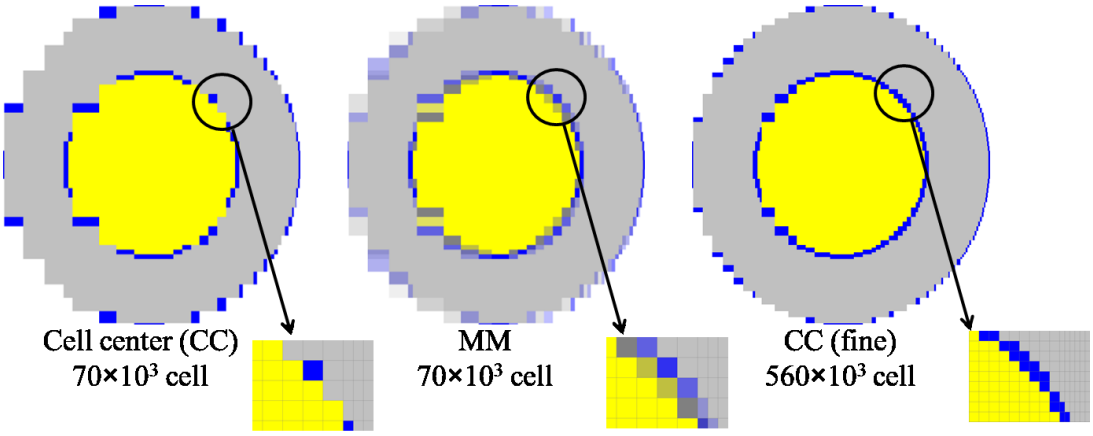

Figure 4.2: Denovo models of shipping cask problem

As shown in Fig. 4.2, the MM approach is especially useful in defining the materials at the cells where the mesh overlaps material boundaries.

Results

Table 4.1 shows the results of the three Denovo calculations.

Table 4.1: Shipping cask Denovo results

Calculation	Time (min)	Dose Rate (μSv/hr)
CC (coarse)	7.6	7.2
MM (coarse)	8.3	5.9
CC (fine)	62.5	3.6

The calculated neutron dose rate should be more accurate with the fine mesh case because refining the mesh decreases the truncation errors, improves the materials representation, and improves the source representation. Unfortunately, refining the mesh increases the Denovo the computational time and memory requirements run. The fine grid Denovo calculation took nearly eight times more time and memory, but the results were definitely more accurate.

The MM case only required 9.2% more time than the CC case that used the same grid. Using the dose rate calculated from the fine case as the reference value, the error of the MM case was 36.1% smaller than the error of the CC case. This shows that improvement in the materials representation provided by the use of the MM approach enhances the accuracy of the deterministic calculations.

4.4.2 Monte Carlo efficiency

Problem description

The implementation of the MM approach in the SCALE shielding analysis sequence, MAVRIC was tested using a source-detector problem. The problem represented a 1.22 m thick concrete wall with 5.72 cm diameter steel rebar on 30.48 cm centers in each dimension and 1.27 cm thick steel plates on each side. The objective was to calculate the dose 1 m from the wall from a 1 Ci source of spent fuel photons 1 m on the other side of the wall. Figure 4.3 shows the shield in real life and a schematic view for the MAVRIC model.

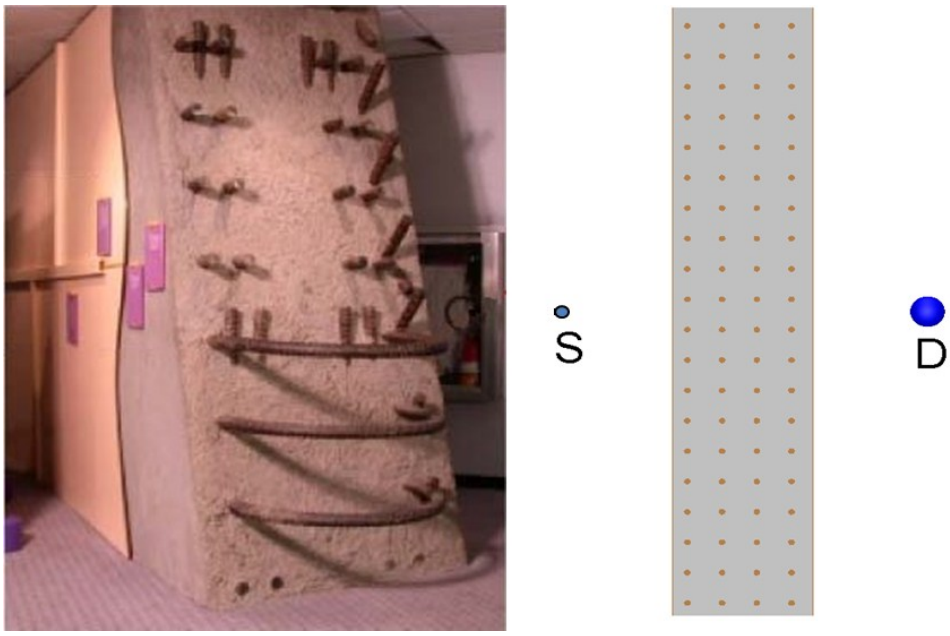

Figure 4.3: Concrete/rebar problem

Methodology

The S_N mesh was fixed at 4×10^5 elements. With a uniformly spaced grid and the CC approach, the steel rebar was completely missed in the S_N model. The MM capability was used with different numbers of cells subdivisions, p=2,3,4,5. For comparison, a non-uniform mesh with the same number of elements was also used. The positions of the planes in the non-uniform mesh were carefully chosen to preserve as much rebar mass as possible. Figure 4.4 shows the S_N models used for all the cases.

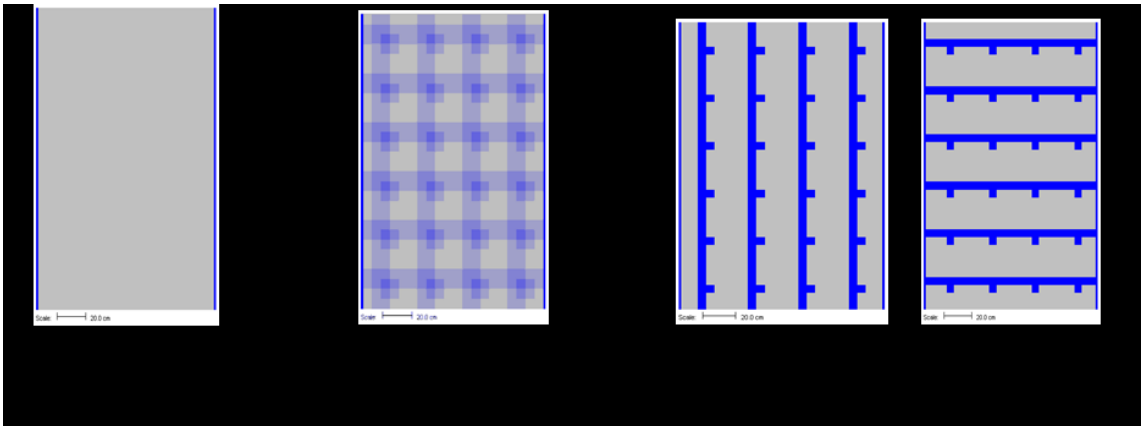

Figure 4.4: Denovo models for concrete/rebar problem

Results

Table 2.1 shows the running time for both Denovo and Monaco calculations, the Monaco calculated dose rates and their *R*s, the MC FOM, and the statistical uncertainty in the MC FOM for each case. The single-tally MC FOM of Eq. (2.23) was used for this source-detector problem. The statistical uncertainty in the FOM was calculated using the VOV information using Eq. (2.26).

Table 4.2: Concrete/rebar CADIS results

	Denovo time (min)	Dose rate per curie (10^{-5} μSv/hr)/Ci	*R*	Monaco time (min)	Normalized FOM
CC	18.01	2.5	0.3%	185.24	1.00 ±0.8%
MM: 2^3	18.22	2.5	0.2%	185.18	2.08 ±0.6%
MM: 3^3	18.72	2.5	0.2%	183.99	1.77 ±0.6%
MM: 4^3	17.65	2.5	0.2%	187.97	2.00 ±0.6%
MM: 5^3	18.34	2.5	0.2%	181.16	1.94 ±0.6%
Nonuniform grid	17.12	2.5	0.2%	188.03	1.67 ±0.6%

The dose rate calculated in all the Monaco simulations was 2.5×10^{-5} μSv/hr with $R<0.5\%$. *The FOM with the MM approach is about a factor of 2 higher than the one with the CC approach for the same S_N grid and the increase in the Denovo runtime is insignificant.* Increasing the number of MM test points within each voxel in the S_N grid did not significantly improve the performance of the Monaco simulation probably because the geometry did not have enough heterogeneity to make a difference. The FOM of the MM cases and the non-uniform grid case were in the same order with the FOM of the non-uniform grid being about 30% less than the MM cases. While it was possible to manually create a good mesh that captures most of the MC geometric detail for this relatively simple problem, the process becomes extremely difficult for large and geometrically complex problems.

4.4.3 Automating adjoint source definition

Problem description

To test the use of the MM approach in defining the adjoint sources in MAVRIC, the simple model shown in Fig. 4.5 was created [87].

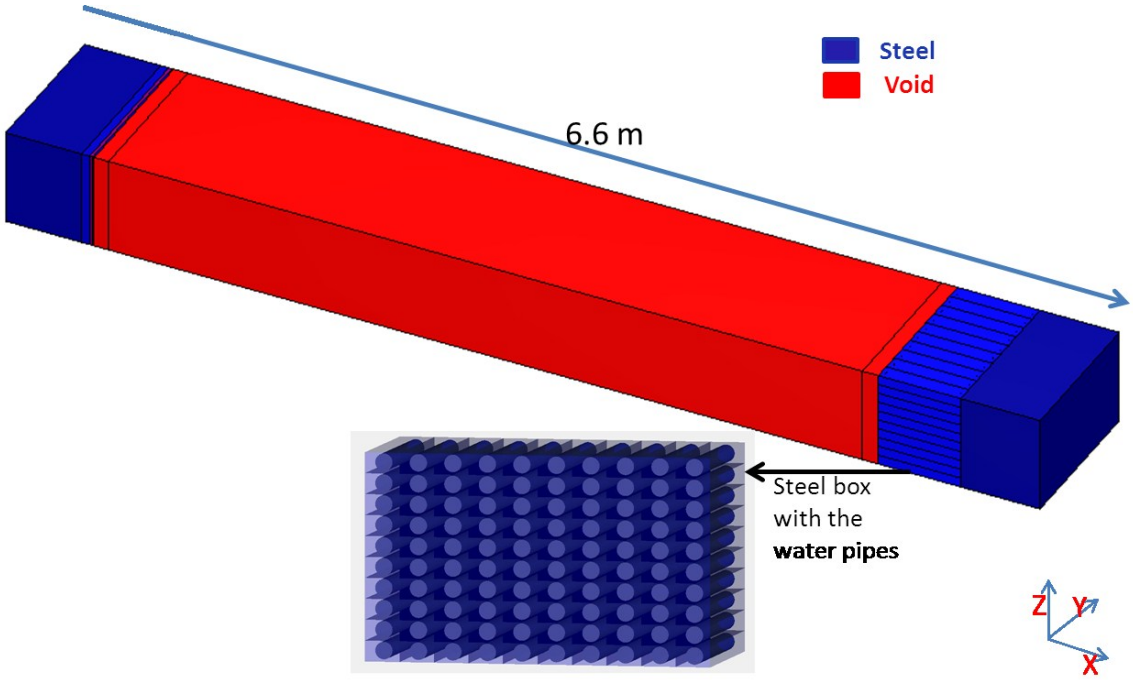

Figure 4.5: Steel box with water pipes problem

Water pipes penetrated a 48 cm×100 cm×60 cm steel box in the *X* direction. The pipes had uniform diameters of 5 cm. A monoenergetic neutron source was distributed uniformly in 475 cm×100 cm×60 cm vacuum box. The energy of the neutron source was uniform in the first group (6.38-20 Mev) of the 27 neutron/19 gamma ENDF-VII library which was used in this analysis. The model was placed in a lattice of 9 similar models to account for neutrons/photons reflections from the other components in the system.

The goal of the analysis was to determine the nuclear heating due to the neutrons and the secondary photons in the steel box. A high resolution mesh tally with uniform size voxels (1 cm in *X*, 0.5 cm in *Y*, and 0.5 cm in *Z*) was superimposed over one of the center water pipes.

Methodology

The S_N mesh sizes were 5 cm in *X*, 5 cm in *Y*, and 3 cm in *Z* over the steel box. With this grid, all the mesh elements contained steel but only some of them contained water.

The adjoint source was defined as a rectangular parallelpiped twice as big as the mesh tally in *Y* and *Z* directions and with the same length in the *X* direction.

The analysis intended to show the effects of different adjoint sources on the efficiency of the MC calculation. For the FW-CADIS calculations, eight different adjoint sources were defined before they were automatically weighted by the inverse of the response calculated from a forward solution (Eq. (3.3)):

A. Total flux: uniform energy spectrum and total flux for weighting
B. Group fluxes: uniform spectrum and flux weighting
C. Water everywhere: water heating cross section for spectrum, response weighting, and no MM
D. Water : water heating cross section for spectrum, response weighting, and MM
E. Steel everywhere: steel heating cross section for spectrum, response weighting, and no MM
F. Steel: steel heating cross section for spectrum, response weighting, and MM
G. Steel and water (no weighting): unweighted sum of steel and water heating cross sections for spectrum and response weighting
H. Steel and water (weighted by MM): MM weighted sum of steel and water heating cross sections for spectrum and response weighting

When MAVRIC uses flux weighting instead of response weighting, the FW-CADIS adjoint source gets weighted by the energy-dependent flux instead of the total response. For case B, the response weighing of Eq. (3.3) was substituted by,

$$q^{+}(\bar{r},E)=\frac{\sigma_d(\bar{r},E)}{\phi(\bar{r},E)}. \tag{4.3}$$

Flux weighting is usually used when the MC tally represents energy-dependent responses. For case A, the sum of the fluxes was used for the response weighting instead of the total nuclear heating.

Since some of the mesh elements within the adjoint region did not have water, the adjoint source of case D only existed in some of the mesh cells. All the elements had steel but with different fractions. The MM approach was used to weight the adjoint source strengths with the MM fraction of each mesh cell in cases D, F, and H. Figure 4.6 (A to H) shows the different adjoint sources used in this analysis.

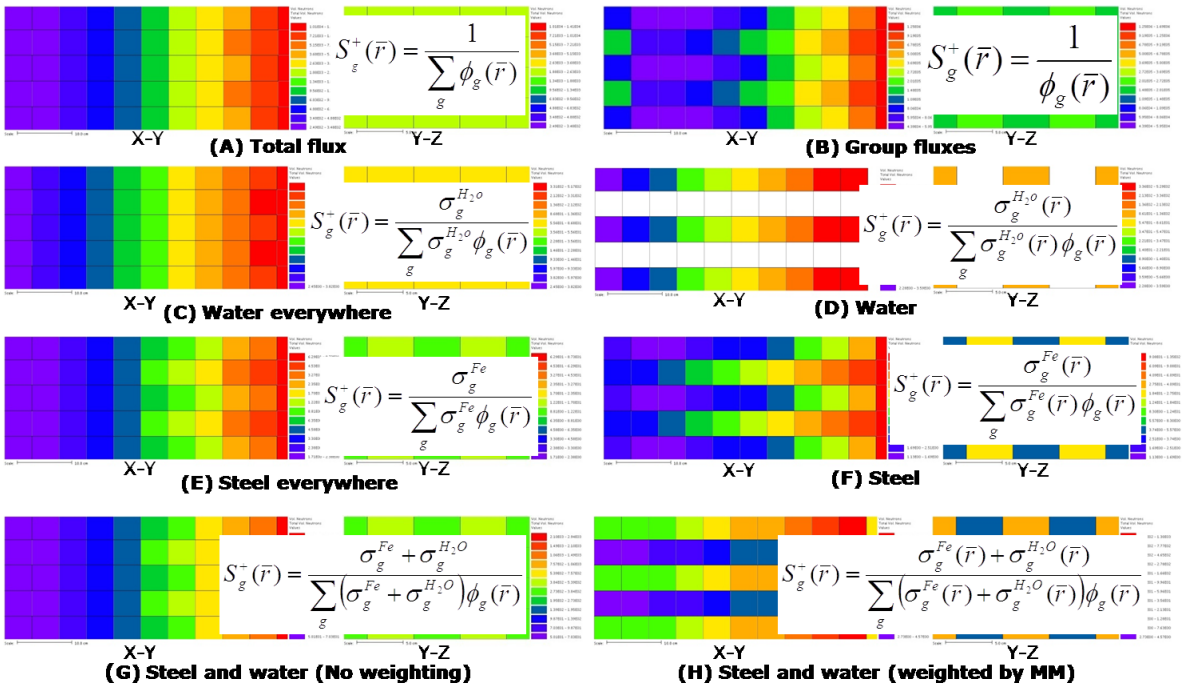

Figure 4.6: Adjoint sources of steel box with water pipes problem

Results

For all the FW-CADIS cases with the different adjoint sources, the differences in MC results were within the uncertainties which were less than 7% everywhere. Figure 4.7 shows the total (neutrons+ gamma) nuclear heating in the mesh tally.

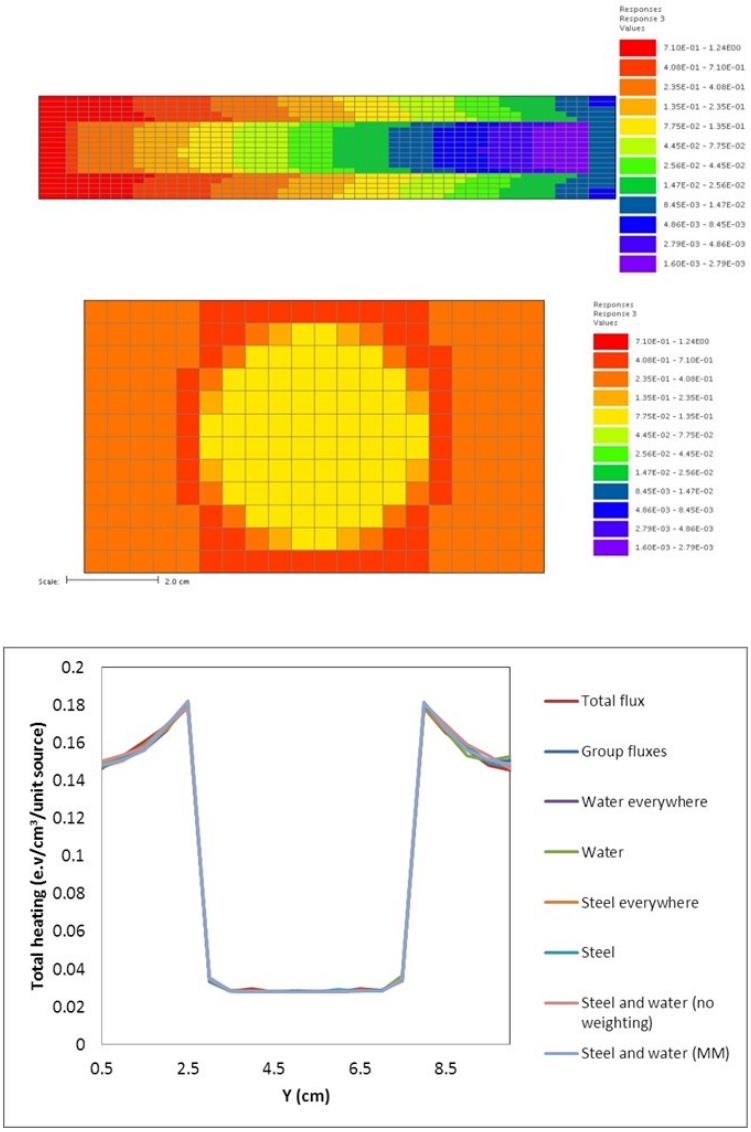

Figure 4.7: Total heating in steel box with water pipes problem

Figure 4.8 shows the CDF of the *R*s in the mesh tally voxels for the different FW-CADIS cases and Table 4.3 shows the fraction of voxels with $R<3\%$.

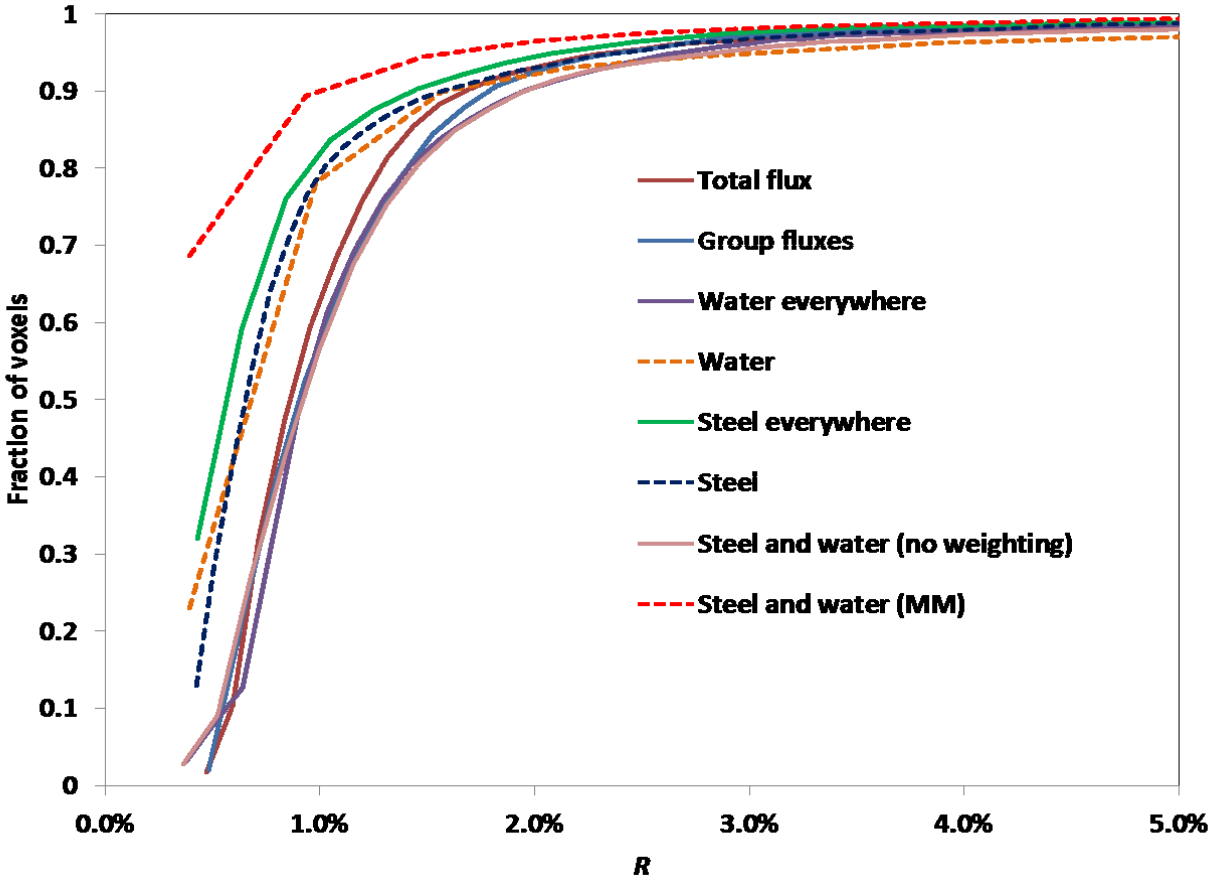

Figure 4.8: CDFs for steel box with water pipes problem

Table 4.3: Fractions of voxels with $R < 3\%$ for steel box with water pipes problem

Case	Fraction of voxels
A	96.7%
B	97.0%
C	96.2%
D	94.8%
E	97.6%
F	96.8%
G	95.4%
H	98.0%

Case H had the largest fraction of voxels with lower *R*s. For this case, the adjoint source was defined as the sum of both the steel and the water heatings weighted by the MM fractions of steel and water in each mesh cell. This shows that using the MM approach in defining the adjoint source increased the efficiency of the MC simulation. The second best case was case E. For this case, the adjoint source strength was uniform in all the mesh cells and the adjoint source spectrum was defined to be the steel heating cross section. The good MC efficiency of case E is due to the domination of steel heating and the similarity in the overall shape of steel and water heating cross section. Case F with steel heating as the adjoint source came third in terms of the MC running efficiency for 90% of the voxels, yet it did not perform as well for the remainder 10%. In this case, all the cells had adjoint sources but the cells with both steel and water had less adjoint source strengths since in this case the adjoint source strengths were weighted by the amount of steel in each cell ignoring the water heating. Case D with water heating as the adjoint source was one of the cases with the least MC efficiency. For this case, the adjoint source was restricted to the cells with water and the overall volume of the adjoint source was smaller than the volume covered by the mesh tally. The two cases with the least MC running efficiency were the cases with the group fluxes and the total flux as the adjoint source spectrum. This was because the adjoint source spectra of these cases were unrelated to the required heating response in steel and water.

4.5 Conclusion

Compared to the traditional CC approach, the MM approach provides a better technique for automating the process of deterministic input file creation in CADIS and FW-CADIS simulations.

By enhancing the materials representation and reducing the geometry discretization errors, the MM approach increases the accuracy of the deterministic calculations with only a negligible computational time penalty.

Because of the enhancement in the accuracy of the deterministic calculation, the expected improvement in the MC FOM has been demonstrated for CADIS and FW-CADIS simulations. The MM approach was also used to automate the adjoint source description of space-dependent response functions in CADIS and FW-CADIS simulations.

The MM approach was implemented for the materials definitions and adjoint source description in SCALE6.1. It was also implemented in ADVANTG and DAGMCNP.

Chapter 5: Deterministic mesh refinement

5.1 Motivation

As shown in Sect. 3.3, the efficiency and reliability of CADIS and FW-CADIS simulations depend on the accuracy of the deterministic solutions. To reduce both truncation and geometry discretization errors, the mesh used in the deterministic calculations has to be as fine as possible. Unfortunately, the computing resources available for the deterministic calculations of CADIS and FW-CADIS simulations are usually not enough to resolve the phase-space domain of large and geometrically complex problems and capture all the geometric details of the MC models.

In all current CADIS and FW-CADIS implementations, the deterministic mesh has to be manually created. Even though the materials specification of the deterministic calculations is automatic, developing an efficient mesh for the deterministic calculation is very difficult for large and complicated problems especially because the elements' sizes have to be in the order of tens of centimeters.

The deterministic mesh refinement algorithm was developed to automatically create better deterministic models by capturing as much geometric detail as possible from the MC models without increasing the total number of mesh cells that is usually determined by the availability of computing resources.

5.2 Algorithm

The goal of the deterministic mesh refinement algorithm is to minimize the geometry discretization errors in CADIS and FW-CADIS deterministic calculations.

Since the objective is to generate the deterministic mesh for the CADIS and FW-CADIS simulations of large and complicated problems, the savings in both human and computer times are crucial to determining the effectiveness of the algorithm. In this thesis, the deterministic mesh refinement algorithm will only be limited to the automatic process of the deterministic input file creation. To avoid the iterative repetition of the deterministic calculations, the algorithm implementation will not use fluxes' information. This excludes addressing some important mesh-related issues such as the refinement of the particles' flow channels between the source and the detector, but the algorithm will be much faster and easier to implement. Moreover, algorithms based on cross-sections information will not be considered in this thesis. The extra computations required by the recalculation of the macroscopic cross-sections might not be very expensive, but this thesis will only focus on algorithms based on geometric information because of their relative simplicity.

A mesh potential function has to be devised to determine the regions at which the mesh needs to be refined. For the deterministic mesh to be representative of the MC geometry, the mesh potential function has to be associated with relevant quantities such as materials masses. The MM approach can be used to identify the heterogeneity of each mesh cell. During the MM calculations, the constituents of each mesh cell are internally stored in a vector of volume fractions. Each element in the vector represents the volume fraction of one of the materials used in the MC model not including vacuum. The void fraction can be calculated by subtracting the

sum of the fractions from 1.0. The mesh cells are expected to have a wider distribution of MM fractions with more heterogeneity and a sharper peaked distribution with less heterogeneity. Therefore, the disparity of the MM fractions can be used to formulate a heterogeneity parameter for each mesh cell. Additionally, the volume has to be included in calculating the heterogeneity parameter of each mesh cell. If two cells have the same disparity of MM fractions but different volumes, a more accurate material definition of the larger cell will have a higher impact on enhancing the deterministic model than the smaller cell. The heterogeneity parameter used in developing the mesh potential function of the deterministic mesh refinement algorithm can be expressed as,

$$h_{ijk} = \left(\sigma_{max} - \sigma_{ijk}\right)V_{ijk}, \tag{5.1}$$

where h_{ijk} is the heterogeneity parameter of the mesh cell defined by the three indices $i, j,$ and k, σ_{ijk} is the standard deviation of the fractions in the vector consisting of the materials' fractions and the void fraction of the mesh cell, σ_{max} is the maximum possible standard deviation of this vector, and V_{ijk} is the volume of the cell. Table 5.1 shows an example for calculating the standard deviation of the volume fractions vector for a MC model with 3 materials.

Table 5.1: Heterogeneity parameter calculation

Materials\Cells	Cell 1	Cell 2	Cell 3	Cell 4
Vacuum	0.25	0.33	0.50	1.00
Mat 1	0.25	0.33	0.50	0.00
Mat 2	0.25	0.33	0.00	0.00
Mat 3	0.25	0.00	0.00	0.00
Standard deviations				
σ	0.00	0.17	0.29	0.50
$\sigma_{max}-\sigma$	0.50	0.33	0.21	0.00

The value of the maximum standard deviation of the materials vector depends on the number of materials in the MC model. It corresponds to cells with only one material and no heterogeneities. Theoretically the standard deviation can be zero for cells with equal fractions of materials including vacuum. These cells have the maximum disparity of materials and should have high heterogeneity parameter. Because of subtracting the standard deviation from the maximum standard deviation, mesh cells with equal volumes will have maximum heterogeneity parameter if they have uniform materials fractions and minimum heterogeneity parameter if they are composed of only one material.

A lot of the existing, widely available S_N codes only have the capability of performing the calculations on orthogonal, simply connected mesh for which each cell face adjoins one and only one neighbor. Performing transport calculations on a simply connected mesh considerably simplifies the sweeping algorithm [90]. Currently, Denovo is limited to simply connected Cartesian mesh [11]. Since Denovo is the preferred deterministic code for ADVANTG, the implementation of the mesh refinement algorithm in ADVANTG was constrained by preserving

the connectivity of the orthogonal Cartesian mesh. A block-heterogeneity parameter can defined for each *X*, *Y*, or *Z* block as the sum of the heterogeneity parameters of all the cells that belong to each block,

$$H_i = \sum_{j,k} h_{ijk}, \qquad H_j = \sum_{i,k} h_{ijk}, \qquad H_k = \sum_{i,j} h_{ijk}. \tag{5.2}$$

Starting from a user defined "initial guess" for the deterministic mesh, the steps of the deterministic mesh refinement algorithms can be summarized as follows:

1. Calculate the heterogeneity parameter of each mesh element using Eq. (5.1)
2. Calculate the block heterogeneity parameter of each *X*, *Y*, and *Z* block using Eqns. (5.2).
3. Modify the mesh by inserting an extra plane at the midpoint between the two bounding planes of the *X*, *Y*, or *Z* block with the maximum heterogeneity parameter.
4. Recalculate the heterogeneity parameter for each of the new elements added by the extra plane insertion.
5. Recalculate all the block heterogeneity parameters.
6. Repeat step 3, 4, and 5 until a user specified total number of mesh elements is reached or until the sum of the heterogeneity parameters of all the mesh elements become zero.

It is necessary to calculate the MM fractions of all the mesh elements for calculating the heterogeneity parameters in step 1. It is not necessary to recalculate the MM fractions of the newly inserted mesh elements after each refinement step (step 3). If the MM fractions are not updated after each refinement step, the heterogeneity parameters, which will be based on the initially calculated MM fractions, will still be updated because of changing the elements' volumes. The later refinement procedure can be useful with fine initial meshes because of the savings in the computational time required to develop the deterministic models.

For Cartesian meshes, the sum of the heterogeneity parameters of all the mesh elements can only be zero for underlying geometries with only rectangular cross sectional areas. The user specified total number of mesh elements should be determined by the computing resources availability for the deterministic calculation or the computer memory that can be allocated for the WW maps of the MC calculations. The maximum number of mesh elements can be specified using a mesh refinement parameter representing the ratio between the total number of elements in the final mesh and the total number of mesh elements in the initial mesh. The deterministic models shown in Fig. 5.1 were developed from two MCNP models of cubic steel boxes having an HEU sphere wrapped inside a polyethylene layer.

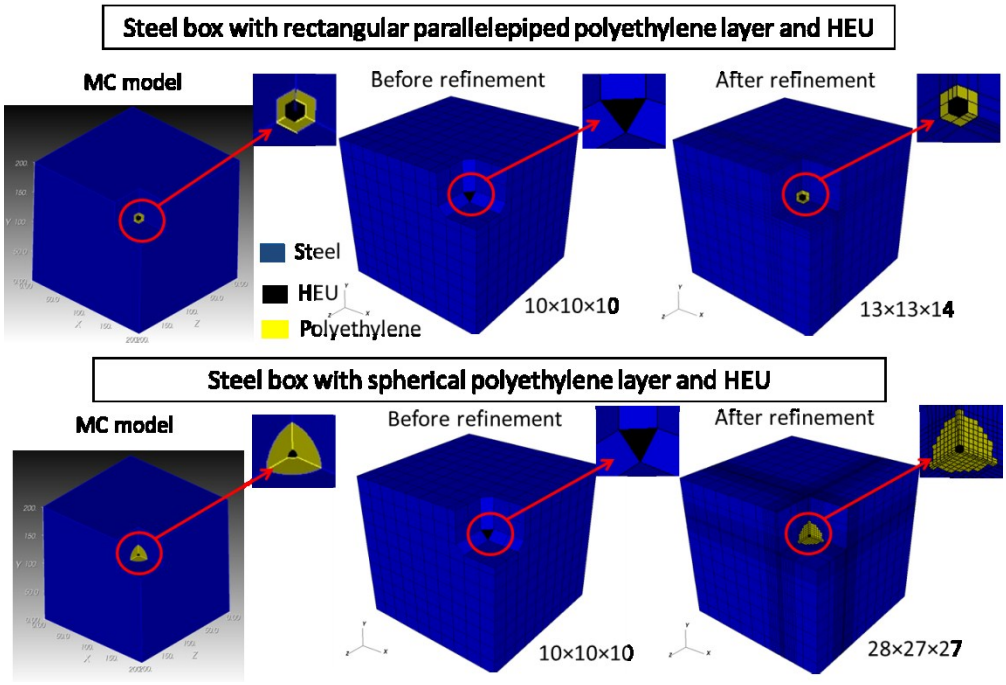

Figure 5.1: Denovo models formed with deterministic mesh refinement algorithm

The polyethylene layer had a cubic geometry in the first model and a spherical geometry in the second. An initial mesh having 10 planes in the *X* direction, 10 planes in the *Y* direction, and 10 planes in the *Z* direction and fixed refinement parameter of 20 was used for both models. For the first model, the refinement stopped after 10 refinement steps because the heterogeneity parameters were all zeros. The final mesh had 13 planes in the *X* direction, 13 planes in the *Y* direction, and 14 planes in the *Z* direction for this model. For the second model, the maximum total number of mesh cells was reached after 52 refinement steps. The final mesh contained 28 planes in the *X* direction, 27 planes in the *Y* direction, and 27 planes in the *Z* direction.

5.3 Demonstration

5.3.1 Mass conservation

Problem description

A cylindrical spent fuel shipping cask similar to the one used in Sect. 4.4.1 was used to calculate the materials volumes in the Denovo models created by the deterministic mesh refinement algorithm. Figure 5.2 shows the spent fuel shipping cask.

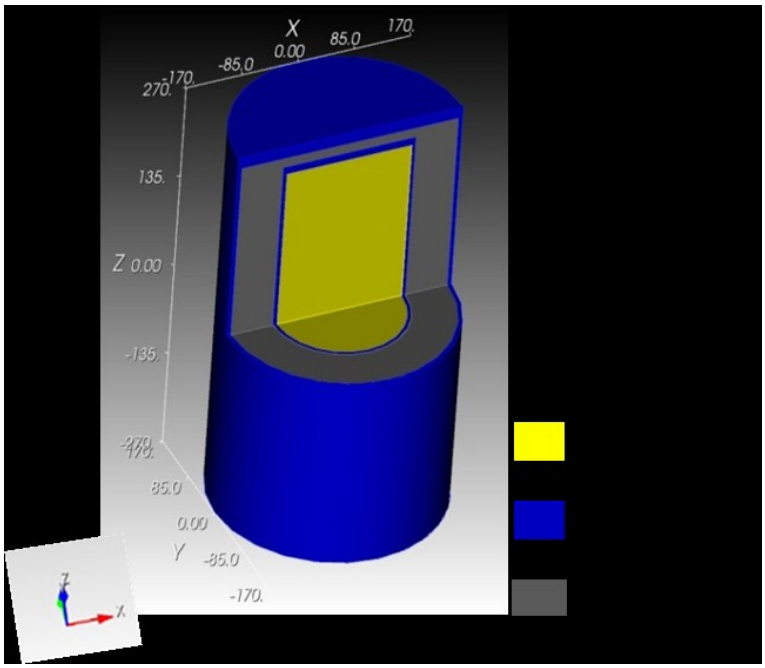

Figure 5.2: Cylindrical spent fuel shipping cask

The cask had a cylindrical shape with a total diameter of 3.4 m and total height of 5.4 m and was composed of three materials: homogenized fuel materials, concrete, and steel. The three different materials were modeled as concentric cylinders to simplify the theoretical calculations of the materials volumes in the MC model.

Methodology

An MCNP model for the cask was used by ADVANTG to create Denovo models developed using different refinement methods. For this analysis, the Denovo models were only used to calculate the materials volumes of the different refinement methods and were not used in performing deterministic calculations. An initial mesh having 4 planes in *X* direction, 4 planes in *Y* direction, and 6 planes in *Z* direction was used. The mesh was refined uniformly by inserting *p* extra planes at equidistant positions between each two adjacent planes in each direction. The

refinement parameter, p was varied between 1 and 20. The deterministic mesh refinement algorithm was then used to refine the initial mesh by a factor of p^3 without recalculating the MM fractions and with the MM fractions recalculations.

The volumes of each of the three different materials (fuel, concrete, and steel) was calculated for each of the 60 cases: 20 cases with uniform refinement, 20 cases with the refinement algorithm and no recalculation of the MM fractions, and 20 cases with the refinement algorithm and MM fractions recalculation. The MM parameter used for materials sampling was set to 15 for all the 40 cases that used the deterministic mesh refinement algorithm. The differences between the volumes of each material (not including vacuum) in the MC model and the corresponding volumes in the Denovo models were calculated for all the 60 Denovo models. The total discrepancy in the materials volumes was calculated using the sum of the absolute values of these differences divided by the total materials volume.

Results

Figure 5.3 shows the total discrepancy in materials volumes between the MCNP model and the Denovo models created using the three different refinement methods: uniform refinement, deterministic mesh refinement algorithm without recalculation of the MM fractions, and deterministic mesh refinement algorithm with MM fractions recalculation. The time taken by ADVANTG to develop these models is also shown in Fig. 5.3 as a function in the total number of mesh cells.

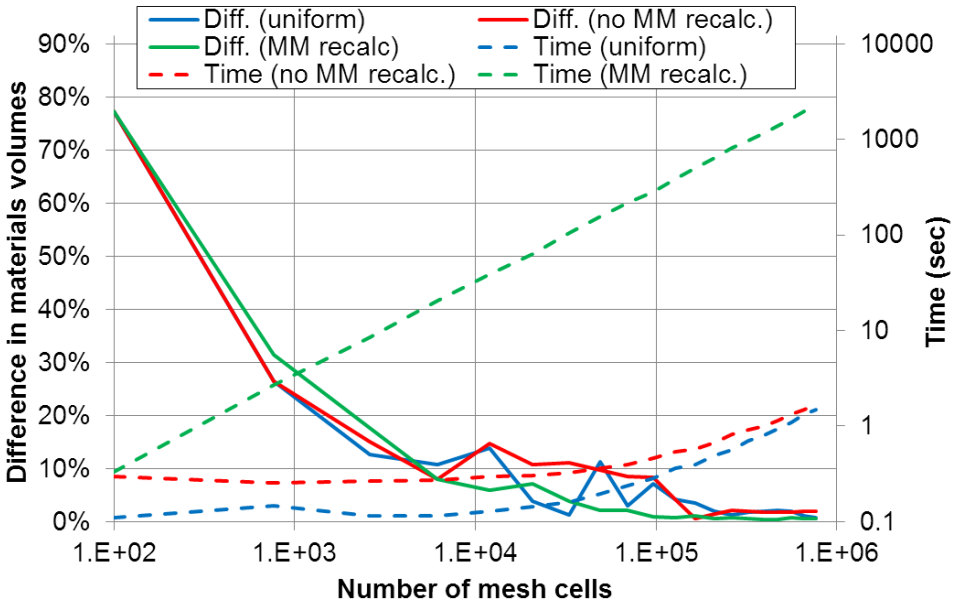

Figure 5.3: Total discrepancy in materials volumes for spent fuel shipping cask problem

The time taken by ADVANTG to create the Denovo models linearly increases with the number of mesh elements for each of the three refinement methods because the number of points sampled for materials definitions increases with the number of mesh cells. The slope of the linear increase is much higher with the MM fractions recalculation because of the extra time required for the MM resampling, but this time is still less than the time needed for the deterministic calculation, which was a factor of 6.5 higher for 0.775 million cell model (last point) and a 27 neutron group library. This shows that, even with the recalculations of the MM fractions, the computational efforts of the deterministic mesh refinement algorithm are usually much less than the overall computational efforts required in CADIS and FW-CADIS simulations.

With the deterministic mesh refinement algorithm with the MM fractions recalculation, the total discrepancy in materials volumes is monotonically less than the discrepancy with the

other two refinement methods. Even when the materials volumes discrepancy of the uniformly refined mesh is smaller than the discrepancy of the models created by deterministic mesh refinement algorithm, the deterministic mesh refinement algorithm provided better deterministic models. Figure 5.4 shows the deterministic models created using the three refinement methods for p=7 and total numbers of mesh elements around 33,000.

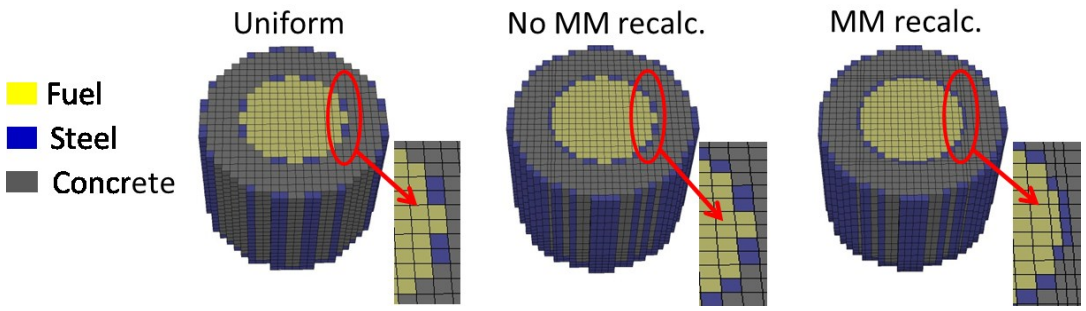

Figure 5.4: Deterministic models with similar number of mesh elements for spent fuel shipping cask problem

It is apparent that the deterministic model created by the automatic mesh refinement algorithm and the MM fractions recalculation has a better representation for the steel surrounding the central fuel region even though the difference between the steel volumes in the MCNP model and in the automatically refined Denovo model is 12.9 times higher than difference in the steel volumes in the MCNP model and in the uniformly refined Denovo model.

5.3.2 Deterministic accuracy

Problem description

The same cylindrical cask of the last example was modeled in Denovo to demonstrate the effects of the deterministic mesh refinement algorithm on the accuracy of the S_N calculations. A uniform homogenous neutron source with a spent fuel energy spectrum was modeled in the fuel region. For this example, the goal is to calculate the neutron dose rate at a specific location 187.5 cm from the central axis of the cask as shown in Fig. 5.5.

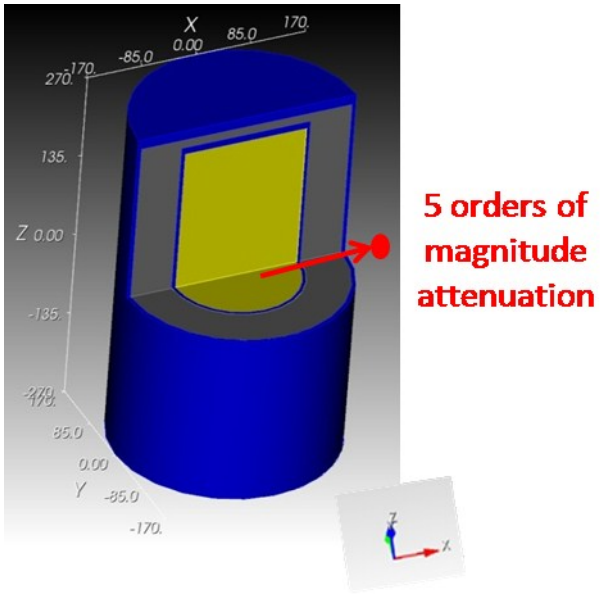

Figure 5.5: Position of neutron dose rate calculation for spent fuel shipping cask problem

Methodology

The Denovo input files were developed by ADVANTG using an MCNP model of the cask. The same initial mesh used in the last example was refined uniformly with eight different refinement parameters. The deterministic mesh refinement algorithm was then used to develop eight different meshes. For the meshes developed using the deterministic mesh refinement algorithm to have similar number of mesh elements as the meshes created by uniform refinement, the total number of cells in the meshes created by the deterministic mesh refinement algorithm were equal to the number of cells in the initial mesh multiplied by the uniform refinement parameter raised to the cubic power.

The MAVRIC hybrid sequence was used for comparison. This later calculation did not suffer from geometry discretization errors because the final Monaco calculation used the exact MC model of the cask.

A 27 neutron groups ENDF-VII library was used for the Denovo and the MAVRIC/Monaco calculations.

Results

Figure 5.6 shows the neutron dose calculated by Denovo for uniformly refined meshes and meshes developed by the deterministic mesh refinement algorithm as a function of the total number of mesh cells. The neutron dose calculated by MAVRIC/Monaco is shown as a dotted line in Fig. 5.6.

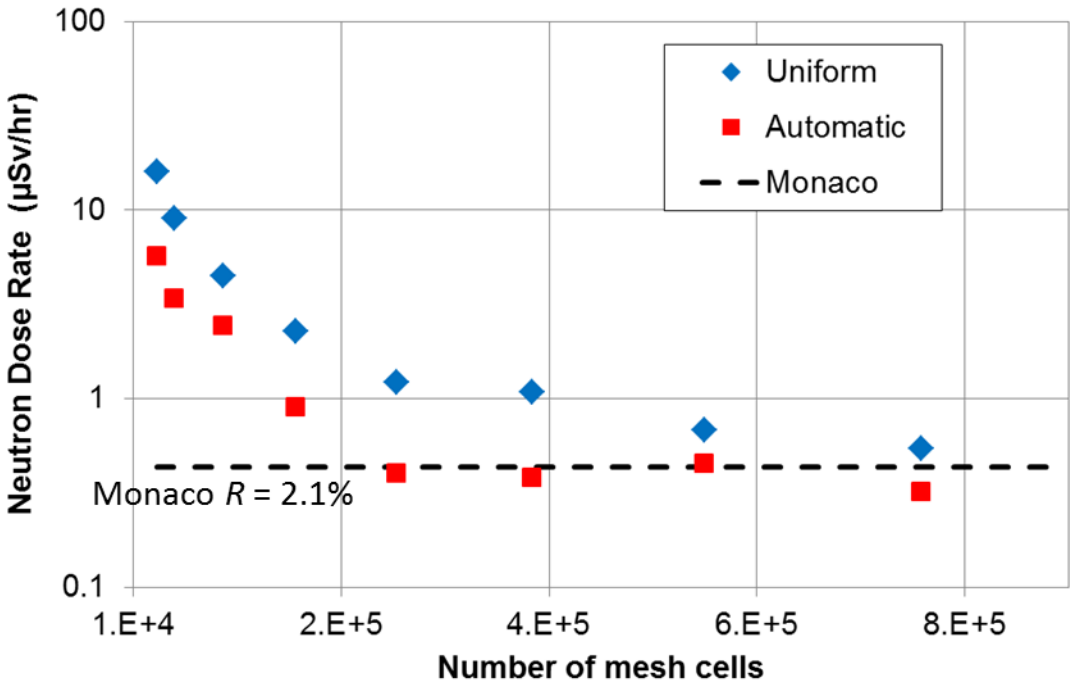

Figure 5.6: Neutron dose rate of spent fuel shipping cask problem

Except for the meshes representing the first point in Fig. 5.6 for which the deterministic running time was less than 10 minutes, the differences in the running time between the deterministic calculations with uniform mesh and the deterministic calculations with an automatically generated mesh did not exceed 10%.

With uniform mesh refinement the neutron dose rate calculated for a mesh having 3.9×10^5 elements was still a factor of 2.0 higher than the neutron dose rate calculated for a mesh with 7.7×10^5 elements. On the contrary, the differences between all the neutron dose rates calculated with meshes having more than 2.6×10^5 elements did not exceed 40.6% with the deterministic mesh refinement algorithm. This shows that, with the deterministic mesh

refinement algorithm, the deterministic calculations started to converge at about half of the elements needed for convergence when the mesh was refined uniformly.

5.3.3 Monte Carlo efficiency

Problem description

The MCNP model of the nuclear development facility bunker described in Sect. 3.3 was used to demonstrate how the efficiency of the MC calculations in a FW-CADIS simulation can be affected by the deterministic mesh refinement algorithm.

The total dose rate of both neutrons and photons is required at five different locations representing the parking lot outside the facility, two locations in the administration office, the roof, and the end of the control area. Figure 5.7 shows the five locations for which the dose rate was calculated in this problem.

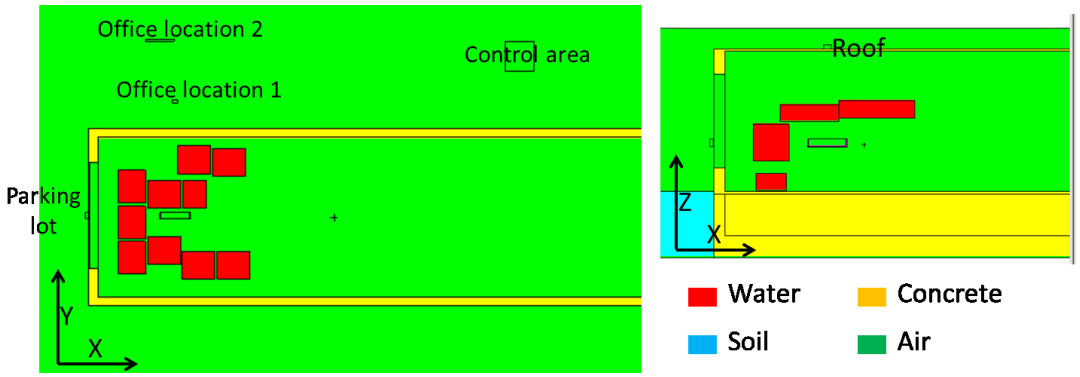

Figure 5.7: Locations of dose rate calculations in nuclear development facility bunker problem

Methodology

ADVANTG was used to employ the FW-CADIS method to provide the WW parameters to accelerate the MCNP calculation of the dose rates at the five locations. Source biasing was not used because the charged particles accelerator only occupies a small volume relative to the overall geometry and neutrons are born inside the D-T gas with the very low density (no attenuation inside source volume).

A uniform mesh for which all the elements were cubic with side length of 25 cm was used for the first FW-CADIS case. This mesh had 184 planes in *X* direction, 104 planes in *Y* direction, 24 planes in *Z* direction, and 4.59×10^{5} total number of elements. Another mesh that was carefully tailored to capture all the important geometric detail of the MCNP model was also used for comparison purposes. Capturing the important details in this problem was only possible because of the simple rectangular geometries of the concrete structure and the water tanks. The carefully tailored mesh had 98 planes in *X* direction, 116 planes in *Y* direction, 46 planes in *Z* direction, and 5.23×10^{5} total number of elements. Finally a mesh created using the deterministic

mesh refinement algorithm, having 83 planes in *X* direction, 96 planes in *Y* direction, 58 planes in *Z* direction, and 4.62×10^5 total number of elements, was used in the analysis. The automatically created mesh used an initial mesh that had 7.18×10^3 of cubic mesh elements with 1 m side length, a MM parameter of 25, and a refinement parameter of 64. The CC approach was used to define the Denovo materials for all the FW-CADIS cases. To isolate the benefit of using the MM approach in materials definition from analyzing the benefit of the mesh quality, the MM approach was not used after the Denovo mesh was determined using the deterministic mesh refinement algorithm. An analog MCNP calculation was also used for comparison.

A 27 neutron, 19 photon groups ENDF-VII library was used for the Denovo calculations and continuous energy libraries were used for the MCNP calculations.

Results

Figure 5.8 shows the deterministic models created for the regions surrounding the accelerator with the three meshes.

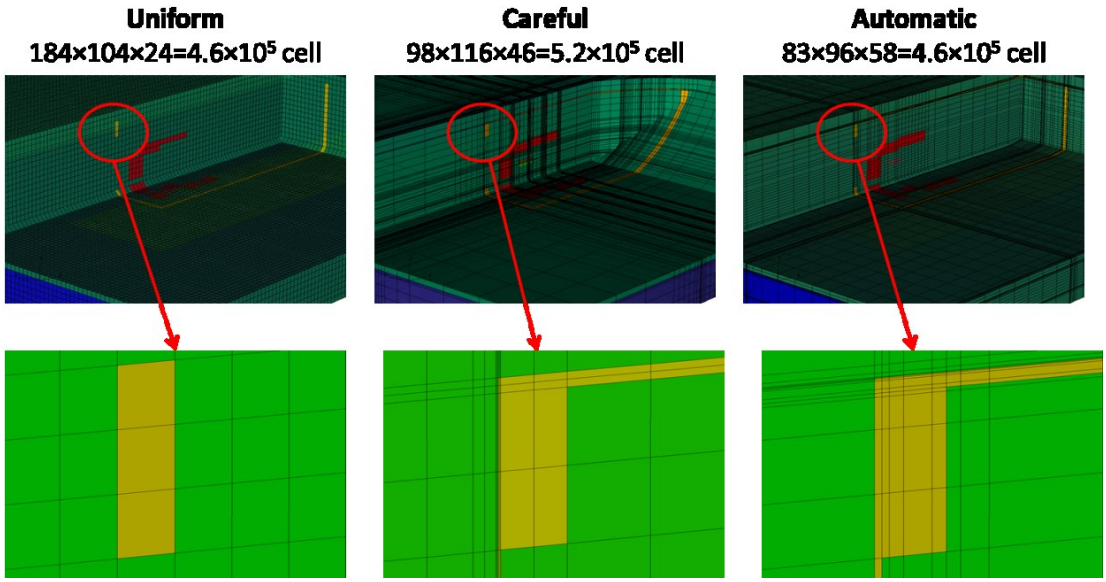

Figure 5.8: Denovo models for nuclear development facility bunker problem

The roof and front gate of the bunker were missed in the uniform deterministic model but were present in the carefully tailored model and the model created by the automatic mesh refinement algorithm.

Figure 5.9 shows the dose rates calculated at the five different locations. None of the three FW-CADIS calculations caused any bias in the final MC dose rates results. At each of the five locations, the differences between the dose rates calculated using each of the four different MC cases including the analog case did not exceed 2σ where σ is the uncertainty of the MCNP case with higher uncertainty.

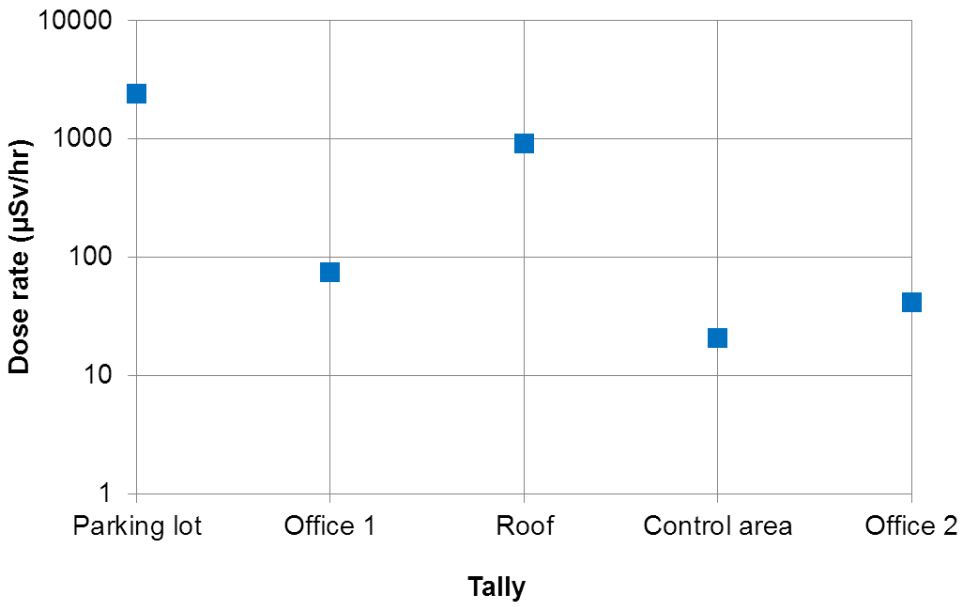

Figure 5.9: Dose rates at different locations for nuclear development facility bunker problem

Since the computational time is controlled by the dose rate tally with the maximum statistical uncertainty, the FOM based on the maximum R (Eq. (2.28)) was used. For calculating the statistical uncertainty in the FOM, the VOV of the tally with maximum R was used in Eq. (2.26).

Figure 5.10 shows the FOMs of the three FW-CADIS cases normalized by dividing them by the analog FOM. The FW-CADIS with uniform mesh provided a factor of 11.0 increase in the MC FOM. The MC FOM of the FW-CADIS case with automatically refined mesh was 55.5% higher than the MC FOM of the FW-CADIS case with uniform mesh, but 21.9% lower than the MC FOM of the FW-CADIS case with the carefully tailored mesh.

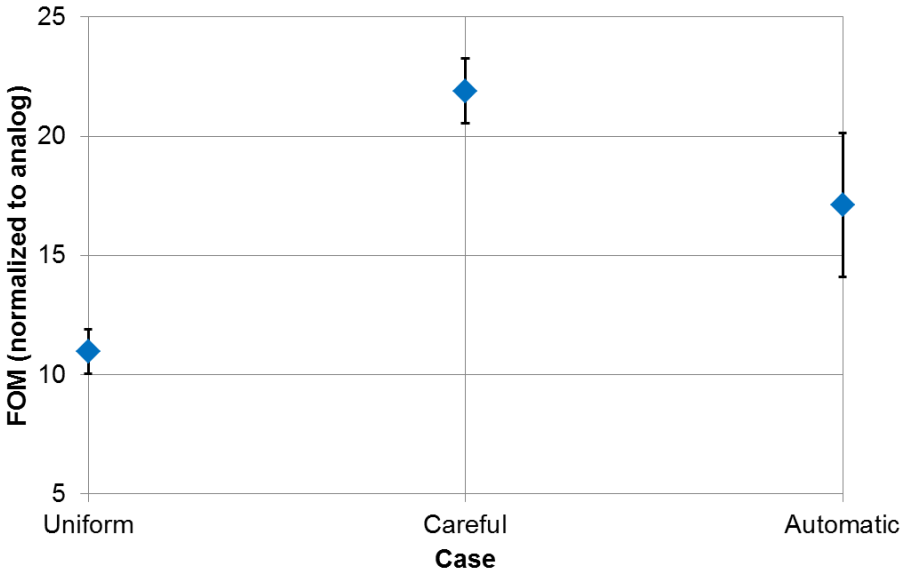

Figure 5.10: FOMs for nuclear development facility bunker problem

The highest *R* in the FW-CADIS case with uniform mesh occurred at the roof, which was missed in the uniform mesh deterministic model. The FOM of the roof tally for the uniform case was 49.9% lower than the carefully tailored case and 45.9% lower than the automatically refined case. The highest uncertainty in the automatically refined case occurred at one of the office locations. The water tanks that were used to shield the office from the neutron source at the accelerator had a 7 cm gap that was missed in the deterministic model developed by the automatic mesh refinement algorithm. Figure 5.11 shows the regions around this gap in both the carefully tailored and the automatically refined deterministic models.

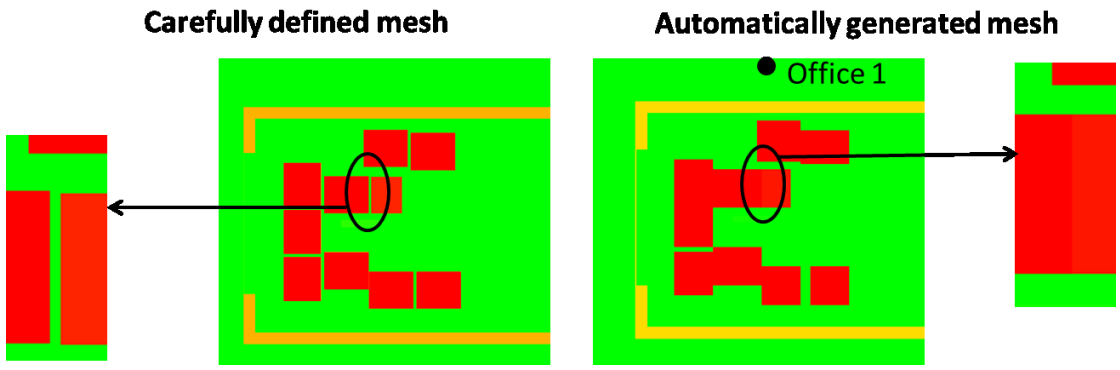

Figure 5.11: Denovo models around gap between water tanks for nuclear development facility bunker problem

For the automatically refined case, the single tally FOM of the dose rate tally in this office location was 51.8% less than of the carefully tailored case, but it was still 15.5% higher than the single tally FOM of the uniform case.

5.4 Conclusion

The deterministic mesh refinement algorithm can be used to automatically refine a coarse initial guess and generate deterministic models that provide good representation of the MC geometries in CADIS and FW-CADIS simulations. *The use of the deterministic mesh refinement algorithm can greatly simplify the difficult and error prone process of manual development of meshes suitable for CADIS and FW-CADIS simulations, but it is usually difficult for the automatically generated deterministic models to exactly represent the MC geometries.*

The recalculation of the MM fractions increases the computational cost of the deterministic mesh refinement algorithm, but the cost of this algorithm is usually small with

respect to the other calculations (deterministic and MC) required by CADIS and FW-CADIS simulations.

Chapter 6: Weight-window coarsening

6.1 Motivation

As shown in Sect. 3.3, the MC calculation will stop if the MC code cannot allocate enough memory to store the WWs. The problem will be more pronounced with parallel processing because the current production-level MC codes (e.g. MCNP) depend on replication of the MC data (geometry, cross-sections, VR parameters, etc.). The parallel MC processes have to share the memory of each computing node. This poses a very restrictive limitation to the deterministic mesh resolution in large and complicated problems because the WWs are generated using the same mesh and energy group structure of the deterministic calculations in CADIS and FW-CADIS simulations. Decoupling the WW and deterministic meshes is necessary to allow the use of finer deterministic calculation without increasing the storage size of the WW maps. An efficient algorithm for reducing the storage size of the WW map should minimize the penalty in the MC efficiency that is expected because of the loss of information by storage reduction.

6.2 Algorithm

Adjoint flux collapsing

It was mentioned in Sect. 2.4.2 that the CADIS and FW-CADIS methods distribute the MC particles according to the contributon fluxes. To test this hypothesis, a water block model with a monoenergetic neutron source was used. Figure 6.1 shows the one group contributon flux and the distribution of the MC particles in a water block with analog MC simulation and with the

CADIS method[6]. The total neutron flux at the detector position represented the tally response and the CADIS adjoint source for this problem.

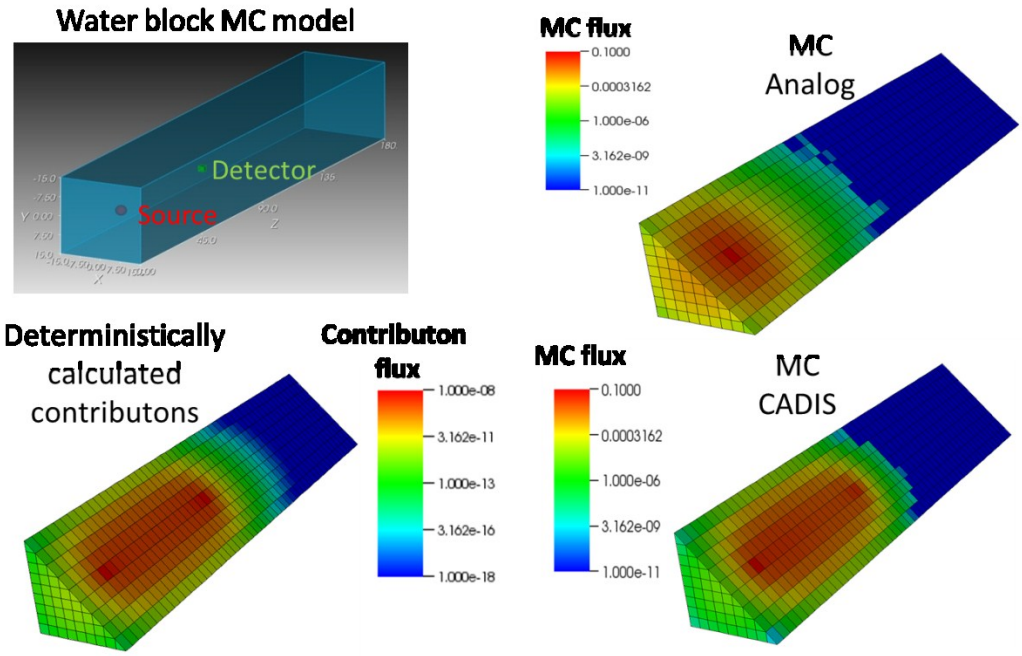

Figure 6.1: MC particle distribution in a water block

It is apparent that the spatial distribution of the contributon flux represents a good estimate for the MC particles distribution of the CADIS calculation.

For formulating a collapsing formula for the adjoint fluxes in CADIS and FW-CADIS simulations, it is logical to try to preserve the contributon flux of the high resolution deterministic calculations because they represent the population of the MC particles throughout

[6] The MC particle flux/fluence in MCNP can be tallied using a certain tally multiplier that divides the tally scores by the particles weights. In this analysis the MCNP source code was modified to tally the MC particle fluxes instead of the real fluxes.

the phase-space domain of the problem. To simplify the formulation, the angular variation of the fluxes will not be considered. By adding the angular dependency to the forward and adjoint fluxes, the derivation can be generalized in a straight forward way[7].

The forward and contributon fluxes corresponding to one coarse space-energy cell, which is composed of several fine space-energy cells, can be evaluated via summation of the fine grid fluxes,

$$\phi_{IJK,G} = \frac{\sum_g \sum_{ijk} \phi_{ijk,g} V_{ijk}}{V_{IJK}} \tag{6.1}$$

and

$$c_{IJK,G} = \phi^{+}_{IJK,G} \phi_{IJK,G} = \frac{\sum_g \sum_{ijk} \phi^{+}_{ijk,g} \phi_{ijk,g} V_{ijk}}{V_{IJK}}, \tag{6.2}$$

where each space-energy cell in the fine grid is identified by its spatial position ijk and energy group g, each coarse space-energy cell is identified by IJK and G, V_{ijk} is the volume of cell ijk in the fine grid, V_{IJK} is the volume of the cell IJK in the coarse grid, $\phi_{ijk,g}$ and $\phi_{IJK,G}$ are the fine and coarse grid fluxes respectively, and $\phi^{+}_{ijk,g}$ and $\phi^{+}_{IJK,G}$ are the fine and coarse grid adjoint fluxes respectively. The ijk and g summations in the R.H.S of Eqs. (6.1) and (6.2) include all the fine space-energy cells that compose the coarse space-energy cell IJK, G.

Equation (6.2) is a conservation relation of the contributon flux between the coarse and the fine grids. By solving both Eq. (6.1) and Eq.(6.2), the adjoint flux of the coarse grid that conserves the contributon flux of the fine grid can be expressed by,

[7] CADIS and FW-CADIS have been usually implemented without considering the angular variation of fluxes. The following development of the adjoint flux collapsing formula and the block contributon parameters will only be accurate for isotropic forward and adjoint fluxes.

$$\phi^{+}_{IJK,G} = \frac{\sum_g \sum_{ijk} \phi^{+}_{ijk,g} \phi_{ijk,g} V_{ijk}}{\phi_{IJK,G} V_{IJK}}. \quad (6.3)$$

Since more of the particles that populate the coarse cell are expected to belong to fine cells with higher forward fluxes, the importance of the coarse cell are expected to be controlled by the importance of the fine cells with higher real (forward) fluxes. It is therefore intuitive to calculate the adjoint flux (importance) of the coarse cell using a flux-weighted average of the adjoint fluxes of the constituent fine cells.

Choice of cells that need collapsing

Since most of the MC computational efforts are spent in tracking the particles [73], achieving high FOM require focusing the MC particles in important phase-space regions. The use of fine meshes increases the fidelity of CADIS and FW-CADIS deterministic calculations, and consequently increases the MC FOM. To minimize the reduction in the MC FOM that is expected with the mesh coarsening necessary to decrease the size of the WW maps, it is desirable to preserve the mesh fidelity in the regions of highest contributon flux, representing the MC particles flux, in CADIS and FW-CADIS simulations. Therefore, mesh cells with lower contributon fluxes should be collapsed before mesh cells with higher contributon fluxes.

Block contributon parameter

Since only structured, simply connected WW maps can be used in MCNP without modification, the space-energy cells removal will be restricted to the removal of spatial (*X*, *Y*, or *Z*) blocks or energy groups. In this thesis, the term block contributon parameter will be used to express the space and energy summations of the product of the contributon flux and the volume of all space-energy cells belonging to each *X*, *Y*, or *Z* block, or to each energy group. These block contributon parameters can be represented by,

$$C_i = \sum_g \sum_{j,k} \phi^+_{ijk,g} \phi_{ijk,g} V_{ijk}, \qquad C_j = \sum_g \sum_{i,k} \phi^+_{ijk,g} \phi_{ijk,g} V_{ijk},$$
$$C_k = \sum_g \sum_{i,j} \phi^+_{ijk,g} \phi_{ijk,g} V_{ijk}, \qquad C_g = \sum_{ijk} \phi^+_{ijk,g} \phi_{ijk,g} V_{ijk}, \tag{6.4}$$

where C_i, C_j, C_k, C_g are the block contributon parameters for each *X*, *Y*, and *Z* block and for each energy group respectively.

Algorithm description

The steps of the WW coarsening algorithm can be summarized as follows:

1. Calculate the contributon fluxes for all the space-energy cells using Eq. (6.2).
2. Calculate the block contributon parameters for all blocks and energy groups using Eqs. (6.4).
3. Calculate the average of the adjoint fluxes for the space-energy cells that belong to the spatial block or the energy group (B_{min}) with the lowest block contributon parameter and the corresponding space-energy cells of the neighboring block $\left(B_{neighbor}\right)$. The adjoint flux collapsing formula (Eq. (6.3)) is used for determining the average adjoint fluxes.
4. Update the adjoint fluxes in the space-energy cells of $B_{neighbor}$ by replacing them with the calculated average.
5. Update the forward fluxes and the volumes of the space-energy cells of $B_{neighbor}$ by adding the corresponding forward fluxes and volumes of B_{min} to the corresponding values of $B_{neighbor}$. No volume changes will occur if B_{min} represents an energy group.
6. Update the block contributon parameter of $B_{neighbor}$ by adding the block contributon parameter of B_{min} to it.

7. Remove the adjoint fluxes and forward fluxes of all the space-energy cells that belong to B_{min} and remove the block contributon parameter of B_{min}.
8. Repeat steps 3-7 until the total number of space-energy elements reaches a user specified value.

If B_{min} is not the first or the last spatial block or energy group (has two neighbors), $B_{neighbor}$ should be the neighboring block or group with the lower block contributon parameter of the two neighbors. The user should determine the total number of space-energy elements in the final WW mesh according to the computer memory available for the MC calculations. The desired final WW mesh resolution can be specified using a collapsing parameter representing the ratio between the total number of space-energy elements in the fine deterministic mesh and the total number of space-energy elements in the coarse WW mesh. In CADIS and FW-CADIS calculations, the total response TR is calculated using Eq. (2.9). This requires that both the real (forward) source and the adjoint flux use the same mesh. Since the WW coarsening algorithm changes the adjoint flux mesh, it should only be implemented after calculating TR in CADIS and FW-CADIS simulations.

6.3 Demonstration

6.3.1 Monte Carlo efficiency without deterministic geometry discretization

Problem description

To study the effect of WW coarsening on the MC FOM without interference of geometry discretization errors, the MC model in Fig. 6.2 was used.

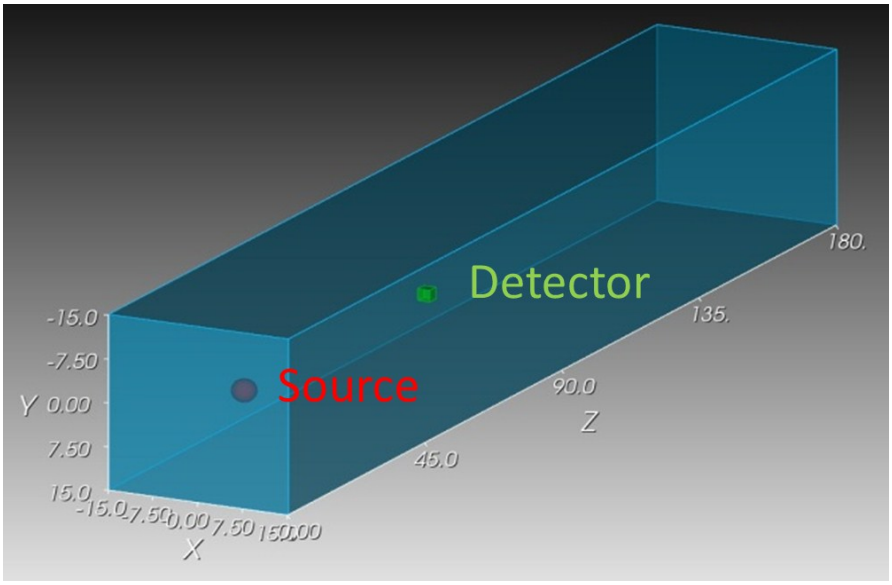

Figure 6.2: MCNP model for water block problem

The model represents a rectangular parallelepiped water block with a 180 cm length and a 30×30 cm^2 cross sectional area. A monenergetic 1 MeV isotropic point source was placed at the

center of the cross sectional area, 15 cm from front plane of the water block. A cubic detector with side length of 2 cm was separated from the source by 60 cm and from the other end of the water block by 105 cm. Only neutrons were modeled in this problem. The total neutron flux at the detector was the response being tallied.

Methodology

ADVANTG was used to implement the CADIS method for calculating the total neutron flux in the detector. The adjoint source was defined as a cube with the same dimensions and at the same location as the detector. A multi-group ENDF-VII library with 27 neutron groups was used for the Denovo calculations. The adjoint source spectrum was uniform over all the energy groups.

Two spatial grids were used in the deterministic calculations. The coarse grid had uniform cubic mesh elements with side length of 6 cm and contained 750 mesh elements. The fine grid had uniform cubic mesh elements with side length of 1.2 cm and contained 93,750 elements. Together with the 27 neutron group structure of the multi-group library, both of these grids were used in both the adjoint deterministic calculation and the WW map of the MC simulation.

The adjoint fluxes of the fine grid were then collapsed to the coarse structure. The collapsing was performed uniformly by using a flux weighted average of the adjoint fluxes according to Eq. (6.3) and using a simple average of the adjoint fluxes. For these two cases, the fluxes of each 125 fine cells that coincided with one coarse WW cell were averaged. The WW coarsening algorithm was then used to find an efficient WW map with a total number of space-energy cells similar to the coarse grid and collapse the fine fluxes to this new structure.

Results

Figure 6.3 shows the neutrons weights for the coarse and fine mesh cases and the three collapsed cases. To calculate the one group neutrons weights for the cases shown in Fig. 6.3, the inverse of the sum of the reciprocals of the group-wise weights generated by ADVANTG was used.

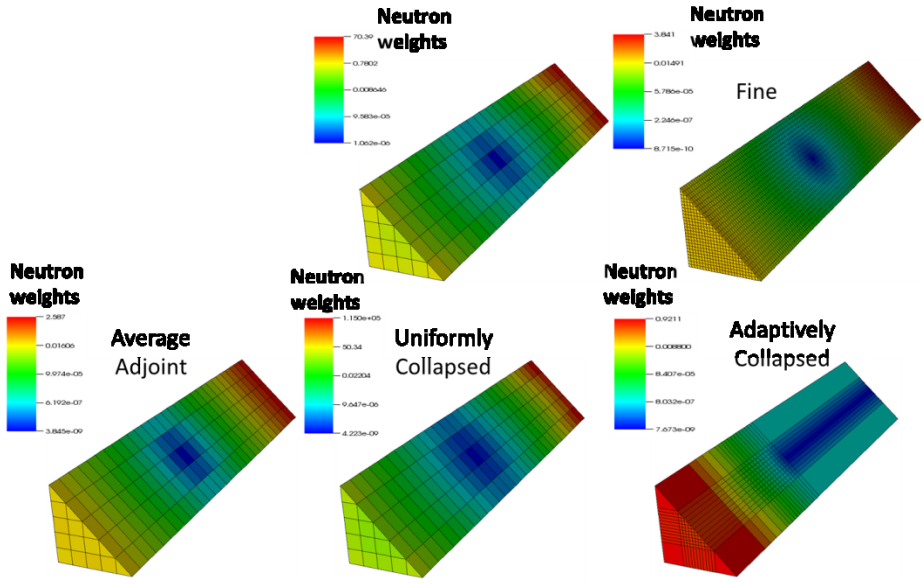

Figure 6.3: One group neutron weights for water block problem

The WW splitting and rouletting is needed to increase the population of the MC particles as they get emitted from the source till they score at the tally location. The coarsening in the mesh created by the WW coarsening algorithm only occurred away from the optical path between the source and the detector. This shows that the WW coarsening algorithm only removes the cells with the least importance to the WW acceleration of the MC calculation.

To reduce the size of the WW map, the WW coarsening algorithm increased the importance (reduced the weights) of the region behind the detector. The impact of this unphysical change in regions importance on decreasing the MC FOM is not expected to be large because the MC particles flux, shown in Fig. 6.1, is much smaller behind the detector than between the source and the detector. Rouletting the MC particles behind the detector will not be as effective in increasing the MC FOM as splitting the particles between the source and the detector.

Table 6.1 shows the results of the fine and coarse meshes and the three collapsed CADIS simulations. The FOM was calculated using Eq. (2.23) and the statistical uncertainty in the FOM was calculated using Eq. (2.26). The time in the denominator of Eq. (2.23) was corrected to include the run time of the deterministic calculation and the MC run time.

Table 6.1: Total flux and FOMs for water block problem

Calculation	Number of space-energy cells (Thousands)	Neutron flux (n/cm^2-sec)	Normalized FOM (deterministic correction)
Analog	n/a	16.00 ± 48.56%	1.00 ± 56.0%
Coarse	20	10.91 ± 1.73%	3.15E+03 ± 3.2%
Fine	2531	10.85 ± 0.19%	2.52E+05 ± 1.0%
Average adjoint flux	20	10.89 ± 0.21%	2.06E+05 ± 1.0%
Uniform adjoint flux collapsing	20	10.88 ± 0.20%	2.19E+05 ± 1.0%
WW coarsening	19	10.90 ± 0.18%	2.70E+05 ± 1.0%

Even with the inclusion of the time of the extra forward deterministic calculation, the FOM for the uniform adjoint flux collapsing case was 6.3% higher than FOM of the simple

average case. The FOM with the WW coarsening algorithm was 23.3% higher than the FOM of the uniform collapsing case and 31.1% higher than the simple average case. Compared to the coarse mesh calculation, the use of the WW coarsening algorithm in collapsing the fluxes to the coarse WW structure provided a factor of 85.7 increase in the FOM even though both cases used WW maps with similar overall size.

The FOM of the WW coarsening case is 7.1% larger than the FOM of the fine case although a penalty in MC efficiency is expected because of loss of information with any WW storage size reduction. As mentioned in Sect. 2.4.2 and 3.3, the use of more accurate adjoint fluxes does not guarantee an increase in the FOM because the importance function used in the importance sampling scheme is not directly related to the FOM or the tally variance. Figure 6.4 shows the effect of the degree of collapsing (collapsing parameter) on the MC FOM with the deterministic run time correction for this problem.

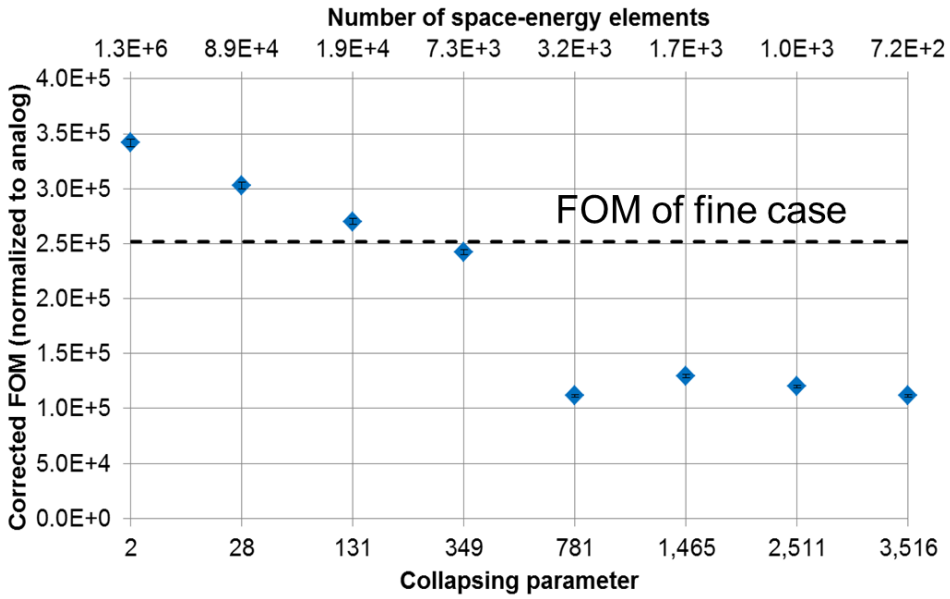

Figure 6.4: FOM versus degree of WW coarsening for water block problem

Even with a factor of 3,516 reduction in the storage size of the WW map, the reduction in the FOM was only 67.25%. This shows that the WW coarsening algorithm minimizes the reduction in the MC efficiency because it only removes the cells with the least importance (low contributon) to the MC solution.

6.3.2 Generic Monte Carlo efficiency analysis

Problem description

To analyze the effects of the WW coarsening algorithm on the FOM of realistic FW-CADIS simulations, the nuclear development facility bunker problem described in Sect. 3.3 and

5.3 was used. No changes were made to the problem geometry, the neutron source, or the tallies as described in Sect. 5.3.

Methodology

In Sect. 5.3, the deterministic model created by the deterministic mesh refinement algorithm did not capture the 7 cm gap between the water tanks when the maximum number of mesh elements was specified to correspond to the total number of mesh elements in the carefully hand-tailored deterministic model which had 0.523 million cells. By allowing the deterministic model to have more about 2.6 times more mesh elements, the model created by the deterministic mesh refinement algorithm captured all the gaps between the water tanks. Figure 6.5 shows the three deterministic models created by the careful manual specification of the locations of the grid planes and by the deterministic mesh refinement with an upper limit of 1.4 million cells.

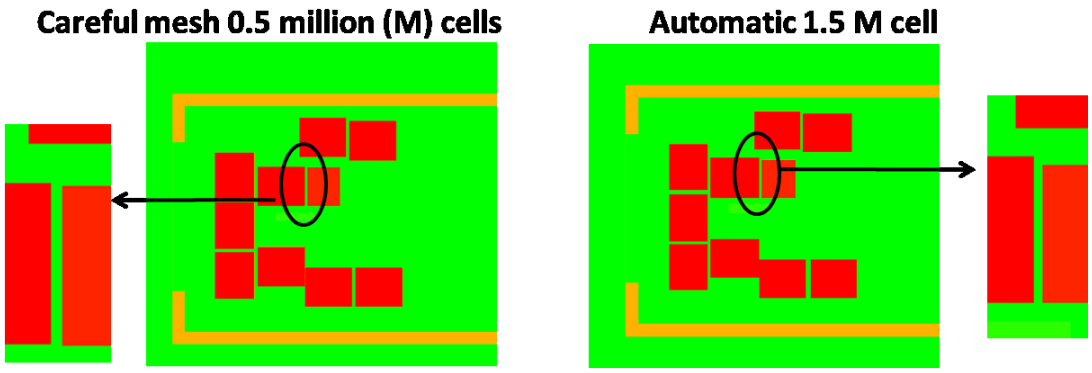

Figure 6.5: Denovo models around gap between water tanks for nuclear development facility bunker problem

For the size of the WW map not to increase by the extra refinement of the deterministic mesh, the WW coarsening algorithm was used to reduce it to the size of the WW map used with the carefully hand-tailored case.

Results

The two additional cases, which used the deterministic mesh refinement algorithm with an upper limit of 1.4 million cell (with and without WW coarsening), were compared to the other three cases described in Sect. 5.3. The differences between the dose rates calculated in the two additional cases and any of the other cases, used for the calculations in Sect. 5.3, did not exceed 2.2σ for any of the tallies.

Figure 6.6 shows the FOM of all the cases. The FOM of the automatically refined case, which had 2.6 times more mesh elements than the carefully hand-tailored mesh case, was 18% lower than the FOM of the carefully hand-tailored mesh case and 68.2% higher than the uniform mesh case.

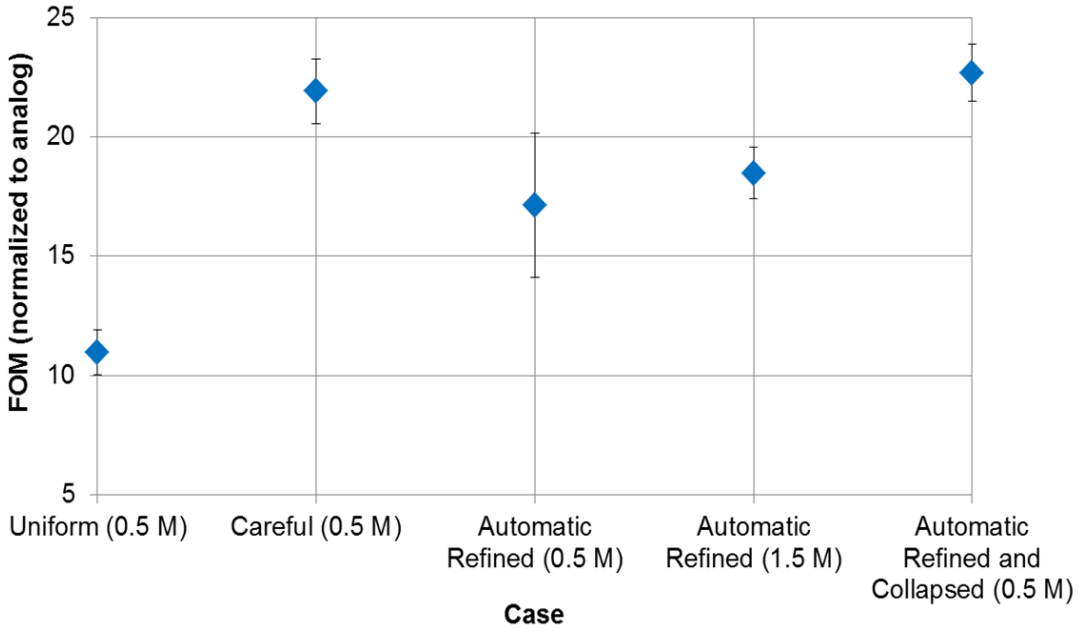

Figure 6.6: FOMs for nuclear development facility bunker problem

With the WW-coarsening of this automatically refined case, the FOM did not decrease despite of the factor of 2.7 reduction in the size of the WW map. This shows that the decrease in the FOM because of the loss of mesh fidelity is minimal with the WW coarsening algorithm, and can be even less than the changes in the FOM caused by other contributing factors such as the effects of the WW values on the MC variance. As mentioned in Sect. 2.4.2 and Sect. 3.3, the later factors [73; 85] are not the focus of this thesis. The FOM of the WW-coarsening case, which had the same size of the carefully hand-tailored mesh case, was nearly equal (3.7% higher) to the FOM of the carefully hand-tailored mesh case.

6.4 Conclusion

The adjoint flux collapsing decouples the space-energy mesh of the WW maps from the space-energy mesh of the deterministic calculations. This allows the use of finer mesh resolutions in the deterministic calculations of CADIS and FW-CADIS simulations because the deterministic mesh will no longer be restricted by the size of the WW maps that can represent a problem for running the MC calculations especially with parallel processing. Using a flux-weighted average of the adjoint fluxes in developing the coarsened WW maps of CADIS simulations has proved to provide a better FOM than using a simple average of the adjoint fluxes.

By only removing the cells with the least importance to the MC calculations, the WW coarsening algorithm minimizes the reduction in the FOM that is expected with any averaging scheme because of the loss of mesh fidelity.

Chapter 7: ITER prompt dose rate

For analyzing the effects of the algorithms developed in this thesis, the ITER global prompt dose rate calculation described in Ref. [4] was used. The goal of this analysis was to emphasize the importance of the high-fidelity, full-scale modeling of large and complicated problems. In Ref. [4], it was shown that an accurate MC calculation of the prompt dose rate at a single point outside the biological shield (bioshield) will require at least 393 processors-years. Because of the difficulty of such a calculation, previous assessments have depended on coupling the final 3-D analysis with 1- or 2-D analyses [91]. These approaches ignore critical geometric detail such as the large diagnostics ports, which increases the prompt dose rate by a factor higher than 100 [4].

The FW-CADIS calculation described in Ref. [4] was repeated using the MM approach, the deterministic mesh refinement, and the WW-coarsening algorithms.

Methodology

The ITER 3-D model, Alite03, was used in the form of an MCNP5 input file representing a 40° sector of the ITER device [92]. Figure 7.1 shows the Alite03 model. The MCNP5 input file, for which the geometry description exceeded 19,800 lines, was built from the previously used BRAND model [93] and updated using MCAM [94], a CAD-MCNP interface program developed by the Fusion Design Study Team at the Institute of Plasma Physics, Hefei, China.

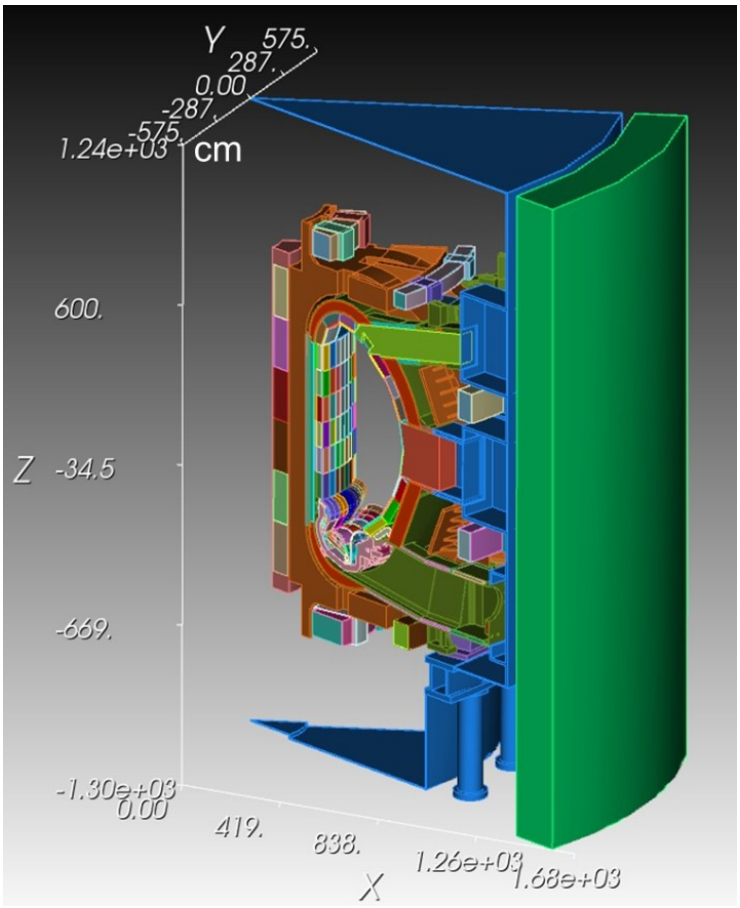

Figure 7.1: ITER MC model (Alite03)

A Cartesian mesh tally with uniform cubic mesh elements of side length equal 10 cm was used to tally the total (neutron+photon) prompt operational dose rates throughout the entire ITER experimental facility.

ADVANTG was used to employ the FW-CADIS method for this analysis. The source biasing parameters were not used because, in some testing cases, they did not change by more than one order of magnitude because the source particles were emitted in vacuum. The adjoint

source was defined to include all the ITER geometry. The group-wise energy spectrum of the adjoint source was defined as the flux-to-dose-rate conversion factors in an energy structure equivalent to that of the multi-group data library of the deterministic calculation.

For the forward and adjoint Denovo calculations not to require more than 32 processors, the number of mesh elements in all the Denovo calculations was set not to exceed 8 million cells. A uniform cubic mesh with side length of 16.36 cm was used with and without the use of the MM approach for materials definitions. The automatic deterministic mesh refinement algorithm was used to automatically create a mesh with the same total number of mesh elements. An initial mesh with 1.3×10^{6} elements was used for the automatically refined case. This initial mesh had uniform side lengths of 32.7 cm in the *Y* direction and 35.3 cm in the *Z* direction. The dimensions of the mesh elements were varied in the *X* direction to capture the fluxes gradient in the bioshield and the inner shielding layers. After the final mesh was automatically developed using the deterministic mesh refinement algorithm, the MM approach was used for the materials definitions in the Denovo model. The WW coarsening algorithm was also used to collapse the fluxes the automatically refined FW-CADIS case by factors of 2, 4, 8, 16, and 32.

A 46 neutron group 21 gamma group FENDL 2.1 library was used for the Denovo calculations and a continuous energy FENDL 2.1 library was used for the MCNP calculation.

7.1 Effect of macromaterials and deterministic mesh refinement

Figure 7.2 shows the CDFs of the mesh tally relative uncertainties (*R*s) for an analog MC calculation and the three FW-CADIS cases that did not use the WW coarsening. The MCNP running time was fixed at 10 days for each of the four cases.

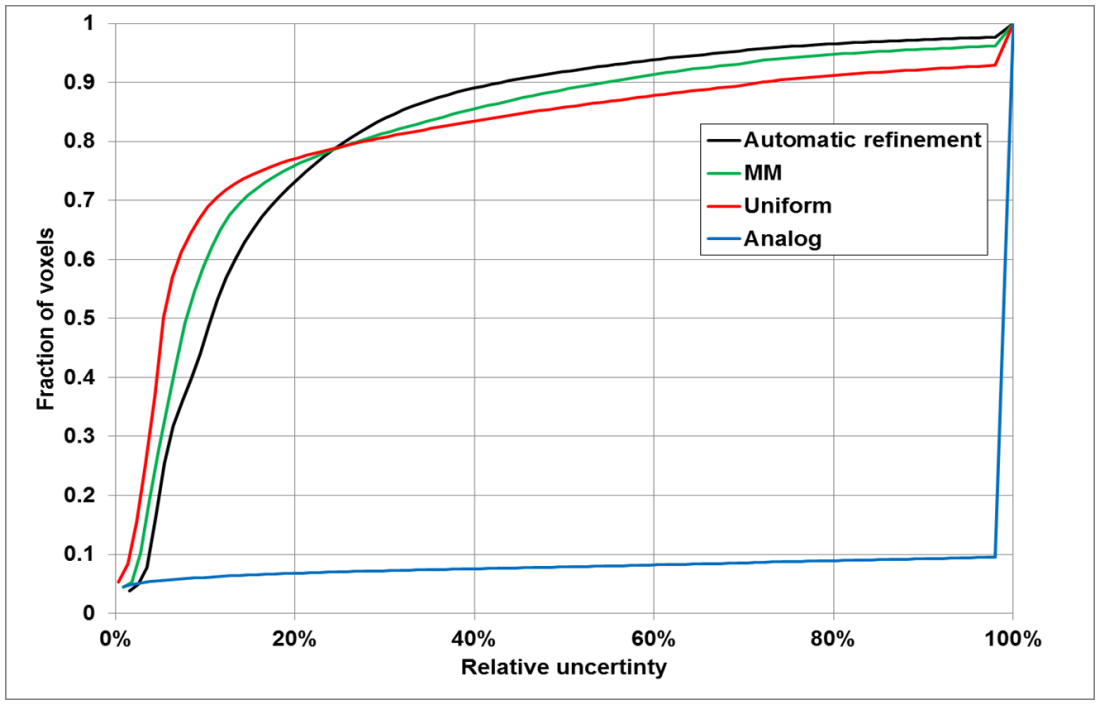

Figure 7.2: CDFs of mesh tally *R* for 10 day MC calculations of analog MC case and three FW-CADIS cases for ITER prompt dose rate problem

The maximum *R* for 90% of the mesh tally voxels is 72.1% for the uniform mesh case, 54.4% for the MM case with no mesh refinement, and 43.8% for the deterministic mesh refinement case. Based on these preliminarily calculations, the minimum MCNP computer time

required for any of these FW-CADIS cases to have 90% of the mesh tally voxels with R below 10% is 191.8 processor-day.

Table 7.1 shows the computer time taken by the three FW-CADIS cases. The initialization times include the time spent in developing the Denovo models for the FW-CADIS calculations.

Table 7.1: Computational time of three FW-CADIS cases for ITER prompt dose rate problem

Case	Time (hr)		
	Initialization	Deterministic	MC
Uniform	0.6	195.2	240.5
MM	16.6	1514.7	240.5
Automatic	14.1	222.6	240.5

The adjoint Denovo calculation of the FW-CADIS case that used the MM approach and did not use deterministic mesh refinement algorithm took 56.85 processor-days which is at least a factor of 9.1 longer than any of the other Denovo calculations. The version of Denovo that was used in this calculation stored all the homogenized materials on every processor, which dramatically increased the required memory and the calculation time. The current version of Denovo only replicates the clean materials and builds only the mixed materials needed on the remote processors. Both the deterministic and initialization times will be considered small compared to the computer time required by a more accurate and reliable MCNP calculation, which exceeds 190 processor-day. For initialization times of the MM case with no mesh refinement and the automatic mesh refinement case to be close, the MM parameter used for the

MM case with no mesh refinement was set to be 5 and the MM parameter of the automatic mesh refinement case was set to be 3.

Table 7.2 shows the fraction of the mesh tally voxels that had MC scoring and the FOM defined using Eq. (2.29) for the three FW-CADIS cases. These FOMs were normalized by dividing them by the FOM calculated for the analog case. The Rs of the zero scoring voxels were assumed to be 100%.

Table 7.2: MC FOM and fraction of mesh tally voxels with MC scoring for three FW-CADIS cases for ITER prompt dose rate problem

Case	Fraction of nonzero voxels	Normalized FOM
Uniform	95.5%	7.2
MM	97.5%	9.1
Automatic	98.3%	11.1

The use of the MM approach in creating the deterministic models increased the fraction of voxels with MC scoring by 2.1% and the use of the deterministic mesh refinement algorithm in automatically creating the Denovo models increased the fraction of voxels with MC scoring by 2.9%. This is equivalent to 53,120 and 74,002 more voxels with MC scoring due to the use of the MM approach and the deterministic mesh refinement respectively. The calculated dose rate on the central plane of ITER and on a plane rotated 20° from the central plane are shown in Fig. 7.3 for the three FW-CADIS cases. The automatically refined case, which also the MM approach for materials definitions, had more voxels with MC scoring in the upper diagnostics port, which is plugged by 5 m of shielding materials, and in the equatorial port which is plugged by 2 m of

shielding materials. Since it is difficult for the MC particles to score in the shielding plugs of these ports, the extra scoring in these regions shows that the WW parameters of the automatically refined case are more accurate.

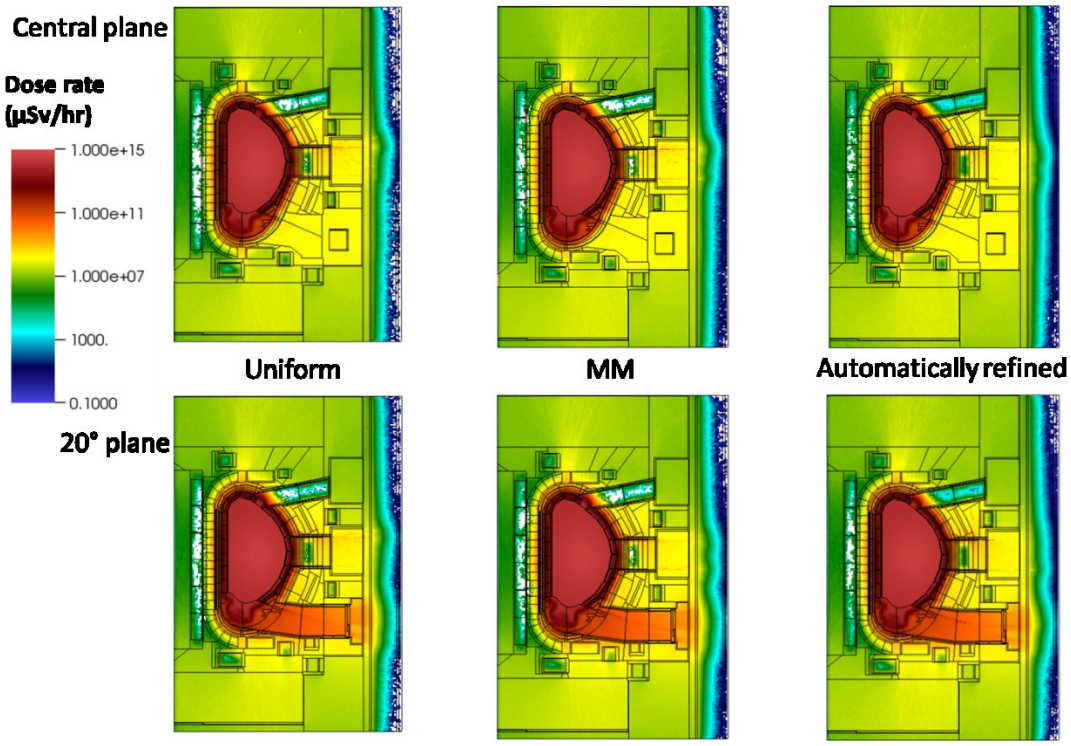

Figure 7.3: Dose rate map on central plane and on plane rotated 20° from central plane for three FW-CADIS cases of ITER prompt dose rate problem

In addition to the more efficient distribution of the scores of the MC particles, the FOM of the MM case is 26.4% higher than the uniform case and the FOM of the automatically refined case is 54.2% higher than with the uniform case.

7.2 Effect of weight-window coarsening

Figure 7.4 shows the CDFs of the mesh tally *R*s of 10 day MCNP runs of the automatically refined FW-CADIS case and the five FW-CADIS cases that used the WW coarsening algorithm to reduce the size of the WW map of the automatically refined FW-CADIS case by factors of 2, 4, 8, 16, and 32. The computational time of the WW coarsening algorithm was less than 20 hrs for all the cases.

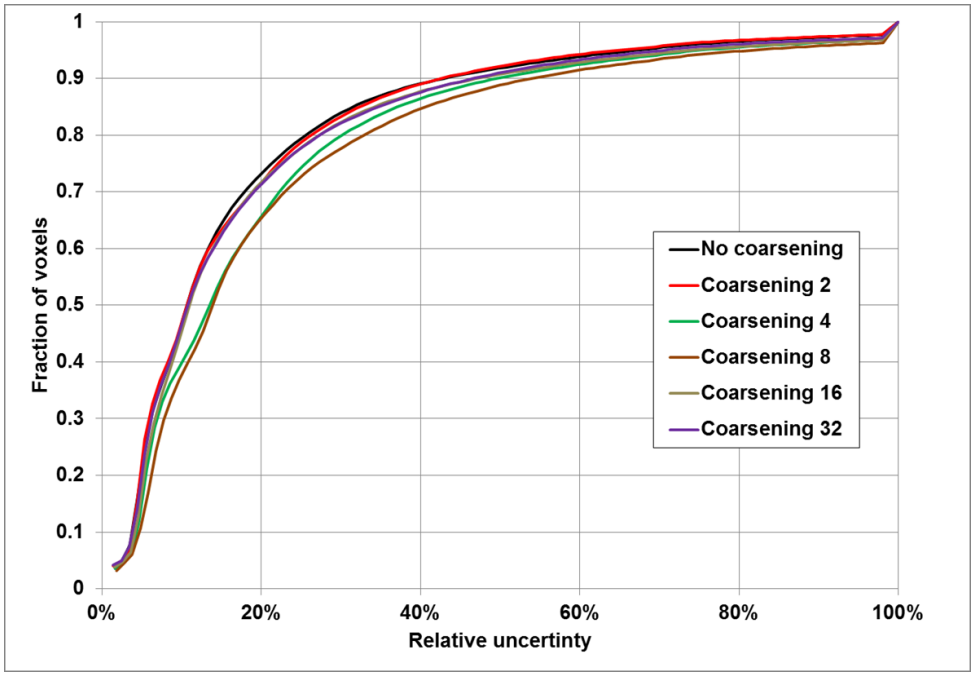

Figure 7.4: CDFs of mesh tally *R* for 10 days MC calculations of FW-CADIS cases with WW coarsening for ITER prompt dose rate problem

Table 7.3 shows the fraction of scoring voxels and global MC FOM for the 10 day MCNP runs of the 6 FW-CADIS cases. The FOMs were calculated using Eq. (2.29) and normalized to the analog FOM values. The *R*s of the zero scoring voxels were assumed to be 100%.

Table 7.3: MC FOM and fraction of mesh tally voxels with MC scoring for FW-CADIS cases with WW coarsening for ITER prompt dose rate problem

Case	Size of WW file (GB)	Fraction of nonzero voxels	Normalized FOM
No coarsening	6.5	98.3%	11.1
Coarsening 2	3.3	98.3%	11.2
Coarsening 4	1.7	97.8%	9.0
Coarsening 8	0.8	97.5%	8.2
Coarsening 16	0.4	97.6%	9.7
Coarsening 32	0.2	97.8%	10.1

For all the cases with the reduced size WW maps, the decrease in the fraction of the nonzero scoring mesh tally voxels was less than 1% and the decrease in the MC FOM was less than 26.1%. The systematic reduction in the fraction of voxels with calculated MC answers is 0.5% and the systematic reduction in the FOM is 9%. These reductions in the MC efficiency can easily be overthrown by the large reduction in the size of the WW map that can greatly facilitate the parallel processing of the MC calculation

7.3 Combined effect of macromaterials, deterministic mesh refinement, and weight-window coarsening

As noted in Sect. 7.1, even with the FW-CADIS method, an accurate and reliable MCNP calculation of a problem with the magnitude and complexity of this problem requires hundreds of processors-days. Performing such a calculation without parallel processing is difficult. Since the size of the WW map can represent the limiting factor on the number of MCNP jobs that can be run in parallel, it is illustrative to compare the MC efficiencies of different FW-CADIS cases with similar WW map sizes.

Figure 7.5 shows the CDFs of the mesh tally R of two 10 day MCNP runs that used two FW-CADIS cases, for which the WW maps had similar sizes and occupied about 0.41 GB of hard disk space.

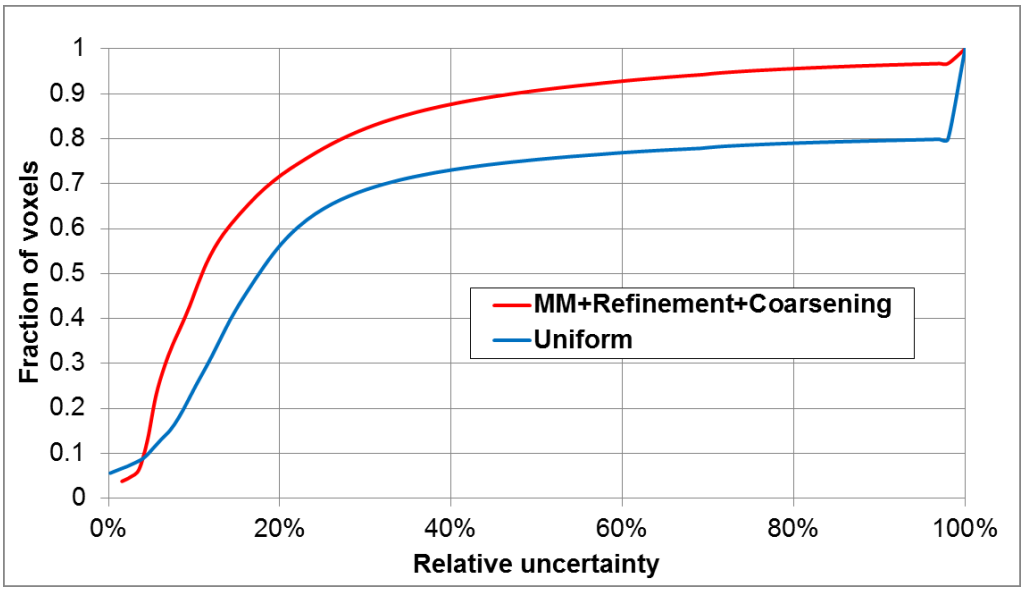

Figure 7.5: CDFs of mesh tally *R* for 10 day MC calculations of FW-CADIS cases with 0.410 GB WW map for ITER prompt dose rate problem

The first FW-CADIS case did not use any of the algorithms developed in this thesis. The Denovo model of this calculation used a uniform mesh for which the elements had side lengths between 40 cm and 42.33 cm. The total number of space-energy elements in the Denovo model of this case was 32.6×10^6. The second FW-CADIS case used the same automatically refined Denovo model created for the automatic refinement case of Sect. 7.1. This Denovo model contained 528.0×10^6 space-energy elements. The WW coarsening algorithm was used to reduce the number of space-energy elements in the WW map of this case to 32.7×10^6.

Table 7.4 shows the fraction of nonzero scoring mesh tally voxels and the MC FOM of the two FW-CADIS cases. The FOMs were calculated using Eq. (2.29) and normalized to the analog FOM values. The *R*s of the zero scoring voxels were assumed to be 100%.

Table 7.4: Fraction of mesh tally voxels with scoring and the MC FOM of two FW-CADIS cases with 0.410 GB WW map for ITER prompt dose rate problem

Case	Fraction of nonzero voxels	Normalized FOM
No adaptivity	81.9%	3.5
Adaptivity	97.6%	9.7

Similarly, Fig. 7.6 shows the CDF of the mesh tally R of two 10 days MCNP runs of two FW-CADIS cases with WW maps which occupied about 0.21 GB of hard disk space. Because of the reduced memory requirements, the MCNP runs with these maps were more convenient to perform then the cases shown of 7.5. The first FW-CADIS case used Denovo models with mesh elements having side lengths between 50.8 cm and 51.43 cm. None of the algorithms developed in this thesis were used in this case. The second FW-CADIS case used the automatically refined Denovo model. The WW coarsening algorithm was used to refine the number of space-energy elements in the WW map to 16.3×10^6 elements.

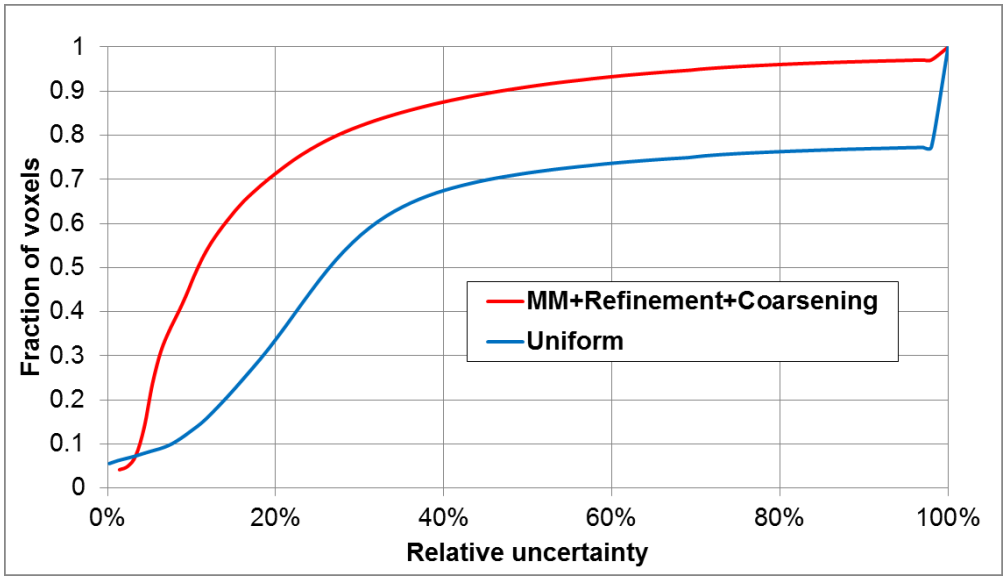

Figure 7.6: CDFs of mesh tally *R* for 10 days MC calculations of FW-CADIS cases with 0.206 GB WW map for ITER prompt dose rate problem

Table 7.5 shows the fraction of nonzero scoring mesh tally voxels and the MC FOM of these two FW-CADIS cases. The FOMs were calculated using Eq. (2.29) and normalized to the analog FOM values. The *R*s of the zero scoring voxels were assumed to be 100%.

Table 7.5: Fraction of mesh tally voxels with scoring and the MC FOM of two FW-CADIS cases with 0.206 GB WW map for ITER prompt dose rate problem

Case	Fraction of nonzero voxels	Normalized FOM
No adaptivity	79.3%	3.0
Adaptivity	97.8%	10.1

For the FW-CADIS cases with WW maps occupying about 0.21 GB of hard disk space, the use of the algorithms developed in this thesis provided 23.3% increase in the fraction of the nonzero scoring mesh tally voxels. This is equivalent to 501,477 more voxels with calculated MC answers. The calculated increase in the MC FOM was a factor of 3.4. Recalling from Sect. 2.3.4, the magnitude of the overestimation in the FOM based on the average relative variance (R^2) is proportional to the number of replacements in the Rs of the zero scoring voxels by 100%. Because the number of zero scoring voxels with the FW-CADIS case that used the three algorithms was 9.4 times smaller than the FW-CADIS case that did not use any of the algorithms, the real (asymptotic) increase in the MC FOM is expected to be higher than the calculated value. The high increase in the MC FOM can significantly reduce the time needed for performing such a difficult MC simulation.

7.4 Reliability of ITER prompt dose rate calculation

The large reduction in the size of the WW map of the automatically refined FW-CADIS case enabled performing a 460 days MCNP calculation by parallel processing on the computer cluster of the UW-Madison Department of Engineering Physics. For this calculation, 87.5% of the mesh tally voxels had Rs below 10% and the MC scoring occurred in 98.7% of the voxels. Figure 7.7 shows the dose rate map on the central plane of the model and on a plane rotated 20° from the central plane.

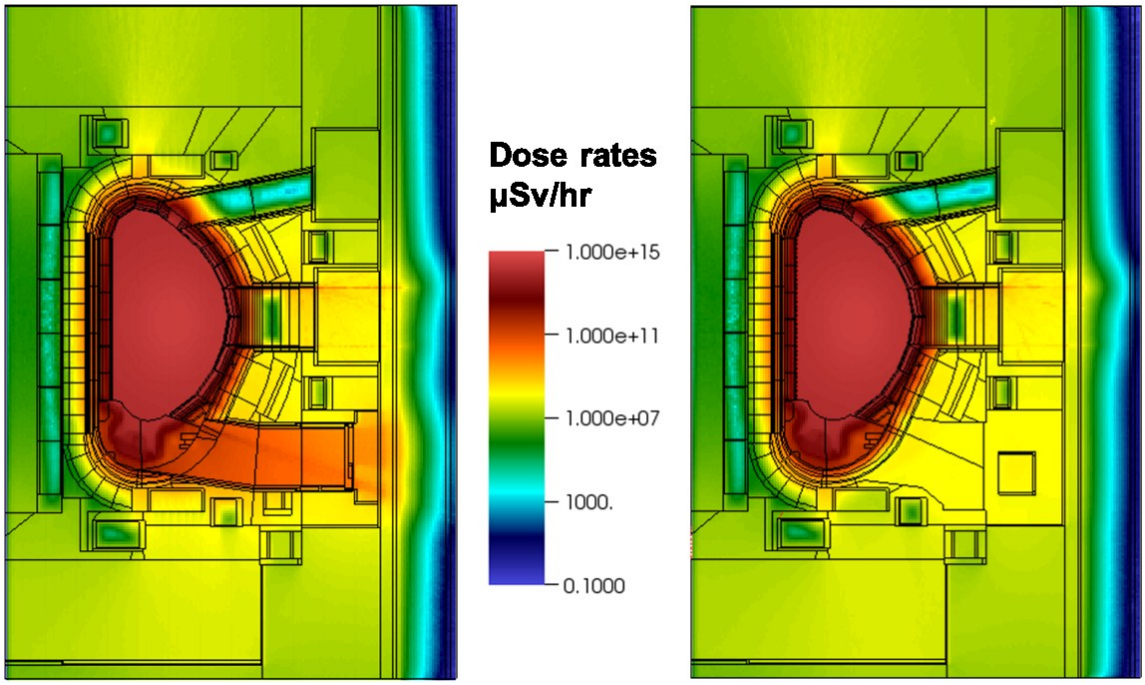

Figure 7.7: Dose rate map on central plane and on plane rotated 20° from central plane for 220 days MCNP runs of ITER prompt dose rate problem with FW-CADIS and three algorithms developed in thesis

The effects of the neutrons and photons streaming through the ITER ports on the dose rates at the bioshield is described in Ref. [4].

To develop confidence in the accuracy of our FW-CADIS calculation, the global MC results at four points were compared to the results of two other complementary approaches. The four points represent interesting positions inside and outside the bioshield at mid-plane and bottom of the tokomak. The positions of the four points used in the validation of the global MC calculation are shown in Fig. 7.8.

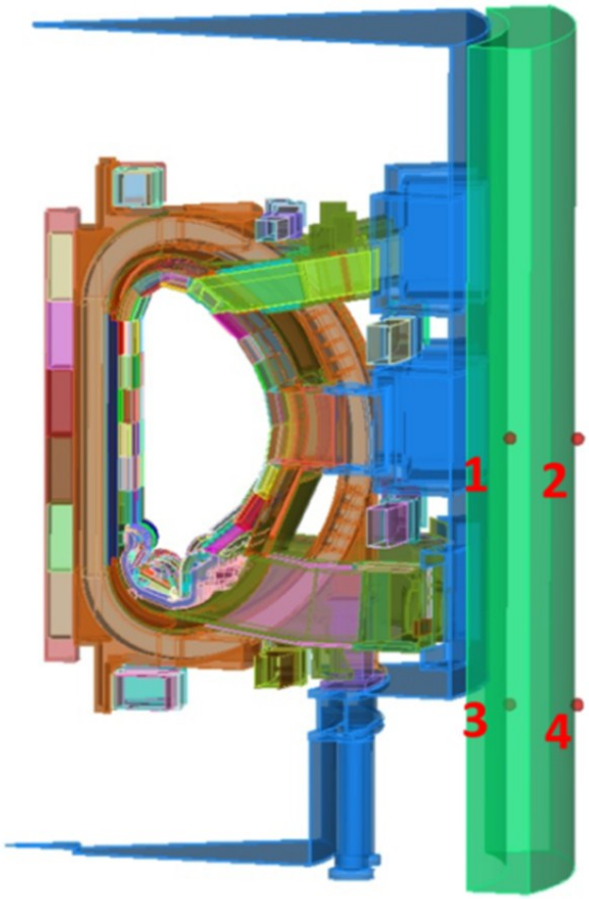

Figure 7.8: Positions of the four points used in validation of ITER prompt dose rate global MC calculation

The results of the global MC calculation at these four points were compared to results from a MC calculation using four point-detectors at the four positions. The use of the FW-CADIS method was necessary for this calculation since the computer time required for doing such a calculation using conventional MC simulations is too large. Compared to global problems, the MC convergence is much faster when the FW-CADIS method is optimizing localized tallies. Four point adjoint sources were specified for this calculation, with an energy spectrum equal to the flux-to-dose-rate conversion factors in the 46 neutron/21 gamma energy

group structure of the multi-group library used in the deterministic calculation. The use of the next event estimator of the point-detector tally instead of the track length estimator of the mesh tally provided another sort of complementarity between the two calculations. The dose rates at these four positions were also compared to the dose rates calculated deterministically in a very fine mesh standalone Denovo calculation. This high-performance-computing (HPC) calculation was performed on the ORNL supercomputer, Jaguar, using a 1.34 billion cell model. An approximate source peaked in the plasma zone and a 46-neutron/21-gamma FENDL2.1 library was used for the HPC Denovo calculation for which the input file was created by ADVANTG. Table 7.6 shows the dose rates calculated at the four points using the mesh tally, the point-detectors, and the HPC Denovo calculations.

Table 7.6: Dose rates calculated at four points for ITER global prompt dose rate problem

Points	Mesh tally (μSv/hr)	Point-detector (μSv/hr)	Denovo (μSv/hr)
1	$1.9\times10^{7} \pm 7.9\%$	$2.8\times10^{7} \pm 5.5\%$	2.2×10^{7}
2	$17 \pm 8.6\%$	$15 \pm 4.4\%$	14.2
3	$4.2\times10^{6} \pm 0.9\%$	$5.3\times10^{6} \pm 2.1\%$	4×10^{6}
4	$2.7 \pm 21.0\%$	$2.3 \pm 2.8\%$	1.8

Considering the 13 to 14 orders of magnitude attenuation between the source region and points 2 and 4 and the 7 to 8 orders of magnitude attenuation between the source and points 1 and 3, the global MC results had very good agreement with both the point-detector and the HPC Denovo results. The maximum relative difference between the point-detector results and the

global MC results is 42.1% while the maximum relative difference between the global MC results and the Denovo results is 32.6%. These differences are also physically expected because the global MC results are averaged across cubical mesh cells 10 cm on a side, the Denovo results are averaged across cubical mesh cells 2 cm on a side, and the point detector results are not averaged.

7.5 Conclusion

The significant increase in the MC efficiency of FW-CADIS simulations due to the use of the MM approach, the deterministic mesh refinement algorithm, and the WW coarsening algorithm enable the simulation of very difficult shielding problems. When the three algorithms were combined, performing an accurate and reliable FW-CADIS calculation of the prompt dose rate throughout the entire ITER reactor was feasible using the computer cluster of the UW-Madison Engineering Physics Department. The results of such calculation agreed at four points with a very fine mesh calculation that was performed on the ORNL super-computer, Jaguar.

Chapter 8: Summary and future work

8.1 Summary and conclusions

The high efficiency gains provided by the hybrid MC/deterministic techniques CADIS and FW-CADIS methods allow the simulations of problems that are very difficult using analog MC or traditional MC techniques. Several practical issues arise when the CADIS and FW-CADIS methods are being used with large and complicated problems. First, the automation of the creation of the deterministic input file is necessary because the manual development of these files is extremely difficult for such problems. Second, the resolution of the mesh used in the deterministic calculation is limited by the availability of computing resources for the deterministic calculations and the memory requirements of the MC calculations. Capturing all the physical and geometric details is not guaranteed with the coarse meshes of the deterministic calculations that traditionally used unsophisticated automatic algorithms for materials definitions. Inconsistencies between deterministic and MC models may arise because of "missing" important geometric detail during the development of the deterministic models. These inconsistencies decrease the MC efficiency and, if severe, they can affect the MC reliability. ***The goal of this thesis was to enhance the efficiency and the reliability of CADIS and FW-CADIS simulations of large and complicated shielding problems by minimizing the inconsistencies between the deterministic and the MC models. As explained below, the enhanced fidelity of the deterministic calculations provided by the three algorithms developed in this thesis increases the efficiency and reliability of the CADIS and FW-CADIS simulations without increasing their computational time or memory requirements.***

To increase the fidelity of the deterministic calculation without exceeding the total number of mesh cells which determines the computing resources requirements, the MM approach and deterministic mesh refinement algorithm were developed.

The MM approach provides a method for homogenizing the materials of each mesh cell in the deterministic models. By providing better mass conservation and decreasing the geometry discretization errors, the MM approach was found to increase the accuracy of the deterministic calculations without increasing the computational time requirement. The increased accuracy of the deterministic solutions increases the efficiency of the MC calculations of CADIS and FW-CADIS simulations. The MM approach was also used to automatically define the adjoint sources for space-dependent responses in CADIS and FW-CADIS simulations.

For a fixed number of mesh elements, the deterministic mesh refinement algorithm seeks an efficient mesh that can minimize the geometry discretization errors, which are inevitable for geometrically complex problems. The algorithm takes the guesswork out of developing an appropriate, problem-dependent mesh for the deterministic calculations. By increasing the fidelity of the deterministic models, the deterministic mesh refinement algorithm was found to increase the accuracy of the deterministic solutions and the efficiency of the MC calculations in CADIS and FW-CADIS simulations.

Using finer mesh resolutions is desirable for CADIS and FW-CADIS simulations because it reduces both the truncation and the geometry discretization errors of the deterministic calculations, and consequently increases the CADIS and FW-CADIS simulation efficiency. Due to the one to one correspondence between the deterministic and the WW mesh in CADIS and FW-CADIS simulations, the deterministic mesh resolution is not just limited by the availability

of computing resources, but also limited by the size of the WW maps developed for the MC calculations. The last limitation can be very restrictive with parallel processing because the production-level MC codes (e.g. MCNP) depend on the replication of the MC data (geometry, cross-sections, WW parameters, etc.). For overcoming this restrictive limitation, a WW coarsening algorithm was developed. The WW coarsening algorithm uses a flux weighted average of the adjoint fluxes to decouple the space-energy mesh of the WW maps from the mesh and energy group structure of the deterministic calculations. This flux weighted average conserves the deterministic estimate of the MC particles as represented by the contributon flux, which was approximated by the product of the space- and energy- dependent scalar forward and adjoint fluxes of each space-energy cell. By conserving the contributon fluxes of the deterministic calculations, the weights generated by the adjoint flux collapsing formula are controlled by the weights of the collapsed mesh cells with higher fluxes. The flux-weighted average of the adjoint fluxes has proved to provide higher MC efficiency than the simple average of the adjoint fluxes. The WW coarsening algorithm carefully chooses the space-energy cells that get removed to be the cells with the least MC particles flux (contributon flux). This minimizes the reduction in the MC FOM that is expected with any averaging scheme.

The three algorithms were used in calculating the prompt dose rate throughout the entire ITER experimental facility. This calculation represents a very challenging shielding problem because of the immense size and complexity of the ITER structure and the presence of a 2 m bioshield. Compared to a FW-CADIS calculation with the same storage size of the VR parameters, the use of the three algorithms increased the regions for which the MC results were achieved by 23.3.% and increased the efficiency of the MC calculation by a factor of 3.4 for a 10 days MCNP calculation. Because of the significant increase in the MC efficiency without any

increase in the memory requirement, the use of the three algorithms with FW-CADIS enabled the simulation of this difficult shielding problem on a regular computer using parallel processing of the MC calculations. The results of the parallel MC calculation agreed at four points with a very fine mesh deterministic calculation that was performed on the ORNL super-computer Jaguar.

8.2 Topics for future research

Parallelization of the MM approach and using MC ray-tracing capability for calculating the MM fractions

Even when the MM approach was used, the computer time spent in developing the deterministic models for the CADIS and FW-CADIS simulations was much smaller than the time of the deterministic or the MC calculations for all the test cases in this thesis. Therefore, no attempts were made to speed up the MM sampling. When the MM approach was used in the deterministic mesh refinement algorithm, reducing the MM parameter was essential for reducing the computer time needed for calculating the MM fractions in some problems.

To reduce the clock-time needed for creating the deterministic models, the MM approach can be implemented using parallel processing. This might not require extensive modifications to the current implementation in SCALE6.1 and ADVANTG because the MM sampling in each mesh cell is independent on the other cells and only requires information about the original materials in the MC model.

It has been demonstrated that the MC ray-tracing techniques can calculate the MM fractions faster and with higher accuracy than the point sampling method used in this thesis [89]. Future implementations of the MM approach will heavily depend on the use of the ray-tracing techniques especially in the UW-Madison code DAG-MCNP.

Optimizing the implementations of the deterministic mesh refinement algorithm

In the current implementation of the deterministic mesh refinement algorithm, the position of the inserted planes is restricted to the midpoint of the block with highest block heterogeneity parameter. For large blocks, this implementation can create extra cells which might not be needed to capture more geometric detail. If each block was queried for the first position at which the heterogeneity occurred, the implementation of the deterministic mesh refinement algorithm can be enhanced. Since this information will be readily available if the MC ray-tracing techniques are used for calculating the MM fractions, the modification might not require extensive work if the MC ray-tracing techniques are used instead of the point sampling method.

Deterministic mesh refinement based on cross-sections

Since the primary goal of the algorithms developed in this thesis is to enhance the efficiency and the reliability of modeling large and complicated problems, the savings in both human and computer times were crucial in determining the effectiveness of the algorithms. Deterministic mesh adaptivity algorithms based on fluxes information were not investigated because they require the iterative repetition of the deterministic calculations. Algorithms based on macroscopic cross-sections will require the recalculation of the macroscopic cross-section at each refinement step. Even though this might not require much more computationally intensive

calculations, these algorithms were not investigated because the details involved are beyond the scope of this thesis.

WW coarsening based on true contributon fluxes

The WW coarsening algorithm implemented in ADVANTG uses the product of the energy-dependent scalar flux and the energy-dependent scalar adjoint flux to calculate the deterministic estimate of the MC particles flux in each space-energy cell. This approximation can only represent the true contributon flux if both the forward and adjoint fluxes were isotropic. Quadrature integrals of the angular moments of the forward and adjoint fluxes can be used to provide a better approximation of the contributon flux at each space-energy cell. This might be needed for using the WW coarsening algorithms problems that have strong particles streaming because of the high angular variations in the forward and adjoint fluxes.

Bibliography

[1] Evans, T. M. (2010). Denovo: A radiation transport code for nuclear applications. *Workshop on Leadership-class Machines, Petascale Applications, and Performance Strategies.* Snowbird, Utah: Center of Scalable Application Development Software (CScADS).

[2] Wagner, J., & Haghighat, A. (1998). Autotmated variance reduction of Monte Carlo shielding calculations using the discrete ordinates adjoint function. *Nuclear Science and Engineering , 128*, 186.

[3] Wagner, J., Blakeman, E., & Peplow, E. (2009). Forward-weighted CADIS method for variance reduction of Monte Carlo calculations of distributions of multiple localized quantities., (pp. Proceeding of the 2009 International Conference on Advances in Mathematics, Computational Methods, and Reactor Physics). Saratoga Springs, NY.

[4] Ibrahim, A. M., Sawan, M. E., Mosher, S. W., Evans, T. M., Peplow, D. E., Wilson, P. P., et al. (2011). Global Evaluation of Prompt Dose Rates in ITER Using Hybrid Monte Carlo/Deterministic Techniques. *Fusion Science and Technology, 60* , 676-680.

[5] Lewis, E., & Miller, W. (1993). *Computational Methods of Neutron Transport Theory.* La Grange Park, IL: American Nuclear Society.

[6] Williams, M. (1991). Generalized Contributon Response Theory. *Nuclear Science and Engineering , 108*, 335.

[7] Bell, G. I., & Glasstone, S. (1970). *Nuclear Reactor Theory.* Malabar, Florida: Krieger Publishing Company.

[8] Alcouffe, R., Baker, R., Dahl, J., & Turner, S. (2002). *PARTISN manual.* Los Alamos, NM: Los Alamos National Laboratory, LA-UR-02-5633.

[9] Rhoades, W., & Simpson, D. (1997). *The TORT Three-Dimensional Discrete Ordinates Neutron/Photon Transport Code (TORT Version 3).* Oak Ridge, TN: Oak Ridge National Laboratory, ORNL/TM-13221.

[10] Wareing, T., Mcghee, J., Barnett, A., Faillla, G., & Davis, I. (2006). Capabilities of Attila for radiation protection and shielding. *Transactions American Nuclear Society*, *95*, p. 659.

[11] Evans, T., Stafford, A., Slaybaugh, R., & Clarno, K. (2010). Denovo a New Three-Dimensional Parallel Discrete Ordinates code in SCALE. *Nuclear Technology , 171*, 171.

[12] Patton, B., & Holloway, J. (2002). Application of preconditioned GMRES to the numerical solution of the neutron transport equation. *Annals of nuclear energy* , 109.

[13] Morel, J. E. (1999). *Deterministic Transport Methods and Codes at Los Alamos.* Los Alamos, NM: Los Alamos National Laboratory, LA-UR-99-3566.

[14] Ibrahim, A., Henderson, D., El-Guebally, L., Wilson, P., & Sawan, M. (2007). *Assessment of radiation streaming through ARIES-CS He-Access Pipes using two- and three-dimensional analyses.* University of Wisconsin-Madison Fusion Technology Institute, UWFDM-1331.

[15] Badruzzaman, A. (1990). Nodal methods in transport theory. In L. &. Becker, *Advaces in Nuclear Science & Technology, Vol. 21* (p. 5). Plenum Press.

[16] Morel, J., Wareing, T., Mcghee, J., & Evans, T. (1998). *Geometrically- Compatible 3-D Monte Carlo and Discret- Ordinates Methods.* Los Alamos, NM: Los Alamos National Laboratory, LA-98-1886.

[17] Wareing, T. A., McGhee, J. M., & Morel, J. E. (1996). ATTILA: A Three-Dimensional Unstructured Tetrahedral-Mesh Discrete Ordinates Code. *Transactions of the American Nuclear Society*, (pp. 146-147). Washington, D.C.

[18] Kalos, M., & Whitelock, P. (1986). *Monte Carlo Methods-Volume 1: Basics.* New York, NY: John Wiley &Sons.

[19] Carter, L., & Cashwell, E. (1975). *Particle Transport Simulations with the Monte Carlo Method.* ERDA Critical Review Series, TID-26607.

[20] Brown, F., & Sutton, T. (1996). *Monte Carlo Fundamentals.* NY: Knolls Atomic Power Laboratory, KAPL-4823.

[21] Brown, F., Kiedrowski, B., & Bull, J. (2010). *MCNP5-1.60 Release Notes.* Los Alamos, NM: Los Alamos National Laboratory, LA-UR-10-06235.

[22] Hendricks, J., & Booth, T. (1985). MCNP Variance Reduction Overview. *Lecture Notes in Physics* , 240.

[23] Haghighat, A., & Wagner, J. (2003). Monte Carlo Variance Reduction with Deterministic Importance Functions. *Progress in Nuclear Energy , 42*, 25.

[24] Booth, T., & Hendricks, J. (1984). Importance Estimation in Forward Monte Carlo Calculations. *Nuclear Technology , 5*, 90.

[25] Lui, L., & Gardner, R. (1997). A Geometry-Independent Fine-Mesh Based Monte Carlo Importance Generator. *Nuclear Science and Engineering , 125*, 188.

[26] Booth, T. (1985). *A sample problem for variance reduction in MCNP.* Los Alamos, NM: Los Alamos National Laboratory, LA-10363-MS.

[27] X-5 Team Monte Carlo;. (2003). *MCNP - A General Monte Carlo N-Particle Transport Code, Version 5 Volume I: Overview and Theory.* Los Alamos, NM: Los Alamos National Laboratory.

[28] Rice, J. (1995). *Mathematical Statistics and Data Analysis (2nd edition).* Duxbury Press.

[29] Booth, T. (2004). Ex post facto Monte Calro variance redution. *Nulcear Science and Engineeing , 148*, 391.

[30] Booth, T. (1992). Analytic Monte Carlo Score Distributions for Future Statistical Confidence Interval Studies. *Nuclear Science and Engineering , 112*, 159.

[31] Forster, R., Pederson, S., & Booth, T. (1991). Two Proposed Convergence Criteris for Monte Carlo Solutions. *Transaction American Nuclear Society*, *64*, p. 305.

[32] Noack, K. (1991). Efficiency and Reliability in Deep-Penetration Monte Carlo Calculations. *Annals of Nuclear Energy , 18*, 309.

[33] Peplow, D., Bowman, S., Horwedel, E., & Wagner, J. (2006). Monaco/MAVRIC: Computational Resources for Radiation Protection and Shielding in SCALE. *Transaction American Nuclear Society*, *95*, p. 669.

[34] Vieira, W., & Stevens, P. (1995). Analysis of the smapling distribution in Monte Carlo radiation transport calculation. *Annals of Nuclear Energy , 22*, 51.

[35] Booth, T. E. (2007). Unbiased Monte Carlo Estimation of the Reciprocal of an Integral. *Nuclear Science and Engineering, 156* , 403-407.

[36] Peplow, D., Blakeman, E., & Wagner, J. (2007). Advanced variance reduction stratigies for optimizing mesh tallies in MAVRIC. *Transactions American Nuclear Society*, (p. 595).

[37] Kiderowski, B., & Ibrahim, A. (2011). Evaluating the efficiency of estimating numerous Monte Carlo tallies. *Transactions American Nuclear Society*, *AN*, p. In press. Hollywood, FL.

[38] Soran, P., Mckeon, D., & Booth, T. (1990). Calculation of Monte Carlo Importance Functions for Use in Nuclear-Well Logging Calculations. *IEEE Transactions on Nuclear Science*, *37*, p. 936.

[39] Larsen, E. (2003). *Final Report - Hybrid Monte Carlo - Deterministic Methods for Nuclear Reactor - Related Criticality Calculations.* Departmenr of Energy, DE-FG07-00ID-13920.

[40] Wigner, E. (1945). *Effect of small perturbation on pile period.* Metallurgical Laboratory (now Argonne National Laboratory), CP-G-3048.

[41] Kahn, H. (1956). *Applications of Monte Carlo.* Rand Coorporation, RM-1237-AEC.

[42] Goertzel, G., & Kalos, K. (1958). Monte Carlo methods in transport problems. *Progress in Nuclear Energy , 2*, 315.

[43] Kalos, M. (1963). Importance Sampling in Monte Carlo Shielding Calculations: I. Neutron Penetration Through Thick Hydrogen Slabs. *Nuclear Science and Engineering , 16*, 227.

[44] Coveyou, R., Cain, V., & Yost, K. (1967). Adjoint and Importance in Monte Carlo Application. *Nuclear Science and Engineering , 27*, 219.

[45] Bowman, S. (2011). SCALE 6: Comprehensive Nuclear Safety Analysis Code System. *Nuclear Technology, 174 , 97*, 126-148.

[46] Tang, J., & Emmet, M. (2006). *SAS4: A Monte Carlo Cask Shielding Analysis Module Using an Automated Biasing Procedure.* Oak Ridge, TN: Oak Ridge National Laboratory, ORNL/TM-2005/39.

[47] West, J., Hoffman, T., & Emmet, M. (1997). *MORSE-SGS for the SCALE System.* Oak Ridge, TN: Oak Ridge National Laboratory, NUREG/CR-0200.

[48] Hoffman, T., & Tang, J. (1982). *XSDRNPM Biasing of MORSE-SGC/S Shipping Cask Calculations.* Oak Ridge, TN: Oak Ridge National Laboratory, ORNL/CSD/TM-175.

[49] Tang, J., & Hoffman, T. (1998). Monte Carlo shielding analysis using an automated biasing procedure. *Nuclear Science and Engineering , 99*, 329.

[50] Wright, G., Shuttleworth, E., Grimstone, M., & Bird, A. (2002). The Status of the General Radiation Transport Code MCBEND. *Proceeding on an International Topical Meeting on Industrial Radiation and Radioisotope Measuerement Apllications.* Bologna, Italy.

[51] Miller, P., Wright, G., & Boyle, G. P. (1990). The use of an inbuilt importance generator for acceleration of the Monte Carlo Code MCBEND. *Proceeding of International Conference in Physics of Reactor Operation, Designe and Computation*, (p. 124). Marseille, France.

[52] Both, J., Mazzolo, A., Petit, O., Peneliau, Y., & Roesslinger, B. (2003). *User Manual for version 4.3 of the TRIPOLI-4 Monte Carlo method particle transport code.* Saclay, France: CEA, CEA-R-6044.

[53] Dijkstra, E. (1959). A note on two problems in connecion with graphs. *Numerische Mathematik , 1*, 269.

[54] Both, J., Nimal, J., & Vergnaud, T. (1990). Automated importance generation and biasing techniques for Monte Carlo shielding techniques by the TRIPOLI-3 code. *Progress in Nuclear Energy , 24*, 273.

[55] Sweezy, J., Brown, F., Booth, T. C., & Preeg, B. (2005). Automated variance reduction for MCNP using deterministic methods. *Radiation Protection Dosimetry , 116*, 508.

[56] Mickael, M. (1995). A fast, automated, semi-deterministic weight windows generator for MCNP. *Nuclear Science and Engineering , 119*, 34.

[57] Gardner, R., & Liu, L. (1999). Monte Carlo simulation of neutron porosity oil well logging tools: combining the geometry-independent fine-mesh importance map and one-dimensional diffusion model approaches. *Nuclear Science and Engineering , 133*, 80.

[58] Alcouffe, R., Baker, R., Brinkley, F. M., & O'dell, R. (1995). *DANTSYS: A Diffusion Accelerated Neutral Particle Transport Code System.* Los Alamos, NM: Los Alamos National Laboratory.

[59] Van Riper, K., Urbatsch, T., Soran, P., Parsons, D., Morel, J., Mckinney, G., et al. (1997). AVATAR- Automated Variance Reduction in Monte Calro Calculations. *Proceeding Joint International Conference on Mathematical Methods and Supercomputing in Nuclear Applications.* Saratoga Springs, NY.

[60] Hendricks, J., & Culberstson, C. (2000). An Assessment of MCNP Weight Windows. *Proceedings of the PHYSOR 2000 ANS International Topical Meeting on Advances in Reactor Physics and Mathematics and Computation into the next Millennium.* Pittsburgh, PA.

[61] Wagner, J. (1997). *Acceleration of Monte Carlo Shielding Calculation with an Automated Variance Reduction Technique and Parallel Processing (PhD Thesis).* The Pennsylvania State University.

[62] Haghighat, A., Hiruta, H., Petrovic, B., & Wagner, J. (1999). Performance of the Automated Adjoint Accelerated MCNP (A3MCNP) for simulation of a BWR core shroud problem. *Proceeding of International Conference on Mathematics and Computation in Reactor Physics, and Environmental Analysis in Nuclear Applications.* Madrid, Spain.

[63] Wagner, J. C. (2002). An automated Deterministic Variance Reduction Generator for Monte Carlo Shileding Applications. *Proceedings of the American Nuclear Society 12th Biennial RPSD Topical Meeting.* Santa Fe, NM.

[64] Mosher, S., Miller, T., Evans, T., & Wagner, J. (2009). Automated weight-window generation for threat detection applications using ADVANTG. Saratoga Springs, NY: Proceeding of the 2009 Internationals Conference on Advances in Mathematics, Computational Methods, and Reacotry Physics.

[65] Peplow, D., & Wagner, J. (2006). Automated variance reduction for SCALE shielding calculations. *Proceeding of ANS 14the Biennial Topical Meeting of the Radiation Protection and Shielding Division.* Carlsbad, NM.

[66] Peplow, D. E. (2011). Monte Carlo Shielding Analysis Capabilities with MAVRIC. *Nuclear Technology, 174* , 289-313.

[67] Oak Ridge National Laborarory Report. (2009). *SCALE: A modular code system for performing Standradized Computer Analyses for Licensing Evaluations, Version 6, Vos. I-III.* Radiation Safety Information Center (CCC-750), ORNL/TM-2005/39.

[68] Turner, S., & Larsen, E. (1997). Automatic variance reduction for three-dimensional Monte Carlo simulations by the local importance function transform-I: Analysis. *Nuclear Science and Engineering , 127*, 22.

[69] Turner, S. L. (1997). Automated variance reduction for three-dimensional Monte Carlo simulations by the local importance function transform-II: numerical results. *Nuclear Science and Engineering , 127*, 36.

[70] Cooper, M., & Larsen, E. (2001). Automated weight windows for global Monte Carlo particle trnasport calculations. *Nuclear Science and Engineering , 137*, 1.

[71] Becker, T. (2009). *Hybrid Monte Carlo/Deterministic Methods for Radiation Shielding Problems (PhD thesis).* Ann Arbor, MI: University of Michigan.

[72] Hoogenboom, J. (2008). Zero-Variance Monte Carlo Schemes Revisited. *Nuclear Science and Engineering , 160*, 1.

[73] Solomon, C. J. (2010). *Discrete-Ordinates Cost Optimization of Weight-Dependent Variance Reduction Techniques for Monte Carlo Neutral Particle Transport (PhD thesis).* Manhattan, Kansas: Kansas State University.

[74] Peplow, D. E., Mosher, S. W., Evans, T. M., & Wagner, J. C. (2010). Hybrid Monte Carlo/Deterministic Methods for Streaming/Beam Problems. *Proceedings of American Nuclear Society Radiation Protection and Shielding Division 2010 Topical Meeting*, (pp. 18-23). Las Vegas, NV.

[75] Wagner, J., Peplow, D., Mosher, S., & Evans, T. (2010). Review of hybrid (deterministic/Monte Carlo) radiation transport methods, codes, and applications at Oak Ridge National Laboratory. *Proceeding of Joint Conference of Supercomputing in Nuclear Apllications and Monte Carlo (SNA + MC2010), Hitotsubashi Memorial Hall.* Tokyo, Japan.

[76] Wagner, J. C., Mosher, S. W., Evans, T. M., Peplow, D. E., & Turner, J. A. (2011). Hybrid and Parallel Domain-Doecomposition Methods to Enable Monte Carlo Reactor Analyses. *Progress in Nuclear Science and Technology, 2* , 815-820.

[77] Wilson, P., & Feder, R. (2008). State-of-the-art 3-D radiation trasnport methods for fusion energy systems. *Fusion Engineering and Design , 83*, 824.

[78] Ibrahim, A. M., Mosher, S. W., Evans, T. M., Peplow, D. E., Sawan, M. E., Wilson, P. P., et al. (2011). ITER Neutronics Modeling Using Hybrid Monte Carlo/Deterministic and CAD-Based Monte Carlo Methods. *Nuclear Technology, 175* , 251-258.

[79] Tautges, T., & Wilson, P. (2009). Acceleration techniques for direct use of CAD-based geomtrics in Monte Carlo radiation transport. *Proceeding of International Conference on Advances in Mathematics, Computational Methods, and Reactor Physics.* Saratoga Springs, NY.

[80] Sawan, M., & Wilson, P. (2009). Application of CAD-neutronics coupling to geometrically complex fusion systems. *Proceeding of IEEE 23rd Symposim of Fusion Engineering (SOFE 23).* San Diego, CA.

[81] Fischer, U., & Iida, H. (2009). Use of CAD generated geometry data in Monte Carlo transport calculations for ITER. *Fusion Science and Technology , 56*, 702.

[82] Aldama, D., & Trkov, A. (2004). *FENDL 2.1, update of an evaluated nuclear data library for fusion applications.* Vienna, Austria: IAEA, INDC (NDS) 467.

[83] Herman, M., & Trkov, A. (2009). *ENDF-6 Formats Manual.* Brookhaven National Laboratory, BNL-90365-2009.

[84] Chadwick, M. B., Oblozinsky, P., Herman, M., Greene, N. M., McKnight, R. D., Smith, D. L., et al. (2006). ENDF/B-VII.0: Next Generation Evaluated Nuclear Data Library for Nuclear Science and Technology. *Nulcear Data Sheets* , 2931-3060.

[85] Knuth, D. E. (1973). *The Art of Computer Programming, 2nd edition.* Reading, MA: Addison-Wesley Pub. Co.

[86] Ibrahim, A., Peplow, D., Evans, E., Wagner, J., & Wilson, P. (2009). Improving the mesh generation capabilities in the SCALE hybrid shielding analysis sequence. *Transactions American Nuclear Society*, *100*, p. 302.

[87] Ibrahim, A., Peplow, D., Evans, T., Wilson, P., & Wagner, J. (2010). Imporving the SN adjoint source and geometry representaion capabilities in the SCALE hybrid shielding analysis sequence. *American Nuclear Society Radiation Protection and Shielding Division 2010 Topical Meeting.* Las Vegas, NV.

[88] *SCALE Newsletter.* (2011). Retrieved from Number 43: info.ornl.gov/sites/publications/Files/Pub30885.pdf

[89] Moule, D. (2011). *Sampling Material Composition of CAD Geometries (Master Thesis).* Madison, WI: University of Wisconsin-Madison.

[90] Baker, R. (2002). A block Adaptive Mesh Refinement Algorithm for the Neutral Particle Transport Equation. *Nuclear Science and Engineering , 141*, 1.

[91] Iida, H., Khripunov, V., Petrizzi, L., & Federici. (2004). *Nuclear Analysis Report version 3.* ITER IO, ITER IDM G 73 DDD 2 W 0.2.

[92] Loughlin, M., & Bastistoni, P. (2009). ITER nuclear analysis strategy and requirements. *Fusion Science and Technology* (56), 566.

[93] Iida, H. (2003). *Fast Neutron Flux and Nuclear Heat in the TF Coil Inboard Legs vs. Gap Width among Blanket.* ITER International Organization (NAG-236).

[94] Sato, S. (2006). Development of a CAD/MCNP interface program prototype for fusion reactor nuclear analysis. *Fusion engineering and design , 81*, 2767.